Title

Modeling the Compton Camera Response for Extended Voxel Sources

Authors

Gunther, Donald
Barnowski, Ross
Haefner, Andrew
et al.

Publication Date

2024-07-02

LBNL Report #2001559 2 July 2024

Modeling the Compton Camera Response for Extended Voxel Sources

by

Donald L. Gunter, Ross Barnowski, Andrew Haefner, Daniel Hellfeld, Kalie Knecht, Lucian Michailescu, Mark Bandstra, Victor Negut, Emily Frame, Ryan Pavlovski, Tenzing Joshi, Jayson Vavrek, Brian Quiter, Kai Vetter

The analysis and interpretation of coincidence events in a Compton camera requires the comparison of the expected rates of observed events from sources with various emission rates, energy spectra and spatial distributions. Radioactive source distributions are often represented by the activity distributed among numerous voxels; each voxel having uniform internal activity and spectra within a cube. In this paper a mathematical model is constructed that predicts the expected rate of coincident Compton events from the rate of emissions from a single voxel source. This detailed model incorporates (1) the finite voxel size, (2) the blurring of the "Compton cone" by the limitations of energy resolution in the detectors and (3) the uncertainty in the Compton cone-axis due to the limited spatial resolution and 'lever-arm' separation between the coincident interactions. The resultant rates can be used to generate the system response matrix for source reconstruction and, therefore, are directly applicable in list-mode MLEM source reconstruction algorithms.

Outline

I. Introduction

The primary result of this paper is a calculation of the expected rate of Compton camera events from the emission rate associated with a single voxel with specified location and size. This calculation is based on a large number of assumptions and an idealized mathematical model. These idealizations are justified by (1) the inclusion of many effects heretofore ignored, (2) the utility of the analytic tools for rapid calculations, (3) applicability of the results in list-mode MLEM reconstruction algorithms.

A Compton camera event consists of the coincident detection of two distinct interactions in the detector system. The interpretation of this event is that the first interaction is a Compton scattering and the second interaction is a photoelectric absorption.

There are many competitive interpretations possible: for example, the second interaction might be another Compton scattering with subsequent escape from the detector; or, the first interaction might actually be multiple interactions within a distance smaller than the spatial resolution of the detector. For the purposes of this analysis, these alternative interpretations will be ignored. A more serious problem is that the sequence of the interactions is unknown. If the two interactions are labeled 'A' and 'B', the sequence of interactions could be either 'AB' or 'BA' producing completely different event rates for each possible source. In this analysis the interaction sequence will be *assumed* known; that is interaction '1' will be assumed Compton scattering and interaction '2' will be assumed photo-absorption. The alternative interpretation can be evaluated and compared by reversing the order of the interactions.

The detailed analysis is presented in six sections (II-VI) and three appendices (A-C). In Section II, the experimental observations and input parameters of the mathematical and physical model are described and our notation is established. In Section III, a mathematical formalism is presented that describes the emission, propagation, scattering and absorption of radiation. In Section IV, the mathematical formalism of Section III is used for the prediction of a very general (and, in practice, a very complicated) formula for the rate of observed events from a single voxel source. The application of this general formula to realistic situations is presented in Section V. This analysis is repeated an compared for alternative sequencing of the interactions Section VI. The derivation of the rates in Section IV requires extensive mathematical calculations that are relegated to three appendices. Appendix A provides a mathematical description of the uncertainty in the direction of the scattered photon (i.e., the axis of the Compton cone) due to the separation and limited spatial resolution of the coincident interactions. Appendix B describes the blurring of the Compton cone due to the limited energy resolution of the detectors. Finally in Appendix C a very complicated four-dimensional integral is performed using a combination of projection and properties of the hypergeometric function. This result is then used in Sections V and VI for the calculation of the desired rates. In Section VII, the results are summarized and future applications discussed.

Four additional Appendices were added pertaining to alternative approaches to imaging with Compton cameras. Many problems are better analyzed in terms of incident fluxes of radiation rather than source voxels. Appendix D provides a natural conversion between the rates associated with a specific voxel (as calculated in this analysis) and the rates produced by an incident photon flux. The "analytic machinery" of this paper can be, thereby, converted directly to give the desired rates associated with incident fluxes. In Appendix E, a comparison is made between the results of our calculation and the published calculations of other researchers. In particular, the work of Xu and He is selected as one of the best published calculations and is compared with our results. In Appendix F, the application of our results is demonstrated in List-Mode MLEM algorithm.

Finally, Appendix G is a mathematical aside in which the approximation of n-dimensional "cubic" voxels by Gaussian functions is demonstrated and justified.

II. Description of the Experimental Measurement and the Voxel Source Model

The mathematical model proposed in this analysis consists of numerous approximations and model parameters. For convenience, one can divide the model into three mathematical components that describe: (1) the coincident detection process in the Compton camera, (2) the source emissions from a single voxel, and (3) the physical process of emission, propagation, and interaction of the radiation from source to detector. Each component of the model requires a collection of assumptions and approximations; and because the reliability of the analysis depends on these assumptions, this section will explicitly delineate the assumptions and model parameters associated with the detection process and voxel source model.

The Coincident Compton Camera Event

A Compton camera event consists of the coincident detection of two distinct interactions in the detector system. The interpretation of this event is that the first interaction (labeled '1') is a Compton scattering and the second interaction (labeled '2') is a photoelectric absorption. The method of sequencing the interactions will not be considered until Section VI; however, at this point the sequence is arbitrary. Each interaction in the Compton camera provides two basic parameters: (1) the 3D location of the interaction, and (2) the energy deposited in the detector. In addition, each parameter must also have an associated resolution. Thus, the input data associated with each event will describe the two interactions (i=1,2) and be denoted by

$$\{\vec{r}_i, \lambda_i\} = \text{ location and spatial resolution of interaction 'i' [m]}$$
$$\{E_i, \varepsilon_i\} = \text{ deposited energy and resolution of interaction 'i' [keV].} \qquad (1)$$

The energies, E_i, and their associated resolutions, ε_i, are simple scalars (with dimensions of keV for this analysis). The locations, $\vec{r}_i$, are 3-vectors (with dimensions of meters [m] in each coordinate). On the other hand, the spatial resolutions, λ_i, are assumed to be scalars (with dimensions [m]) that provide the isotropic resolution in all directions. Not only does the resolution of each parameter provide information about the accuracy of the measurement, but it also indicates the range of that parameter. *One cannot define the rate associated with an event at specific locations and energies, but one can define the rate of events within ranges of those parameters.* One, therefore, expects that the rate of observed events will be proportional to the resolutions in each of the 8 parameters (6 spatial coordinates and 2 energies), i.e.

$$Rate \;\propto\; \lambda_1^3 \;\lambda_2^3 \;\varepsilon_1\,\varepsilon_2\,. \qquad (2)$$

Ironically, an interaction with poorer resolution, i.e. larger λ_i or ε_i, will produce higher rates associated with the observed event because more interactions might potentially fall inside the assigned range. However, the blurring effects from loss of resolution will also distribute the increased rate over more source voxels; thereby, reducing the response attributed to any specific voxel. This dual role for the resolutions is crucial in the analysis;

an incorrect assignment of a resolution can significantly affect the rate calculation. For most of this paper, λ_i and ε_i are treated as experimental constants provided by prior measurements. Nonetheless, certain assumptions concerning the resolutions are implicit. Obviously, all the resolutions must be positive; more significantly, relation (2) implies that none of the resolutions, λ_i or ε_i , can vanish. Furthermore, the upper limits on the resolutions may appear implicitly [e.g. inequalities (15)] throughout the analysis. These upper limits reflect the practical fact that events with extremely poor resolution provide virtually no information and should generally be excluded from analysis.

The Source Voxel and Its Emissions

The source of emissions is described mathematically by a radioactive activity distribution, $A(\vec{x}, E)$, where

$$\vec{x} = \text{position of the emission},$$

$$E = \text{emission energy [keV]} \,, \tag{3}$$

and

$$A(\vec{x}, E) = \frac{[emissions]}{[sec][keV][m^3]} = \text{activity density at } \vec{x}.$$

[Although 'activity' generally refers to the *decay* rate of radioactive materials, in these notes the 'activity' will refer to the *emission* rate. The distinction is important for isotopes with multiple emissions/decay or alternative branching ratios. However, in maximum likelihood calculations (as summarized in Appendix F), the system matrix is most easily calculated as the ratio (rate of detections)/(rate of emissions). Consequently, these notes emphasize the number of emissions.] In general, the function, $A(\vec{x}, E)$, is a continuous function of $\vec{x}$ and E. However, in most imaging applications, the function, $A(\vec{x}, E)$), is decomposed into a large number of voxels – each voxel containing constant activity within a "small" cubic volume. In this representation, the activity distribution of a single voxel is given by

$$A_{voxel}(\vec{x}, E) = A(E)\Lambda\left(\vec{x} - \vec{C}, L\right) \tag{4}$$

where the vector $\vec{C}$ is the center of the voxel,

$$A(E) = \frac{[emissions]}{[sec][keV][m^3]} \text{ within the voxel, and}$$

$$\Lambda(\vec{x}, L) = \text{voxel spatial distribution [dimensionless]}. \tag{5}$$

A voxel is universally accepted as a cubic volume in 3D that has uniform properties; i.e., density, composition, etc. Each voxel is characterized by the location of its center point, $\vec{C}$, and length of its sides, L. Mathematically, a voxel is characterized by the function, Λ. The standard cubic voxel that is oriented along the x-, y-, and z-axes is described by the function:

$$\Lambda_{\text{cube}}(\vec{x}, L) = \begin{cases} 1 & \text{if } -\frac{L}{2} < x_i < \frac{L}{2} \\ 0 & \text{otherwise.} \end{cases} \tag{6}$$

Such a voxel is generally associated with a 3D lattice of voxels that provides both the regular spacing and the orientation of the voxel axes. For our modeling, the orientation of a voxel in space is not an important property; however, the spatial extent of the source is. Indeed, the orientation of the voxel axes requires an unnecessary complication in the calculations that provides little increase in accuracy. For this reason, the standard cubic voxel will be replaced by a rotationally invariant Gaussian source. The Gaussian voxel function is defined by

$$\Lambda(\vec{x}) = \left(\frac{6}{\pi}\right)^{3/2} \exp[-6\,|\vec{x}|^2 / L^2] \tag{7}$$

and is used throughout this analysis. This Gaussian voxel function is selected because it is rotationally symmetric, simplifies calculations, and, furthermore, produces the same integral moments (up to second order) as the cubic voxel in Equation (6); namely,

$$\iiint d^3\vec{x}\ \Lambda(\vec{x}) = L^3 \quad ; \quad \iiint d^3\vec{x}\ |\vec{x}|^2\, \Lambda(\vec{x}) = \frac{1}{4} L^5 \tag{8}$$

which is the reason for selecting the specific Gaussian parameters in Equation (7). (Details of this analysis are provided in Appendix G.) The primary limitation imposed by the spherical symmetry of a Gaussian voxel is that asymmetric voxels are excluded. If asymmetric voxels are required, one can approximate the desired distribution by the construction of the asymmetric geometry with numerous smaller spherical voxels. The "cost" of the multiple rate calculations is deemed smaller than the "cost" of orienting and calculating the rates for complicated voxel geometries.

Hybrid Parameters

The basic input parameters for each event are $\{\vec{r}_i, \lambda_i\}$ and $\{E_i, \varepsilon_i\}$ for i=1,2; whereas, the source voxel is described by the parameters $\vec{C}$, L, and the function A(E). The desired rates of interaction will be a function of these parameters. However, a number of hybrid combinations of these parameters arise naturally from the geometry and physics of the Compton interaction process and appear ubiquitously throughout the calculation. For convenience and future reference, these hybrid parameters are summarized here.

Within the detector, the two interactions are separated by the distance R_{12}, defined by

$$R_{12} \equiv |\,\vec{r}_2 - \vec{r}_1\,|\,, \tag{9a}$$

and the unit vector pointing from the first to the second interaction (and, therefore, approximating the direction of scattered photon) is denoted by

$$\vec{\alpha} \equiv (\,\vec{r}_2 - \vec{r}_1\,)/R_{12}\ . \tag{9b}$$

Combining Equations (9a) and (9b), one finds

$$(\vec{r}_2 - \vec{r}_1\,) = R_{12}\,\vec{\alpha}\,. \tag{9c}$$

The unit vector, $\vec{\alpha}$, is often referred to as the 'scattering-axis' of the Compton cone, because the Compton kinematics dictates that the source should lay near a cone determined by this axis with its vertex at $\vec{r}_1$.

The geometric relation between the source voxel and the detector is characterized by the vector $\left(\vec{r}_1 - \vec{C}\right)$ that connects the center of the voxel to the location of the first interaction. The distance between the source and detector is defined as R_s, where

$$R_s \equiv \left| \vec{r}_1 - \vec{C} \right| \tag{10a}$$

and the unit vector $\vec{\beta}$ denoting the direction from the source to the detector is

$$\vec{\beta} \equiv \left(\vec{r}_1 - \vec{C}\right)/R_s \tag{10b}$$

which indicates the approximate direction of an incident photon. One can, therefore, write that

$$\left(\vec{r}_1 - \vec{C}\right) = R_s\vec{\beta}\ . \tag{10c}$$

The scattering angle of the Compton interaction as measured by the source location and interaction locations is defined by

$$\vec{\alpha} \cdot \vec{\beta} \equiv \nu \equiv cos\ \theta_{geo} \tag{11}$$

Compton kinematics requires that the scattering angle is related to the energies deposited at each interaction site The function $\mu(E_1, E_2))$ gives the predicted cosine of the scattering angle for deposited energies E_1 and E_2:

$$\mu \equiv \mu(E_1, E_2) = cos\ \theta_{kin} = 1 - \frac{mE_1}{(E_1+E_2)E_2} \tag{12}$$

where m=electron mass [511 keV]. (N.B. Throughout this analysis the standard notation c=1 is assumed; so that, both energy and momentum are given keV.) . The imaging properties of a Compton camera arise from a comparison of the geometric scattering angle of Equation (11) with the kinematic scattering angle. The reality of the angle, θ_{kin}, requires that

$$\begin{aligned} -1 \le \mu \le 1 \quad &\Rightarrow \quad 2E_2^2 + 2E_1E_2 - mE_1 \ge 0 \\ &\Rightarrow \quad E_2 \ge \tfrac{1}{2}\left[\sqrt{E_1^2 + 2mE_1} - E_1\right] \ , \end{aligned} \tag{13}$$

a condition that excludes some interaction sequences. As Inequality (13) indicates, the value of μ, as defined in Equation (12), may be smaller than -1 and, therefore, unphysical. This condition is often referred to as the "backscatter limit" because the limiting equality holds for $\mu = -1$ (i.e. backscattered radiation). One might assume that an event violating the backscatter limit was improperly sequenced. However, due to the errors (ε_i) associated with the observed energies, this limit is somewhat blurred and an event that violates the backscatter limit by small energies ($<\varepsilon_i$) may actually be backscattered radiation with erroneous energies rather that unphysical sequencing. Consequently, values of $\mu(E_1, E_2) < -1$ is not *a priori* prohibited. Instead, the suppression of such events might be expected arise naturally from the interplay of the energy resolution and the Compton kinematics. [For details, see Appendix B.]

The effect of the voxel size on the imaging process arises from the dispersion of directions of radiation reaching detector. The crucial parameter describing this dispersion is the ratio of the distance between the source distance, R_s, and the "voxel" size L. In particular, the ratio

$$\Sigma_1 \equiv \frac{L}{\sqrt{12}R_s} \tag{14}$$

recurs throughout the calculation.

Finally, the scale of the various length parameters can be ordered hierarchically by either the detector design or physical constraints:

$$\lambda_i < R_{12} < L < R_s \tag{15a}$$

so that, one expects $\Sigma_1<0.28$. Similarly, the one expects the energy resolution to be significantly smaller than the measured values; that is,

$$5\varepsilon_i < E_i\ . \tag{15b}$$

The factor of 5 in Inequality (15b) is consistent with 20% error in the energy measurement (i.e., poorer energy resolution than any Compton camera currently used). Furthermore, in Appendix B where the blurring effects of energy resolution are calculated, the limits on the Σ_3 parameter are comparable to those on the Σ_1 parameter from Inequality (15a). The Inequalities (15a) and (15b) will frequently be invoked to simplify calculations.

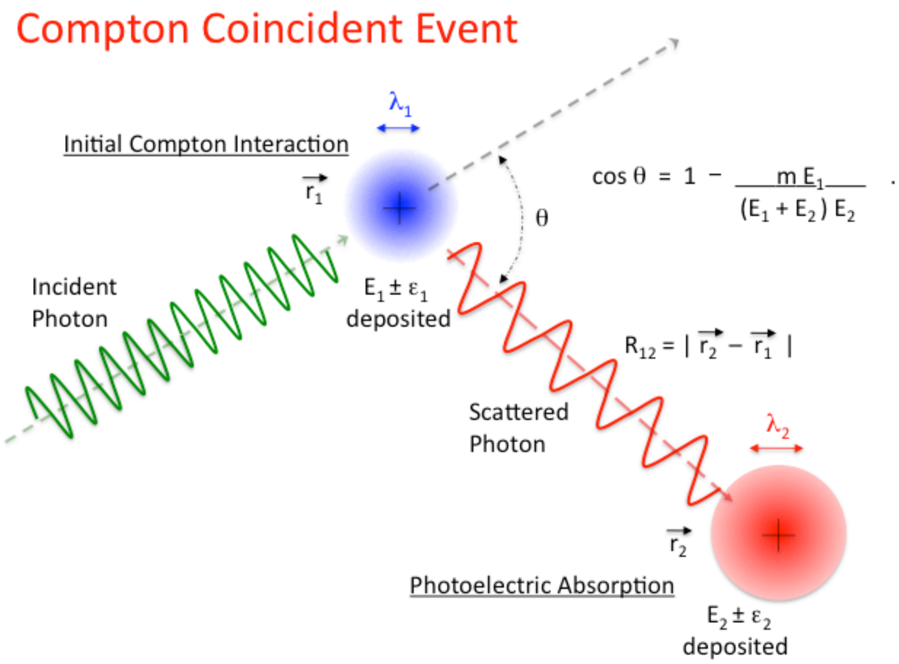

Figure 1. The Basic Geometry is depicted for a coincident Compton event within the detector. The data for a coincident Compton event includes not only the measured location and energy deposition at two interaction sites, but also the uncertainties in those measurements. These uncertainties critically affect the rate because larger volumes imply larger rates.

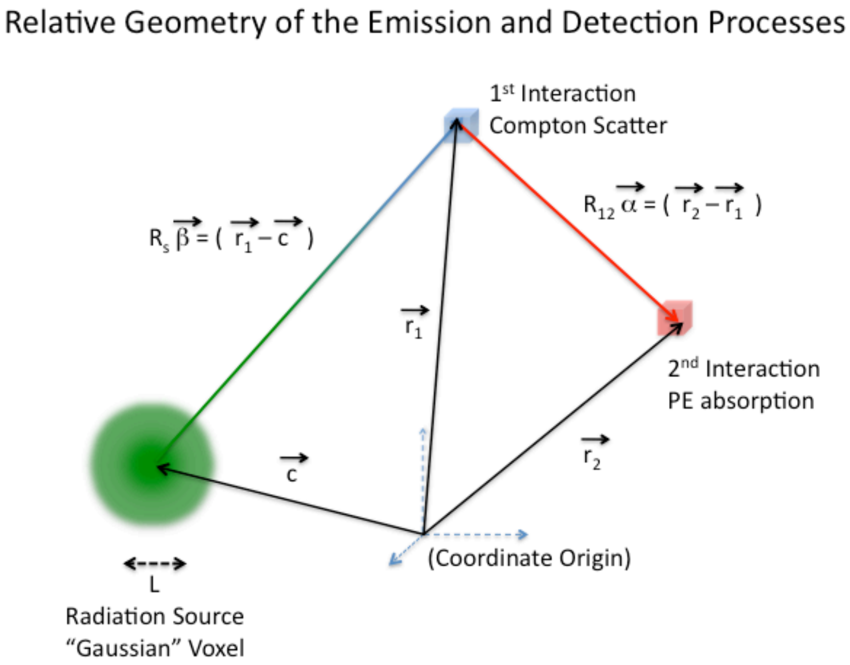

Figure 2. The Relative Geometry is shown between the source voxel and the interactions of the coincident Compton event. The direction $\vec{\beta}$ (shown in green) is approximately the direction of the incident photon; whereas, the direction $\vec{\alpha}$ (shown in red) is approximately the direction of the scattered photon.

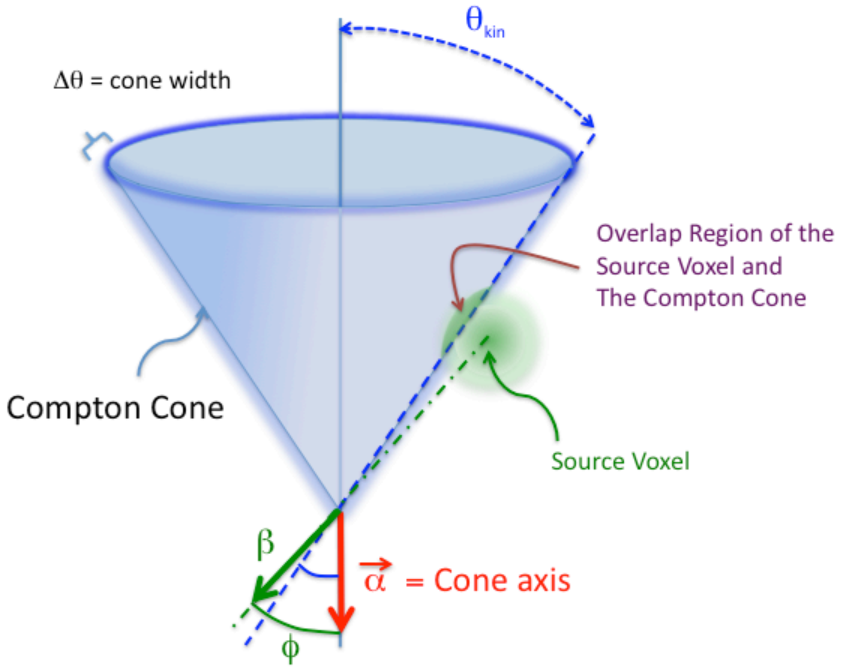

Figure 3. The imaging properties of a Compton camera are based on the back-projection of an event onto a Compton cone. This diagram demonstrates the relationship between the $\vec{\alpha}$ and $\vec{\beta}$ vectors and the back-projected Compton cone with opening angle θ_{kin} determined by the deposition energies. The rate of events is proportional to the overlap of the source voxel with the cone. Although the deposition energies determine a unique cone, the uncertainties in those energies blur that cone giving it an angular width $\Delta\theta$. Three sources of blurring are analyzed in this paper and each source has an associated parameter. The finite voxel size of the source blurs the direction of the incident radiation, $\vec{\beta}$, and is associated with the parameter Σ_1. Uncertainties in the interaction positions blur the direction of $\vec{\alpha}$ and are associated the parameter Σ_2. Uncertainties in the deposited energies cause blurring of the angle θ_{kin} and are associated with the parameter Σ_3.

III. Photon Emission, Propagation, and Interactions

The primary mathematical tool used in this analysis is the photon phase-space density, Φ, defined by

$$\Phi(\vec{x},\vec{p}) \equiv \frac{[\,\#photons\,]}{[m^3][keV^3]} = \text{photon phase} - \text{space density} \quad . \tag{16}$$

In general, one expects that Φ will be a function of time and will satisfy the Louiville equation with the appropriate scattering terms. For this analysis, however, we assume that the sources and geometry are constant during the period of the observation. Consequently, the photon phase-space density is stationary. Because the scattering of the radiation is crucial in the analysis, one decomposes the photon phase-space density based upon the number of scattering interactions. One, therefore, defines

$$\begin{gathered} \Phi^{(n)}(\vec{x},\vec{p}) = \text{photon phase} - \text{space density following (n)scatters} \\ \Phi(\vec{x},\vec{p}) = \sum_{n=0}^{\infty} \Phi^{(n)}(\vec{x},\vec{p}) \end{gathered} \tag{17}$$

where $\Phi^{(0)}$ corresponds to the photon density *entering the detector* and $\Phi^{(n)}$ corresponds to the photon density following the nth scatter *within* the detector. Thus, radiation that scatters *before entering the detector* is deemed part of the $\Phi^{(0)}$ component. The utility of this $\Phi^{(n)}$ decomposition is threefold: (1) for a Gaussian voxel source $\Phi^{(0)}$ is easily computed, (2) $\Phi^{(n+1)}$ is easily computed from $\Phi^{(n)}$ in terms of known differential cross-sections, and (3) the rate of interactions in a region is easily computed in terms of Φ and the attenuation coefficient within that region.

Emissions from a Voxel

The radiation incident on the detector is described by $\Phi^{(0)}$. In general, $\Phi^{(0)}$ can originate from either local or far-field sources. Far-field sources are essentially independent of the detector position (i.e., there are no parallax effects when the detector moves); astronomical sources typically fall into this category. These far-field sources are not of concern in this analysis. Local sources generally arise from the isotropic emissions of a radioactive source density $A(\vec{x},E)$ as described in Equations (3) and (4). The resulting radiation is given by

$$\Phi^{(0)}(\vec{x},\vec{p}) = \iiint d^3\vec{z} \int dE \;\; A(\vec{z},E) \;\; \frac{\text{Att}(\vec{x},\vec{z},E)}{4\pi c\, |\vec{x}-\vec{z}|^2} \;\; \delta^3\left(\vec{p} - E\,\frac{(\vec{x}-\vec{z})}{|\vec{x}-\vec{z}|}\right) \tag{18}$$

where the (dimensionless) attenuation function, Att, gives the fraction of radiation that propagates from $\vec{z}$ to $\vec{x}$ without absorption or scattering and is defined mathematically in terms of a line integral of the attenuation coefficient $\underline{\mu}(\vec{x},E)$,

$$\text{Att}(\vec{x},\vec{z},E) \equiv exp\left[\, -|\vec{x}-\vec{z}| \int_0^1 d\xi \;\; \underline{\mu}(\xi\vec{x} + (1-\xi)\vec{z}\,, E\,) \,\right] . \tag{19}$$

[Note: For this paper, the traditional symbol 'μ' for the attenuation coefficient is underlined '$\underline{\mu}$' to distinguish it from the cosine defined in Equation (12).] From the standard definitions, one recalls that

$$\underline{\mu}(\vec{x}, E) \equiv n(\vec{x})\, \sigma_{Total}(E) = attenuation\ coefficent\ [m^{-1}] \tag{20}$$

where

$$n(\vec{x}) = \frac{[\#scattering\ centers\ (atoms)]}{[m^3]} = number\ density\ of\ scatter\ centers \tag{21}$$

and

$$\sigma_{Total}(E) \equiv total\ scattering\ cross - section\ [m^2]\ \ . \tag{22}$$

A straightforward integration over the 3D delta function in Equation (18) yields that

$$\Phi^{(0)}(\vec{x}, \vec{p}) = \frac{1}{4\pi c\, |\vec{p}|^2} \int_0^\infty dr\ \ \mathrm{A}\left(\vec{x} - r\frac{\vec{p}}{|\vec{p}|}, |\vec{p}|\right)\ \ \mathrm{Att}\left(\vec{x}, \vec{x} - r\frac{\vec{p}}{|\vec{p}|}, |\vec{p}|\right) \tag{23}$$

for *any* activity distribution $\mathrm{A}(\vec{x}, E)$. If one uses the activity distribution for a single voxel as described in Equations (4) and (7) with center at $\vec{C}$, voxel size L, and assumes negligible attenuation within the source voxel, the integral in Equation (23) can be evaluated analytically and gives

$$\begin{aligned}\Phi^{(0)}\left(\vec{C} + R\vec{\Omega}, E\vec{\omega}\right) = \frac{6\ \mathrm{A}(E) L\ \mathrm{Att}\left(\vec{C}, \vec{C} + R\vec{\Omega}, E\right)}{4\pi^2 c\ E^2} \exp\left\{ -\frac{6R^2}{L^2}\left[\ 1 - \left(\vec{\Omega}\cdot\vec{\omega}\right)^2\ \right]\right\} \\ \frac{1}{2}\left\{\ 1\ +\ \mathrm{erf}\ \left[\frac{\sqrt{6}R}{L}\ \left(\vec{\Omega}\cdot\vec{\omega}\right)\right]\right\}\end{aligned} \tag{24}$$

for *any* location ($\vec{C}$+R$\vec{\Omega}$) and momentum (E$\vec{\omega}$). The (1+erf) term in the second line of Equation (24) can be bothersome in calculations. However, for L<R [as one expects from Inequalities (15a)], one can approximate the second line by a Heaviside function, so that

$$\Phi^{(0)}\left(\vec{C} + R\vec{\Omega}, E\vec{\omega}\right) = \frac{6\ A(E) L\ \mathrm{Att}\left(\vec{C}, \vec{C} + R\vec{\Omega}, E\right)}{4\pi^2 c\ E^2} \exp\left\{ -\frac{\left[\ 1 - \left(\vec{\Omega}\cdot\vec{\omega}\right)^2\ \right]}{2\ \Sigma_1^2}\right\}\ \Theta\left(\vec{\Omega}\cdot\vec{\omega}\right) \tag{25}$$

which is the form used henceforth in this analysis. N.B.: There is no explicit R^{-2} term in this expression. The effect of source distance does not appear explicitly in $\Phi^{(0)}$. Instead, the effect of moving further from the source is a narrowing of the momentum distribution [as characterized by the $\left(\vec{\Omega}\cdot\vec{\omega}\right)$ dependence]. So that the flux, integrated over all photon directions, is proportional to Σ_1^2 and, therefore, decreases with distance as R^{-2}. The ubiquitous Σ_1 term that was defined in Equation (14) originates in Equation (25).

Scattering of Radiation Within the Detector

The photon phase-space density $\Phi^{(n+1)}$ arises from the scattering of photons in the $\Phi^{(n)}$ photon density. The explicit relation is given by the integral equation

$$\Phi^{(n+1)}(\vec{x}, \vec{p}) = \iiint d^3\vec{z} \iiint d^3\vec{k}\ \ \Phi^{(n)}\left(\vec{z}, \vec{k}\right)\ \frac{\mathrm{Att}(\vec{x}, \vec{z}, |\vec{p}|)\ n(\vec{z})}{|\vec{x} - \vec{z}|^2}\ \frac{d^3\sigma}{d^3\vec{p}}\left(\vec{k} \longrightarrow \vec{p}\right)\ \delta^2\left(\frac{\vec{p}}{|\vec{p}|}, \frac{\vec{x} - \vec{z}}{|\vec{x} - \vec{z}|}\right) \tag{26}$$

where the δ^2 function on the 2-sphere is defined by the relation

$$F(\vec{\omega}) \equiv \iint_{S^2} d^2\vec{\Omega}\ \delta^2(\vec{\omega}, \vec{\Omega})\, F(\vec{\Omega}) \tag{27}$$

for any function F on the sphere. One can verify Equation (26) by considering the standard laboratory scattering experiment with a mono-energetic incident beam impinging on a small target and finding the predicted flux of scattered particles in the far-field. For our analysis, further notation concerning the differential cross-section is required. In Equation (26) the differential cross-section includes all forms of scattering. While many types of interaction are possible, only two are relevant for this analysis: Compton scattering and photoelectric absorption. Because other forms of interaction are possible [and appear in the total cross-section of Equation (22)], care is needed in the notation. We recall some standard definitions and explain our non-standard notations. For photoelectric absorption, the total cross-section is defined as

$$\sigma_{PE}(E) \equiv\ Photoelectric\ absorption\ cross - section\ [m^2]\ . \tag{28}$$

For Compton scattering, our notation is

$$\frac{d^3\sigma_{Compton}}{d^3\vec{p}}\left(\vec{k} \longrightarrow \vec{p}\right) \equiv differential\ Compton\ cross - section\ \left[\frac{m^2}{keV^3}\right] \tag{29a}$$

and

$$\sigma_{Compton}(E) \equiv Total\ Compton\ cross - section\ \ [m^2] \tag{29b}$$

where

$$\sigma_{Compton}(E) = \iiint d^3\vec{p}\ \ \frac{d^3\sigma_{Compton}}{d^3\vec{p}}(E\vec{e}_3 \rightarrow \vec{p})\ . \tag{29c}$$

[N.B. the arbitrary direction of the incident radiation ($\vec{e}_3$) in Equation (29c) does not affect the calculation because the integral covers all directions relative to that direction.] The total cross-section, σ_{Total}, includes other types of interaction; so that, the total cross-section may exceed the combined Compton and photoelectric cross-sections:

$$\sigma_{PE}(E) + \sigma_{Compton}(E) \le \sigma_{Total}(E)\ . \tag{30}$$

Next, the interaction fractions are defined by

$$f_{PE}(E) \equiv \frac{\sigma_{PE}(E)}{\sigma_{Total}(E)} \quad \text{and} \quad f_{CS}(E) \equiv \frac{\sigma_{Compton}(E)}{\sigma_{Total}(E)}\ . \tag{31}$$

Consequently, one can write

$$\frac{d^3\sigma_{Compton}}{d^3\vec{p}}\left(E\vec{\Omega} \longrightarrow \vec{p}\right) = \sigma_{Total}(E)\, f_{CS}(E)\left[\frac{1}{\sigma_{Compton}(E)}\frac{d^3\sigma_{Compton}}{d^3\vec{p}}\left(E\vec{\Omega} \longrightarrow \vec{p}\right)\right] \tag{32}$$

and, consequently, the terms appearing in Equation (26) can be written as,

$$n(\vec{x})\ \frac{d^3\sigma_{Compton}}{d^3\vec{p}}\left(E\vec{\Omega} \longrightarrow \vec{p}\right) = \underline{\mu}(\vec{x}, E)\, f_{CS}(E)\ \left[\frac{1}{\sigma_{Compton}(E)}\frac{d^3\sigma_{Compton}}{d^3\vec{p}}\left(E\vec{\Omega} \longrightarrow \vec{p}\right)\right]. \tag{33}$$

The differential cross section in Equation (29a) incorporates in a single expression both the Klein-Nishina differential cross-section and the kinematic relation between scatter angle and energy. One relates this (3D) differential Compton cross-section of Equation (29) to the standard Klein-Nishina form by observing that the (3D) cross-section must include three factors: (1) phase space weighting, (2) relativistic kinematics [i.e., energy and momentum conservation], and (3) the Klein-Nishina cross-section that describes physics of the scattering process. The resulting expression for free-electron scattering is given by

$$\frac{d^3\sigma_{Compton}}{d^3\vec{p}}\left(E\vec{\Omega}\longrightarrow p\vec{\omega}\right)=\frac{1}{p^2}\,\delta\left[p-\frac{mE}{m+E\left(1-\vec{\Omega}\cdot\vec{\omega}\right)}\right]\frac{d\sigma_{KN}}{d^2\Omega}(E,p) \tag{34}$$

[For Compton scattering from atomic electrons, one must also include the incoherent atomic scattering form-factor, but that term will be ignored in this treatment. The incoherent form-factor, which is approximately equal to the atomic number Z, can significantly suppress small-angle scattering, but such events are seldom significant in Compton cameras. Such small-angle events imply low momentum transfer, i.e., small E_1 values. The effects of the incoherent form factor generally arise for values of E_1 near or below the noise thresholds of the cameras, which is the justification for ignoring the effects in this analysis.] Next, we define the [dimensionless] Klein-Nishina weighting function by

$$X_{KN}(E,p)\equiv\frac{1}{\sigma_{Compton}(E)}\frac{d\sigma_{KN}}{d^2\Omega}(E,p) \tag{35}$$

so that

$$\frac{d^3\sigma_{Compton}}{d^3\vec{p}}\left(E\vec{\Omega}\longrightarrow p\vec{\omega}\right)=\frac{\sigma_{Compton}(E)}{p^2}\;\delta\left[p-\frac{mE}{m+E\left(1-\vec{\Omega}\cdot\vec{\omega}\right)}\right]\;X_{KN}(E,p)\;. \tag{36}$$

Applying Equations (33) and (36) in Equation (26), one finds the crucial relation

$$\Phi^{(n+1)}\left(\vec{x},p\vec{\Omega}\right)=\iiint d^3\vec{z}\int dk\,k^2\int_{S^2}d^2\vec{\omega}\;\;\Phi^{(n)}(\vec{z},k\vec{\omega})\;\;\delta^2\left(\vec{\Omega},\frac{\vec{x}-\vec{z}}{|\vec{x}-\vec{z}|}\right)\;\frac{\mathrm{Att}(\vec{x},\vec{z},p)\;\underline{\mu}(\vec{z},k)}{|\vec{x}-\vec{z}|^2}$$

$$\frac{f_{CS}(k)}{p^2}\;\delta\left[p-\frac{mk}{m+k\left(1-\vec{\Omega}\cdot\vec{\omega}\right)}\right]\;X_{KN}(k,p)\;. \tag{37}$$

Detection of Interactions Within the Detector

The calculation of interaction rates within the detector is comparatively simple. The rate of photoelectric absorptions in a region ΔR and within an energy interval ΔE is given by

$$Rate_{PE}(\Delta R,\Delta E)=\iiint_{\vec{x}\in\Delta R}d^3\vec{x}\iiint_{|\vec{k}|\in\Delta E}d^3\vec{k}\;\;\Phi\left(\vec{x},\vec{k}\right)\underline{\mu}\left(\vec{x},\left|\vec{k}\right|\right)f_{PE}\left(\left|\vec{k}\right|\right)c\quad, \tag{38}$$

where c is the speed of light. A generalization is required for the description of a detection system that reports the interaction position $(\vec{r}_i,\lambda_i)$ and deposition energy (E_i,ε_i). The spatial region associated with an interaction $(\vec{r}_i,\lambda_i)$ is described by a function D_x, and the energy interval associated with the observation (E_i,ε_i) is described by a function D_E. The function D_x specifies the volume included in the detection region and must satisfy the conditions

$$0 \leq D_x(\vec{x}|\vec{r},\lambda) \leq 1 \,,$$

$$\iiint d^3\vec{x} \;\; D_x(\vec{x}|\vec{r},\lambda) \;=\; (2\pi)^{3/2}\lambda^3 = volume\ of\ detection\ region \quad \text{, and} \tag{39a}$$

$$\iiint d^3\vec{x} \;\; \vec{x} \;\; D_x(\vec{x}|\vec{r},\lambda) = \; (2\pi)^{3/2}\lambda^3\,\vec{r} \quad .$$

Likewise, the function D_E describes the energy window and must satisfy the conditions

$$0 \leq D_E(k|E,\varepsilon) \leq 1 \,,$$

$$\int dk \;\; D_E(k|E,\varepsilon) \;=\; (2\pi)^{1/2}\varepsilon = width\ of\ the\ energy\ window \tag{39b}$$

$$\int dk \;\; k \;\; D_E(k|E,\varepsilon) \;=\; (2\pi)^{1/2}\varepsilon\, E \quad .$$

In Equations (39a&b), the "dummy" variables of integration, '$\vec{x}$' and 'k', represent the *actual* location of the interaction and energy deposited in the detector; whereas, '$\vec{r}$' and 'E' represent the *reported* location and energy deposition of the interaction. Furthermore, the detector may not report all interactions. This phenomenon can be accounted for by an efficiency function $\mathrm{Eff}(\vec{r},E)$, that satisfies $0 < \mathrm{Eff}(\vec{r},E) < 1$. [The 'Eff' function is essentially a "Finagle" factor that allows one to adjust the response in various detector locations based on prior measurements. For example, some solid-state detectors may have crystal defects that inhibit charge collection in specific pixels; or edge pixels may exhibit reduced collection efficiencies. Such phenomena are device specific and outside the current analysis.] The rate in Equation (38) is then generalized by

$$Rate_{PE}(D) = Eff(\vec{r},E) \iiint d^3\vec{x} \iiint d^3\vec{k} \;\; \Phi\left(\vec{x},\vec{k}\right) \; \underline{\mu}\left(\vec{x},\left|\vec{k}\right|\right) c\, f_{PE}\left(\left|\vec{k}\right|\right)$$

$$D_x(\vec{x}|\vec{r},\lambda) \;\; D_E\left(\left|\vec{k}\right|\middle| E,\varepsilon\right) \;. \tag{40}$$

Two sets of detector functions can be useful in this analysis. An "ideal" detector can be defined by

$$D_x^{ideal}(\vec{x}|\vec{r},\lambda) = (2\pi)^{3/2}\,\lambda^3 \;\; \delta^3(\vec{x}-\vec{r})$$

$$D_E^{ideal}(k|E,\varepsilon) = (2\pi)^{1/2}\;\varepsilon\;\;\delta(k-E) \;\; . \tag{41}$$

The ideal detector model provides the appropriate detector volume and energy window, but ignores the blurring effects caused by uncertainties in location and energy. A more "realistic" detector is defined by

$$D_x^{real}(\vec{x}|\vec{r},\lambda) = \exp\left(-\frac{|\vec{x}-\vec{r}|^2}{2\lambda^2}\right)$$

$$D_E^{real}(k|E,\varepsilon) = \exp\left(-\frac{(E-k)^2}{2\varepsilon^2}\right) \;. \tag{42}$$

These “realistic” detector functions give the appropriate detector volume and energy window and also provide the appropriate blurring effects associated with the uncertainties in location and energy.

The “ideal” detector is very useful because multiple integrals disappear trivially when acting on delta functions. For example, in Equation (40), the “ideal” detector yields

$$Rate_{PE}^{ideal} = (2\pi)^2\, \lambda^3\, \varepsilon\ \mathrm{Eff}(\vec{r},E)\ E^2 f_{PE}(E)\, \underline{\mu}(\vec{r},E)\, c \iint_{S^2} d^2\vec{\Omega}\ \Phi\left(\vec{r},E\vec{\Omega}\right)\ . \tag{43}$$

Unfortunately, the idealized detector model produces anomalous results if applied uncritically to the Compton camera analysis. In particular, the delta functions produce a “perfect” Compton cone. The rate calculation requires the evaluation of an overlap integral involving this Compton cone and the activity distribution of a voxel. If this overlap integral is evaluated with the idealized detector functions, the rate from a source in the far-field decays as R^{-1} rather than R^{-2}. This anomaly arises from multi-dimensional blurring. The Compton cone actually has finite angular width that changes the dimensionality of the cone integral from 2 to 3 dimensions – with significant consequences for distant sources. Earlier versions of this calculation started from the idealized detector model and then included *ad hoc* blurring to compensate for the anomaly; so that, one recovered the appropriate R^{-2} behavior. This *ad hoc* approach solved the immediate problem, but failed to convince the lead author that the blurring was properly treated. In the current treatment only the D^{real} functions are used.

With this notation, we have all the mathematical tools necessary for the evaluation of the rate of coincident Compton camera events.

IV. General Theory of Coincident Detection Rates for Two-Interaction Compton Camera Events

A two-interaction Compton camera event consists of the simultaneous detection of two interactions, D1 and D2. D1 is the initial Compton scattering interaction of an incident photon having momentum $\vec{k}_1$ at location $\vec{x}_1$ in the detector that is observed at location $\vec{r}_1(\pm\lambda_1)$ and deposits energy $E_1(\pm\varepsilon_1)$. The scattered photon then propagates with momentum $\vec{k}_2$ to location $\vec{x}_2$ where it undergoes photoelectric absorption and is reported as interaction D2 at location $\vec{r}_2(\pm\lambda_2)$ with energy $E_2(\pm\varepsilon_2)$ deposited.

Our analysis of this event begins with the final photoelectric absorption at D2. According to Equation (40), the rate of photoelectric absorptions from previously (single) scattered photons that are detected with the parameters $\{r_2\pm\lambda_2, E_2\pm\varepsilon_2\}$ of D2 is given by

$$Rate_{PE}(D2) = \mathrm{Eff}(\vec{r}_2,E_2)\ \iiint d^3\vec{x}_2 \iiint d^3\vec{k}_2\ \ \Phi^{(1)}\left(\vec{x}_2,\vec{k}_2\right)\ \underline{\mu}\left(\vec{x}_2,\left|\vec{k}_2\right|\right) c\ f_{PE}\left(\left|\vec{k}_2\right|\right)\ D_x(\vec{x}_2|\vec{r}_2,\lambda_2)\ D_E\left(\left|\vec{k}_2\right|\middle| E_2,\varepsilon_2\right)\ . \tag{44}$$

The single-scattered photon density, $\Phi^{(1)}$, arises from scattering of the incident radiation, $\Phi^{(0)}$. Based on Equation (37) one finds that

$$\begin{aligned}\Phi^{(1)}(\vec{x}_2,\vec{k}_2) = \iiint d^3\vec{x}_1 \iiint d^3\vec{k}_1\ \ \Phi^{(0)}(\vec{x}_1,\vec{k}_1)\ \frac{\mathrm{Att}(\vec{x}_1,\vec{x}_2,|\vec{k}_2|)\,\underline{\mu}(\vec{x}_1,|\vec{k}_1|)}{|\vec{x}_1-\vec{x}_2|^2}\\ \frac{f_{CS}(|\vec{k}_1|)\,X_{KN}(|\vec{k}_1|,|\vec{k}_2|)}{|\vec{k}_2|^2}\ \delta\left(|\vec{k}_2| - \frac{m|\vec{k}_1|}{m+|\vec{k}_1|-\frac{\vec{k}_1\cdot\vec{k}_2}{|\vec{k}_2|}}\right)\delta^2\left(\frac{\vec{k}_2}{|\vec{k}_2|},\frac{\vec{x}_2-\vec{x}_1}{|\vec{x}_1-\vec{x}_2|}\right).\end{aligned}\tag{45}$$

Combining Equations (44) and (45), one finds the rate of D2 interactions from an incident photon density, $\Phi^{(0)}$, to be

$$\begin{aligned}Rate_{PE}(D2) = \mathrm{Eff}(\vec{r}_2,E_2)\iiint d^3\vec{x}_2\iiint d^3\vec{k}_2\iiint d^3\vec{x}_1\iiint d^3\vec{k}_1\ \ \Phi^{(0)}(\vec{x}_1,\vec{k}_1)\ c\\ \underline{\mu}\left((\vec{x}_2,|\vec{k}_2|)\right)\ f_{PE}\left(|\vec{k}_2|\right)\frac{f_{CS}(|\vec{k}_1|)\,X_{KN}(|\vec{k}_1|,|\vec{k}_2|)}{|\vec{k}_2|^2}\ \frac{\mathrm{Att}(\vec{x}_1,\vec{x}_2,|\vec{k}_2|)\,\underline{\mu}(\vec{x}_1,|\vec{k}_1|)}{|\vec{x}_1-\vec{x}_2|^2}\\ \delta\left(|\vec{k}_2| - \frac{m|\vec{k}_1|}{m+|\vec{k}_1|-\frac{\vec{k}_1\cdot\vec{k}_2}{|\vec{k}_2|}}\right)\delta^2\left(\frac{\vec{k}_2}{|\vec{k}_2|},\frac{\vec{x}_2-\vec{x}_1}{|\vec{x}_1-\vec{x}_2|}\right)\\ D_x(\vec{x}_2|\vec{r}_2,\lambda_2)\ \ D_E\left(|\vec{k}_2|\,\middle|\,E_2,\varepsilon_2\right)\ .\end{aligned}\tag{46}$$

This rate includes scattered radiation from *all* regions of the detector. One, therefore, must restrict this rate to those initial interactions that are consistent with the detection of the first interaction D1. Such restrictions are accomplished very simply by inserting the appropriate detector functions Eff, D_x, and D_E for the D1 interaction; thereby, limiting the ranges of x_1 and k_1. Consequently, the rate for (D1,D2) coincident events is given by

$$\begin{aligned}Rate(D1,D2) = c\ \mathrm{Eff}(\vec{r}_1,E_1)\ \mathrm{Eff}(\vec{r}_2,E_2)\iiint d^3\vec{x}_1\iiint d^3\vec{k}_1\ \ \Phi^{(0)}(\vec{x}_1,\vec{k}_1)\\ \iiint d^3\vec{x}_2\iiint d^3\vec{k}_2\ \ \underline{\mu}\left((\vec{x}_2,|\vec{k}_2|)\right)\ f_{PE}\left(|\vec{k}_2|\right)\frac{f_{CS}(|\vec{k}_1|)\,X_{KN}(|\vec{k}_1|,|\vec{k}_2|)}{|\vec{k}_2|^2}\\ \frac{\mathrm{Att}(\vec{x}_1,\vec{x}_2,|\vec{k}_2|)\,\underline{\mu}(\vec{x}_1,|\vec{k}_1|)}{|\vec{x}_1-\vec{x}_2|^2}\ \delta\left(|\vec{k}_2| - \frac{m|\vec{k}_1|}{m+|\vec{k}_1|-\frac{\vec{k}_1\cdot\vec{k}_2}{|\vec{k}_2|}}\right)\delta^2\left(\frac{\vec{k}_2}{|\vec{k}_2|},\frac{\vec{x}_2-\vec{x}_1}{|\vec{x}_1-\vec{x}_2|}\right)\\ D_x(\vec{x}_2|\vec{r}_2,\lambda_2)\ \ D_E\left(|\vec{k}_2|\,\middle|\,E_2,\varepsilon_2\right)\ \ D_x(\vec{x}_1|\vec{r}_1,\lambda_1)\ \ D_E\left(|\vec{k}_1|-|\vec{k}_2|\,\middle|\,E_1,\varepsilon_1\right)\ .\end{aligned}\tag{47}$$

Despite its awkward appearance and the 12-dimensional integral, Equation (47) is actually the fundamental result of this paper – containing a minimum number of assumptions and not restricted to any specific source configuration. The delta functions remove 3 dimensions of the integration; but, the remaining 9 integrals are non-trivial. The convergence of the integrals is assured by the asymptotic behavior of the D^{real} functions. Furthermore, the positivity of the integrand assures that one can interchange the order of integration. Nonetheless, the rate calculation in Equation (47) is not immediately useful. The remainder of the paper consists of simplifications based on various assumptions that render the result applicable in realistic situations.

The first observation in our effort to simply Equation (47) is that many terms in the integrand are slowly varying functions that, on the small scale of the detector resolutions, are effectively constant; and, therefore, can be removed from the integrals. The following abbreviated notation will be adopted for these "constant" terms:

$$\begin{array}{ll} \underline{\mu}_1 \equiv \underline{\mu}(\vec{r}_1, E_1 + E_2) & Att_{ext} \equiv Att\big(\vec{C}, \vec{r}_1, E_1 + E_2\big) \\ \underline{\mu}_2 \equiv \underline{\mu}(\vec{r}_2, E_2) & Att_{int} \equiv Att(\vec{r}_1, \vec{r}_2, E_2) \\ f_{CS1} \equiv f_{CS}(E_1 + E_2) & Eff_1 \equiv Eff(\vec{r}_1, E_1) \\ f_{PE2} \equiv f_{PE}(E_2) & Eff_2 \equiv Eff(\vec{r}_2, E_2) \\ X_{KN}^{12} \equiv X_{KN}(E_1 + E_2, E_2^*)\ . & \end{array} \tag{48}$$

These functions are assumed constant over the effective domains of the D^{real} functions. Detectors are generally constructed with uniform materials, so that very little spatial variation in the attenuation coefficients $\underline{\mu}_i$ is expected. However, in asserting that the Att functions are effectively constant throughout the detection region, we are implicitly assuming that the variation in Att is small; a condition that is true if and only if, $\underline{\mu}_i \lambda_i \ll 1$. If this condition is not satisfied, the mean value of Att may give misleading results. Furthermore, the Att functions depend crucially on the path between x_1 and x_2, so that some sort of averaging may be necessary for different paths between the detection regions due to variations in the absorbing materials encountered. One can ameliorate both of these problems by subdividing the detector region. In the energy regime, the K-edge shell produces large discontinuities in the photoelectric cross-sections and can cause significant variations in the attenuation coefficients across small energy ranges. In particular, if the second interaction window ($E_2 \pm \varepsilon_2$) straddles such a discontinuity, the effect can be large. In such a case, one might consider splitting the analysis into two separate parts; using two narrow energy windows on either side of the K-edge, rather than a single energy window. Finally, the energies E_1 and E_2 may violate the backscatter limit [Inequality (13)]; so that, the Compton weighting X_{KN} is undefined. As discussed earlier, this situation generally arises from incorrect sequencing of the interactions. However, it can also arise from the imprecision in the energy measurements of an actual backscatter event. The expression for X_{KN} contains an E_2^* to indicate that, if the backscatter condition is violated, one should calculate X_{KN} as though the event were exactly backscattered [$\mu(E_1, E_2) = -1$]. The combination of relativistic kinematics and energy resolution should suppress the rate if the backscatter limit [Inequality (13)] is violated [see the analysis in Appendix B]. For the remainder of this analysis, the parameters listed in Equation (48) will be assumed constant and removed from the integrands; so that

$$\begin{aligned} Rate(D1,D2) = {} & c\ \mathrm{Eff}_1\ \mathrm{Eff}_2\ Att_{int}\ X_{KN}^{12}\ f_{CS1}\ f_{PE2}\ \underline{\mu}_1\ \underline{\mu}_2 \\ & \iiint d^3\vec{x}_1 \iiint d^3\vec{k}_1\ \ \Phi^{(0)}\left(\vec{x}_1,\vec{k}_1\right)\ \iiint d^3\vec{x}_2 \iiint d^3\vec{k}_2\ \ \frac{1}{\left|\vec{k}_2\right|^2}\ \frac{1}{\left|\vec{x}_1-\vec{x}_2\right|^2} \\ & \delta\left(\left|\vec{k}_2\right| - \frac{m\left|\vec{k}_1\right|}{m+\left|\vec{k}_1\right|-\frac{\vec{k}_1\cdot\vec{k}_2}{\left|\vec{k}_2\right|}}\right)\ \delta^2\left(\frac{\vec{k}_2}{\left|\vec{k}_2\right|},\frac{\vec{x}_2-\vec{x}_1}{\left|\vec{x}_1-\vec{x}_2\right|}\right) \\ & D_x(\vec{x}_2|\vec{r}_2,\lambda_2)\ D_E\left(\left|\vec{k}_2\right|\middle| E_2,\varepsilon_2\right)\ D_x(\vec{x}_1|\vec{r}_1,\lambda_1)\ D_E\left(\left|\vec{k}_1\right|-\left|\vec{k}_2\right|\middle| E_1,\varepsilon_1\right)\ . \end{aligned} \tag{49}$$

Next, one notes that the incident radiation, as represented by $\Phi^{(0)}$ in Equation (49), generally does not vary significantly as a function of $\vec{x}_1$ within the detection region D1 (although it will vary significantly as a function of $\vec{k}_1$). By definition, sources in the far field will not depend on x_1 at all. For voxel sources the incident radiation is described by $\Phi^{(0)}$ in Equation (25). This function *is* strongly dependent on $\vec{k}_1$; but, for $\lambda_1 << R_s$ as expressed in the Inequality (15a), the function $\Phi^{(0)}$ is unaffected by the location of $\vec{x}_1$ within region of detection $\vec{r}_1 \pm \lambda_1$. Consequently, Equation (49) can be reorganized into the form:

$$\begin{aligned} Rate(D1,D2) = {} & c\ \mathrm{Eff}_1\ \mathrm{Eff}_2\ Att_{int}\ X_{KN}^{12}\ f_{CS1}\ f_{PE2}\ \underline{\mu}_1\ \underline{\mu}_2 \\ & \int_0^\infty dk_1\, k_1^2 \iint_{S^2} d^2\vec{\Omega}_1\ \ \Phi^{(0)}\left(\vec{r}_1, k_1\vec{\Omega}_1\right) \\ & \int_0^\infty dk_2 \iint_{S^2} d^2\vec{\Omega}_2\ \ \delta\left(k_2 - \frac{m k_1}{m+k_1\left(1-\vec{\Omega}_1\cdot\vec{\Omega}_2\right)}\right)\ D_E(k_1-k_2|E_1,\varepsilon_1)\ D_E(k_2|E_2,\varepsilon_2) \\ & \iiint d^3\vec{x}_1\ \iiint d^3\vec{x}_2\ \ \frac{1}{\left|\vec{x}_1-\vec{x}_2\right|^2}\ \ \delta^2\left(\vec{\Omega}_2,\frac{\vec{x}_2-\vec{x}_1}{\left|\vec{x}_1-\vec{x}_2\right|}\right)\ D_x(\vec{x}_2|\vec{r}_2,\lambda_2)\ D_x(\vec{x}_1|\vec{r}_1,\lambda_1) \end{aligned} \tag{50}$$

where the unit vector $\vec{\Omega}_1$ denotes the direction of the incident radiation $\left[\vec{k}_1 \equiv k_1\vec{\Omega}_1\right]$ and $\vec{\Omega}_2$ denotes the direction of the scattered radiation $\left[\vec{k}_2 \equiv k_2\vec{\Omega}_2\right]$. [Note: the unit vectors Ω_1 and Ω_2 are strongly correlated with $\vec{\beta}$ and $\vec{\alpha}$, respectively, but are not equal! The unit vector $\vec{\beta}$ points from the center of the voxel to first interaction location and, therefore, should be approximately equal to $\vec{\Omega}_1$, the actual direction of the incident photon. Likewise, the unit vector $\vec{\alpha}$ points from the first interaction to the second and, therefore, should be approximately equal to $\vec{\Omega}_2$, the actual direction of the scattered photon.] For a Gaussian voxel, as defined in Equations (4) and (7) with center at $\vec{C}$ and size L, the incident radiation field, $\Phi^{(0)}$, is given by Equation (25) and yields a more explicit result:

$$
\begin{aligned}
Rate(D1,D2) = {} & \frac{6L}{4\pi^2}\ \mathrm{Eff}_1\ \mathrm{Eff}_2\ Att_{ext}\ Att_{int}\ X_{KN}^{12}\ f_{CS1}\ f_{PE2}\ \underline{\mu}_1\ \underline{\mu}_2 \\
& \iint_{S^2} d^2\vec{\Omega}_1 \iint_{S^2} d^2\vec{\Omega}_2\ \ \exp\left[-\tfrac{1}{2\Sigma_1^2}\left(1-\left(\vec{\Omega}_1\cdot\vec{\beta}\right)^2\right)\right]\ \Theta\left(\vec{\Omega}_1\cdot\vec{\beta}\right) \qquad (51) \\
& \int_0^\infty dk_1\ A(k_1)\ D_E\left(\tfrac{k_1^2(1-\vec{\Omega}_1\cdot\vec{\Omega}_2)}{m+k_1(1-\vec{\Omega}_1\cdot\vec{\Omega}_2)}\middle| E_1,\varepsilon_1\right)\ D_E\left(\tfrac{mk_1}{m+k_1(1-\vec{\Omega}_1\cdot\vec{\Omega}_2)}\middle| E_2,\varepsilon_2\right) \\
& \iiint d^3\vec{x}_1\ \iiint d^3\vec{x}_2\ \ \frac{1}{|\vec{x}_1-\vec{x}_2|^2}\ \ \delta^2\left(\vec{\Omega}_2,\tfrac{\vec{x}_2-\vec{x}_1}{|\vec{x}_1-\vec{x}_2|}\right)\ D_x(\vec{x}_2|\vec{r}_2,\lambda_2)\ D_x(\vec{x}_1|\vec{r}_1,\lambda_1)\ .
\end{aligned}
$$

Three terms in Equation (51) are "color coded" as representing the three blurring processes associated with Compton imaging. The integrals over $\vec{\Omega}_1$ and $\vec{\Omega}_2$ correspond to directions of the incident and scattered radiation, respectively. The "red" terms represent the dispersion in the direction of the incident radiation, $\vec{\Omega}_1$ due to the finite spatial size of the source voxel. The "purple" terms represent the blurring of the kinematic opening angle, $(\vec{\Omega}_1\cdot\vec{\Omega}_2)$, due to uncertainties in the observed energies, as represented by the D_E functions. The source activity, $A(k_1)$, appears among the "purple" terms because the emission spectrum must be convolved with the observed energy depositions. The "blue" terms represent the uncertainty in the direction of the scattered radiation, $\vec{\Omega}_2$, due to the limited spatial resolution of the detectors.

The evaluation of the integrals in Equation (51) begins with the formal definition of the components described in the last paragraph. The last component [the "blue" part of Equation (51)] represents the blurring of the scatter direction due to spatial resolution of the interactions. This component is denoted by the function $CA(\vec{\omega})$ (CA= "cone axis") that characterizes the distribution of the scatter direction and is defined by

$$CA(\vec{\omega}) \equiv \iiint d^3\vec{x}_1\ \iiint d^3\vec{x}_2\ \ \frac{1}{|\vec{x}_1-\vec{x}_2|^2}\ \ \delta^2\left(\vec{\omega},\tfrac{\vec{x}_2-\vec{x}_1}{|\vec{x}_1-\vec{x}_2|}\right)\ D_x(\vec{x}_2|\vec{r}_2,\lambda_2)\ D_x(\vec{x}_1|\vec{r}_1,\lambda_1)\ . \qquad (52)$$

The function CA gives the distribution of the cone-axis ($\vec{\omega}$) on the 2 sphere and is peaked [$CA(\vec{\omega})$ maximum] in the direction $\vec{\omega}=\vec{\alpha}$, that points from $\vec{r}_1$ toward $\vec{r}_2$. (N.B. Despite its role as the distribution of cone-axis directions, the function CA has dimensions $[\mathrm{m}]^4$.) An analytic approximation of CA is derived in Appendix A, where one finds that CA is given by

$$
\begin{aligned}
CA(\vec{\omega}) &= \frac{(2\pi)^2\lambda_1^3\lambda_2^3}{(\lambda_1^2+\lambda_2^2)}\ \Theta(\vec{\omega}\cdot\vec{\alpha})\ \exp\left\{-\frac{1}{2\Sigma_2^2}\left[\,1-(\vec{\omega}\cdot\vec{\alpha})^2\right]\right\} \qquad (53) \\
&= \frac{(2\pi)^2\lambda_1^3\lambda_2^3}{\Sigma_2^2 R_{12}^2}\ \Theta(\vec{\omega}\cdot\vec{\alpha})\ \exp\left\{-\frac{1}{2\Sigma_2^2}\left[\,1-(\vec{\omega}\cdot\vec{\alpha})^2\right]\right\}
\end{aligned}
$$

where $$\Sigma_2 \equiv \frac{\sqrt{\lambda_1^2+\lambda_2^2}}{R_{12}}\ . \qquad (54)$$

According to the Inequality (15a), one assumes $\lambda_i < R_{12}$ so that $\Sigma_2 < \sqrt{2}$. In practice, however, the only events with $5\lambda_i < R_{12}$ provide reasonable information. This restriction implies that $\Sigma_2 < 0.28$ which is comparable (not coincidentally) with the restriction associated with Σ_1 following Inequality (15a). As a result of these physical constraints on the imaging process, one concludes that $1/2\Sigma_1^2 > 6$ and $1/2\Sigma_2^2 > 6$.

The second component [the green part] of Equation (51) represents the blurring of the opening angle of the Compton cone associated with the energy measurements and resolution of the detectors. This component is denoted by the function OA(υ) (OA=”opening angle”) that characterizes the distribution of opening angles for the Compton cone and is defined by

$$OA(\upsilon) \equiv \int_0^\infty dk \;\; A(k) \;\; D_E\left(\frac{k^2(1-\upsilon)}{m+k(1-\upsilon)}\middle| E_1, \varepsilon_1\right) \; D_E\left(\frac{mk}{m+k(1-\upsilon)}\middle| E_2, \varepsilon_2\right) \; . \tag{55}$$

The function OA gives the distribution of cosine of the opening angle (υ) determined by the Compton kinematics, energy resolution and incident spectrum. (N.B. The function OA has dimensions [counts][m]$^{-3}$[sec]$^{-1}$.) The function OA is significantly more complicated than CA because it depends on the energy spectrum of the source. One expects the function OA to be peaked around $\upsilon = \mu(E_1, E_2)$, where the function μ is computed in Equation (12) for Compton scattering. Because OA depends on the (unknown) spectrum A(E), alternative functions are required depending on the assumed source spectrum. Basically, the function OA samples the source spectrum A(k) over a narrow energy band of width $\sqrt{\varepsilon_1^2 + \varepsilon_2^2}$ near k=(E$_1$+E$_2$). In Appendix B, we evaluate $OA(\upsilon)$ for a Gaussian source distribution of the form

$$A(k) = \frac{A^*}{\sqrt{2\pi}\Sigma_s} \; exp\left[-\frac{(k-E_s)^2}{2\Sigma_s^2}\right] \tag{B.2}$$

which can be adapted to represent either extremely narrow or broad emission spectra. N.B. The functions OA and A* have dimensions [counts][m]$^{-3}$[sec]$^{-1}$; whereas, E_s and Σ_s^2 have are energies (keV). For this analysis, we assume a narrow emission spectrum $(E_s \ll \varepsilon_1)$ and $(E_s \ll \varepsilon_2)$; so that Appendix B calculates

$$OA(\upsilon) = A^* exp\left[-\frac{(\upsilon-\mu)^2}{2\,\Sigma_3^2}\right] exp\left[-\frac{(E_s-E_1-E_2)^2}{2(\varepsilon_1^2+\varepsilon_2^2)}\right] \Theta\left(2 - \frac{m}{E_s}\frac{[\varepsilon_1^2 E_2+\varepsilon_2^2(E_s-E_1)]}{[\varepsilon_2^2 E_1+\varepsilon_1^2(E_s-E_2)]}\right) \tag{56a}$$

where

$$\mu = \mu\left(\frac{\varepsilon_2^2 E_1+\varepsilon_1^2(E_s-E_2)}{(\varepsilon_1^2+\varepsilon_2^2)}, \frac{\varepsilon_1^2 E_2+\varepsilon_2^2(E_s-E_1)}{(\varepsilon_1^2+\varepsilon_2^2)}\right) = 1 - \frac{m[\varepsilon_2^2 E_1+\varepsilon_1^2(E_s-E_2)]}{E_s[\varepsilon_1^2 E_2+\varepsilon_2^2(E_s-E_1)]} \cong \mu(E_1, E_2) \tag{56b}$$

and $$\Sigma_3 = \frac{m\varepsilon_1\varepsilon_2[\varepsilon_1^2+\varepsilon_2^2]^{3/2}}{[\varepsilon_1^2 E_2+\varepsilon_2^2(E_s-E_1)]^2} \cong \frac{\varepsilon_1\varepsilon_2}{\sqrt{\varepsilon_1^2+\varepsilon_2^2}}\frac{m}{E_2^2} \, . \tag{56c}$$

These results correspond to Equations (B.16) through (B.18) in Appendix B. The final Heaviside function in Equation (56a) arises from the backscatter cutoff introduced in Equation (B.31).

Using the functions CA and OA in Equation (51), one finds that the desired rate is given by

$$Rate(D1,D2) = \frac{6LA^{*}\,\lambda_1^3\lambda_2^3}{(\lambda_1^2+\lambda_2^2)}\ \mathrm{Eff}_1\ \mathrm{Eff}_2\ Att_{ext}\ Att_{int}\ X_{KN}^{12}\ f_{CS1}\ f_{PE2}\ \underline{\mu}_1\ \underline{\mu}_2$$

$$exp\left[-\frac{(E_S-E_1-E_2)^2}{2(\varepsilon_1^2+\varepsilon_2^2)}\right]\Theta\left(2-\frac{m}{E_S}\frac{[\varepsilon_1^2E_2+\varepsilon_2^2(E_S-E_1)]}{[\varepsilon_2^2E_1+\varepsilon_1^2(E_S-E_2)]}\right)$$

$$\iint_{S^2} d^2\vec{\Omega}_1 \iint_{S^2} d^2\vec{\Omega}_2\ \ \exp\left\{-\frac{1}{2\Sigma_1^2}\left[1-\left(\vec{\Omega}_1\cdot\vec{\beta}\right)^2\right]\right\}\Theta\left(\vec{\Omega}_1\cdot\vec{\beta}\right) \tag{57}$$

$$\exp\left\{-\frac{1}{2\Sigma_2^2}\left[1-\left(\vec{\Omega}_2\cdot\vec{\alpha}\right)^2\right]\right\}\Theta\left(\vec{\Omega}_2\cdot\vec{\alpha}\right)$$

$$\exp\left\{-\frac{1}{2\Sigma_3^2}\left[\vec{\Omega}_1\cdot\vec{\Omega}_2-\mu\right]^2\right\}.$$

The first line of Equation (57) is a product of numerous physical constants that describe the processes of the propagation, scattering, photo-absorption and detection of the radiation. When multiplied together, these constants have the desired physical dimensions [counts/sec]. The Gaussian and Heaviside functions in the second line assure that the source energy matches the detected energies and that the backscatter limit is observed. The integrals over all possible directions of the incident radiation $(\vec{\Omega}_1)$ and the scattered radiation $(\vec{\Omega}_2)$ are dimensionless but represent all the important imaging properties of a Compton detector. [N.B.: $\vec{\Omega}_1$and $\vec{\Omega}_2$ represent the *actual* directions of the incident photon and scattered photon, respectively; whereas $\vec{\alpha}$ and $\vec{\beta}$ represent the measured estimates for the direction of the scattered and incident radiation, respectively.] The pseudo-"Gaussian" exponential terms in lines 3 and 4 represent the distribution of the actual directions around their measured values. The width constants Σ_1 and Σ_2 indicate the uncertainty in those measured directions. Both the integrals over solid angles and the pseudo-"Gaussian" exponential terms are dimensionless weighting functions. The last line contains information about the Compton kinematics determined by the energy depositions. Figures 4 and 5 illustrate the pseudo-"Gaussian" distributions of $\vec{\Omega}_1$ and $\vec{\Omega}_2$ on the spheres and how their relative orientation is related to the opening angle θ_{kin} predicted by Compton kinematics $[\mu \approx \cos\theta_{kin}]$.

The ungainly integral term in Equation (57) can be compartmentalized by the introduction of a "Compton Cone" function, CC, defined by

$$CC\left(\vec{\alpha}\cdot\vec{\beta},\mu;\Sigma_i\right) \equiv \frac{1}{(2\pi\Sigma_1^2)(2\pi\Sigma_2^2)} \iint_{S^2} d^2\vec{\Omega}_1 \iint_{S^2} d^2\vec{\Omega}_2\ \Theta\left(\vec{\Omega}_1\cdot\vec{\beta}\right)\Theta\left(\vec{\Omega}_2\cdot\vec{\alpha}\right)$$
$$exp\left\{-\frac{1}{2\Sigma_1^2}\left[1-\left(\vec{\Omega}_1\cdot\vec{\beta}\right)^2\right]-\frac{1}{2\Sigma_2^2}\left[1-\left(\vec{\Omega}_2\cdot\vec{\alpha}\right)^2\right]\right\} \qquad (58)$$
$$exp\left\{-\frac{1}{2\Sigma_3^2}\left[\left(\vec{\Omega}_1\cdot\vec{\Omega}_2\right)-\mu\right]^2\right\}.$$

Recalling the definitions of Σ_1 [Equation (14)] and Σ_2 [Equation (54)] and using the definition of CC [Equation (58)], one can rewrite the rate [Equation (57)] as

$$Rate(D1,D2) = (L^3A^*)[\![Eff_1 Eff_2 Att_{int} Att_{ext}]\!]\left\{\frac{2\pi^2\lambda_1^2\lambda_2^2}{R_S^2R_{12}^2}\right\}\left[\underline{\mu}_1\lambda_1\underline{\mu}_2\lambda_2 f_{CS1}f_{PE2}X_{KN}^{12}\right]$$
$$exp\left[-\frac{(E_S-E_1-E_2)^2}{2\left(\varepsilon_1^2+\varepsilon_2^2\right)}\right]\Theta\left(2-\frac{m}{E_S}\frac{\left[\varepsilon_1^2E_2+\varepsilon_2^2(E_S-E_1)\right]}{\left[\varepsilon_2^2E_1+\varepsilon_1^2(E_S-E_2)\right]}\right)CC\left(\vec{\alpha}\cdot\vec{\beta},\mu;\Sigma_i\right) \qquad (59)$$

In Equation (59), the first term, (L^3A^*), equals the emissions per second from within the voxel. The [[hollow bracketed]] term consists of dimensionless coefficients that reduce the observed rate due to the detector efficiencies and attenuation between the emission and points of detection. The {curly bracketed} term is a dimensionless, geometric term depending only on distances R_s, R_{12}, and the spatial resolutions λ_i that characterizes the solid angles viewed by the associated detector volumes. The [square bracketed] term is a dimensionless interaction term that depends primarily on the energy depositions E_1 and E_2 and characterizes the probabilities of the Compton and photoelectric interactions. Thus, the overall dimensions of Rate(D1,D2) are given by the (L^3A^*) term; i.e. counts/sec. The crucial term for imaging appears in the CC function.

The Compton Cone function, CC, defined in Equation (58) suppresses rates for voxels located off the Compton cone and is, therefore, the most significant of this analysis. Unfortunately, the accurate evaluation of CC is difficult and requires complicated calculations. Nonetheless, one important property can be immediately deduced from the definition. Noting that

$$0 \le \exp\left[-\frac{1}{2\Sigma_3^2}\left[\left(\vec{\Omega}_1\cdot\vec{\Omega}_2\right)-\mu\right]^2\right] \le 1 \qquad (60)$$

one observes that

$$0 < CC\left(\vec{\alpha}\cdot\vec{\beta},\mu;\Sigma_i\right) \le \frac{1}{(2\pi\Sigma_1^2)(2\pi\Sigma_2^2)} \iint_{S^2} d^2\vec{\Omega}_1 \iint_{S^2} d^2\vec{\Omega}_2\ \Theta\left(\vec{\Omega}_1\cdot\vec{\beta}\right)\Theta\left(\vec{\Omega}_2\cdot\vec{\alpha}\right)$$
$$exp\left\{-\frac{1}{2\Sigma_1^2}\left[1-\left(\vec{\Omega}_1\cdot\vec{\beta}\right)^2\right]-\frac{1}{2\Sigma_2^2}\left[1-\left(\vec{\Omega}_2\cdot\vec{\alpha}\right)^2\right]\right\}. \qquad (61)$$

In the last term of the Inequalities (61) the integrals over $\vec{\Omega}_1$ and $\vec{\Omega}_2$ decouple and yield

$$0 < CC\left(\vec{\alpha}\cdot\vec{\beta},\mu;\Sigma_i\right) \le \frac{1}{\Sigma_1^2\Sigma_2^2}\,{}_1F_1\left(1,\frac{3}{2};-\frac{1}{2\Sigma_1^2}\right){}_1F_1\left(1,\frac{3}{2};-\frac{1}{2\Sigma_2^2}\right) \xrightarrow[\substack{\Sigma_1\ll 1\\ \Sigma_2\ll 1}]{} 1 \qquad (62)$$

where the ${}_1F_1$ functions in Equation (62) are the confluent hypergeometric functions. Thus, if the Inequalities (15) are satisfied, one finds 0<CC<1.

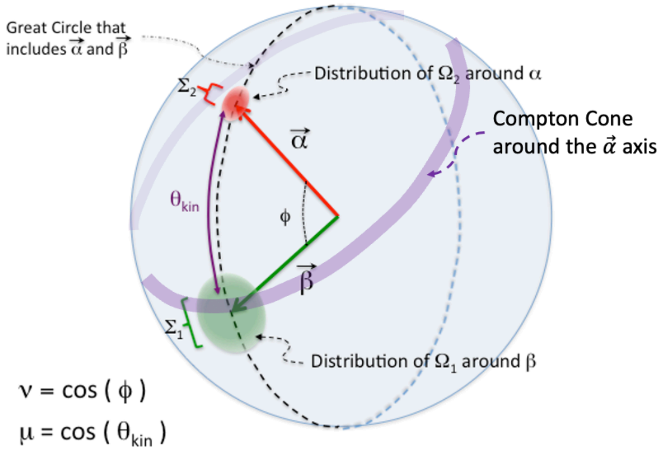

Figure 4. The distributions of $\vec{\Omega}_1$ and $\vec{\Omega}_2$ are shown on the sphere. The vector $\vec{\alpha}$ (often called the "axis of the Compton cone") is the direction of the scattered photon as determined by the locations of the two interactions. The actual direction of the scattered radiation $\vec{\Omega}_2$ is characterized by a distribution indicated by the red-shaded region having diameter parameterized by Σ_2. The vector $\vec{\beta}$ is the direction of the incident photon as determined by the locations of the voxel center and the first interaction. The actual direction of the incident radiation $\vec{\Omega}_1$ is characterized by a distribution indicated by the green-shaded region having diameter parameterized by Σ_1. The purple arc indicates the opening angle θ_{kin} predicted by Compton kinematics and the observed energy depositions. The purple "Compton Cone" intersects the celestial sphere with a finite width that is characterized by Σ_3. The CC function is determined by the overlap integral of the purple "Compton Cone" with the green "Source" direction. However, that simple overlap integral is complicated by the wobbling to the "Compton Cone" axis around the direction $\vec{\alpha}$.

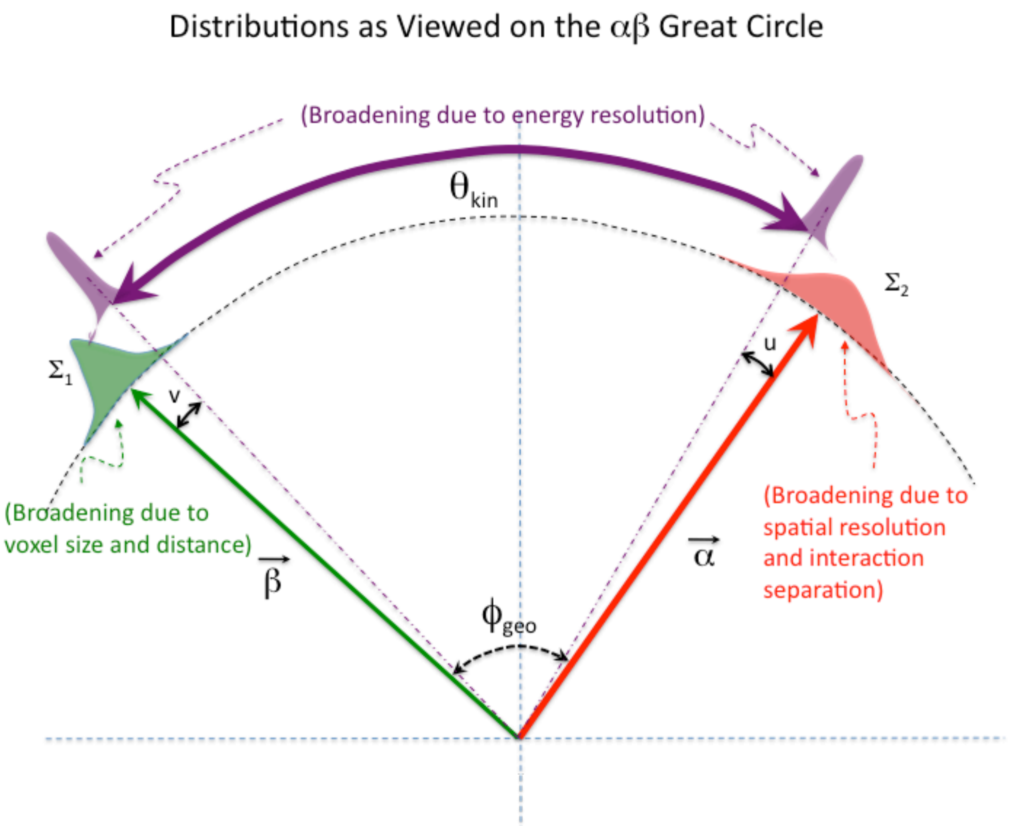

Distributions as Viewed on the αβ Great Circle

Figure 5. This diagram is a schematic slice through the sphere in Figure 4 on the great circle determined by vectors $\vec{\alpha}$ and $\vec{\beta}$. The integrals over $\vec{\Omega}_1$and $\vec{\Omega}_2$ involve the overlap of the distributions for $\vec{\Omega}_1$ (green), $\vec{\Omega}_2$ (red), and the angular separation of the characterized by $\vec{\Omega}_1 \cdot \vec{\Omega}_2 = cos(\theta_{kin})$ with a distribution OA (purple). In this figure the angle between $\vec{\alpha}$ and $\vec{\beta}$ (indicated as ϕ_{geo}) is slightly larger that the angle predicted by E_1, E_2, and the kinematics of Compton scattering, θ_{kin}.

The evaluation of the CC function is difficult. The details of the CC calculation are sufficiently complicated that the evaluation and resulting algorithm are relegated to Appendix C. In that appendix, a series of approximations are presented that culminate in Equations (C.51a-e). In summary, the best analytic approximation for CC currently available is given by

$$\nu \equiv \vec{\alpha} \cdot \vec{\beta} \tag{63a}$$

$$\mu \equiv max\left(-1\,,1-\frac{m\left[\varepsilon_2^2 E_1+\varepsilon_1^2(E_s-E_2)\right]}{E_s\left[\varepsilon_1^2 E_2+\varepsilon_2^2(E_s-E_1)\right]}\right) \tag{63b}$$

$$\sigma \equiv sign\left(\mu\sqrt{1-\nu^2}-\nu\sqrt{1-\mu^2}\right) \tag{63c}$$

$$\Upsilon \equiv max\left(\epsilon, \mu\nu+\sqrt{1-\mu^2}\sqrt{1-\nu^2}\right) \qquad [\epsilon \approx .001] \tag{63d}$$

$$\Delta \equiv \sigma\sqrt{1-\Upsilon^2} \tag{63e}$$

$$\chi \equiv \frac{\nu\Delta}{\Upsilon} \tag{63f}$$

and $$CC(\nu,\mu;\Sigma_i) = \frac{\Sigma_3}{\sqrt{\Sigma_3^2+(1-\nu^2)\Sigma_1^2+(1-\mu^2)\Sigma_2^2}}\, exp\left[-\frac{\left(\sqrt{1-\nu^2}-\chi\right)^2\Delta^2}{2\left[\Sigma_3^2+(1-\nu^2)\Sigma_1^2+(1-\mu^2)\Sigma_2^2\right]}\right]. \tag{63g}$$

[N.B. the Υ of Equation (63d) is effectively $cos\left(\theta_{kin}-\phi_{geo}\right)$ where $\mu = cos\theta_{kin}$ and $\nu = cos\phi_{geo}$ and the angular difference does not exceed $\pi/2$; so that, Equation (63e) implies $\Delta \cong \sin\left(\theta_{kin}-\phi_{geo}\right)$.] The combination of this approximate CC function [Equation(63g)] with Equation (59); namely,

$$Rate(D1,D2) = (L^3A^*)[\![Eff_1Eff_2Att_{int}Att_{ext}]\!]\left\{\frac{2\pi^2\lambda_1^2\lambda_2^2}{R_s^2R_{12}^2}\right\}\left[\underline{\mu}_1\lambda_1\underline{\mu}_2\lambda_2 f_{CS1}f_{PE2}X_{KN}^{12}\right]$$
$$exp\left[-\frac{(E_s-E_1-E_2)^2}{2\left(\varepsilon_1^2+\varepsilon_2^2\right)}\right]\,\Theta\left(2-\frac{m\left[\varepsilon_2^2E_1+\varepsilon_1^2(E_s-E_2)\right]}{E_s\left[\varepsilon_1^2E_2+\varepsilon_2^2(E_s-E_1)\right]}\right)\; CC(\nu,\mu;\Sigma_i), \tag{64}$$

produces a complete algorithm for the rate calculation. The value of μ calculated in Equation (63b) is always in the range [-1,1]; thereby, permitting one to compute the CC function for unphysical energy combinations. The Θ function that is added to the second line of Equation (64) eliminates kinematically prohibited combinations. Extreme caution must be exercised in using this result for events in the vicinity of $\mu = \pm 1$. As discussed in Appendices B and C, such events are of doubtful value in Compton cameras and should probably be excluded. Near $\mu = -1$ the angular resolution is poor and provides virtual no directional information. On the other hand, events in the vicinity of $\mu = 1$ have sufficient angular resolution, but are seldom observed due to small E_1 energy deposition. In either case the analytic approximations in Appendix C become problematic when the back-projection "cone" becomes a narrow pencil-beam.

Very early in the analysis [Equation (2)] we asserted that the observed rate should satisfy

$$Rate \;\propto\; \lambda_1^3\;\lambda_2^3\;\varepsilon_1\,\varepsilon_2. \tag{2}$$

If one examines Equation (64), the dependence on λ_1^3 and λ_2^3 appears exactly as expected. However, the dependence on ε_1 and ε_2 is problematic; nowhere in Equation (64) do the energy resolutions explicitly appear. Careful analysis reveals a hidden dependence arising from two terms: (1) the energy Gaussian and (2) the CC function. If one integrates the energy Gaussian over all the possible source energies (E_s), one gets a factor of $\sqrt{\varepsilon_1^2 + \varepsilon_2^2}$. If one evaluates the CC function for a voxel on the Compton cone ($\mu = \nu$), one finds

$$CC(\mu, \mu; \Sigma_i) = \frac{\Sigma_3}{\sqrt{\Sigma_3^2 + (1-\mu^2)(\Sigma_1^2 + \Sigma_2^2)}}, \tag{65}$$

so that

$$Rate \propto \frac{\varepsilon_1\, \varepsilon_2}{\sqrt{\Sigma_3^2 + (1-\mu^2)(\Sigma_1^2 + \Sigma_2^2)}}. \tag{66}$$

One can conclude that Equation (2) is satisfied provided that

$$\frac{\Sigma_3}{\sqrt{1-\mu^2}} < \sqrt{\Sigma_1^2 + \Sigma_2^2}. \tag{67}$$

Recalling Equation (B.21), one writes Inequality (67) as

$$\eta \frac{[m + E(1-\mu)]}{E\sqrt{1+\mu}} < \sqrt{\Sigma_1^2 + \Sigma_2^2} \tag{68}$$

which is generally satisfied except in the immediate vicinity of $\mu = -1$ where Appendix B has already revealed significant problems. Basically, the CC function has peak value $CC = 1$ in the vicinity of $\mu = \nu = -1$, due to the 'pencil beam' nature of the Compton cone. Elsewhere along the ($\mu = \nu$) line, the CC function gives rates proportional to $\varepsilon_1 \varepsilon_2$ because the Σ_3 contribution to the denominator of Equation (66) is smaller than the Σ_1 and Σ_2 contributions. However, in the vicinity of $\mu = \nu = -1$ the large values of Σ_3 dominate, so that one finds $Rate \propto \sqrt{\varepsilon_1^2 + \varepsilon_2^2}$, rather than $\varepsilon_1 \varepsilon_2$. This anomaly is directly attributable to the pathological broadening of the Compton cone in the backscatter limit.

V. Coincident Detection Rates for Voxel Sources with Narrow-Energy Spectra

This section displays and discusses the rate of (D1,D2) events as predicted by Equation (64). Of particular concern are the rate predictions for backscatter events ($\mu \approx -1$). In both Appendices B and C we observed that backscattered radiation produced large angular uncertainties that, subsequently, produced pathological broadening in the CC function. Indeed, Figures C.4 and C.5 seem to challenge the viability of Compton cameras because the CC function response for large-angle scattering was stronger than the response for small-angle scattering that provides better angular resolution. Fortunately, other terms in the Rate Equation (64) multiply the CC function and tend to suppress the backscatter response; thereby, ameliorating the problem. Recalling that backscatter events imply large energy transfers (E_1) at the first interaction, one expects smaller energy (E_2) for the scattered photons. These comparative energies affect three terms in Rate(D1,D2) equation that multiply the CC function; namely, Att_{int}, $\left(\underline{\mu}_2 f_{PE2}\right)$, and X_{KN}^{12}. [The combined term $\left(\underline{\mu}_2 f_{PE2}\right)$ is the portion of the attenuation coefficient arising from photoelectric absorption, and, consequently, is actually a single physical phenomenon]. Both Att_{int} and X_{KN}^{12} suppress the rate of backscattered radiation as compared to forward scattered radiation. On the other hand, the term $\left(\underline{\mu}_2 f_{PE2}\right)$ tends to increase at lower values of E_2 and, therefore, enhances the contribution from backscattered radiation. The competition between these effects determine the overall Rate(D1,D2). Aside from the energies E_1 and E_2, the other significant "event" parameter (i.e., unrelated to the source voxels) affecting the rate is R_{12}. The effects of the R_{12} term arise from (1) the obvious R_{12}^{-2} dependence and (2) the more subtle and significant effects on the Att_{int} term. The farther the scattered photon travels in the detector materials, the greater will be the attenuation, i.e. Att_{int} will be smaller. Because the attenuation term preferentially suppresses backscattered radiation, larger values of R_{12} will better suppress the backscatter response. The importance of these considerations will become obvious once the CC and Rate(D1,D2) functions are displayed.

The behavior of the CC and Rate(D1,D2) functions for individual events will be displayed by back-projection onto an array of source voxels. The source voxels will be of uniform size and located on the x-z plane. The voxel size is given by L=10cm; the 2D array of voxels runs from $(-900cm \leq x \leq 900cm)$ and $(-900cm \leq z \leq 900cm)$. The first D1 interaction is assumed to be detected at the origin $(x = y = z = 0)$; whereas, the second D2 interaction is detected at $(x = y = 0; z = -R_{12})$. Thus, the axis of the Compton cone $(\vec{\alpha})$ is always aligned along the negative z-axis; and the Compton cone intersects the 2D voxel array on a "V" shaped wedge with the vertex at the origin. Figure 6 shows a prototype diagram for the results that follow. For these displays, CZT was selected as the detector material and the spatial resolution of the interaction locations was set at 1mm. The cross-sections and attenuation coefficients were calculated based on interactions in CZT at the observed energies. Therefore, the basic parameters for the displays are:

$$\begin{aligned} &\lambda_1 = \lambda_2 = .1\ cm \\ &R_{12} = 1.5\ or\ 3.0\ cm \\ &L = 10\ cm \qquad (69) \\ &A^* L^3 = 1\ cnt/sec \\ &[\![Eff_1 Eff_2 Att_{ext}]\!] = 1 \end{aligned}$$

and

$$Att_{int} = exp\left[-0.9 R_{12} \underline{\mu}_2\right].$$

The calculation of Att_{int} is problematic because the distance that the scattered photon travels within the detector material before photo-absorption depends on the specific geometric design of the camera. Many cameras feature air gaps between detectors, so that only a fraction of the total separation (R_{12}) is actually inside the detector material. We selected $0.9R_{12}$ as a compromise attenuation length. The energy resolutions were calculated as described in Appendix B; namely,

$$\varepsilon(E) = \sqrt{\varepsilon_0^2 + \eta^2 m E} \qquad (B.19)$$

where we selected $\varepsilon_0 = 5\ keV$ and $\eta = 0.0331$ as typical values. The value $\eta = 0.0331$ corresponds to 3% energy resolution at E=662 keV; i.e., $E = 662 \pm 19.9\ keV$.

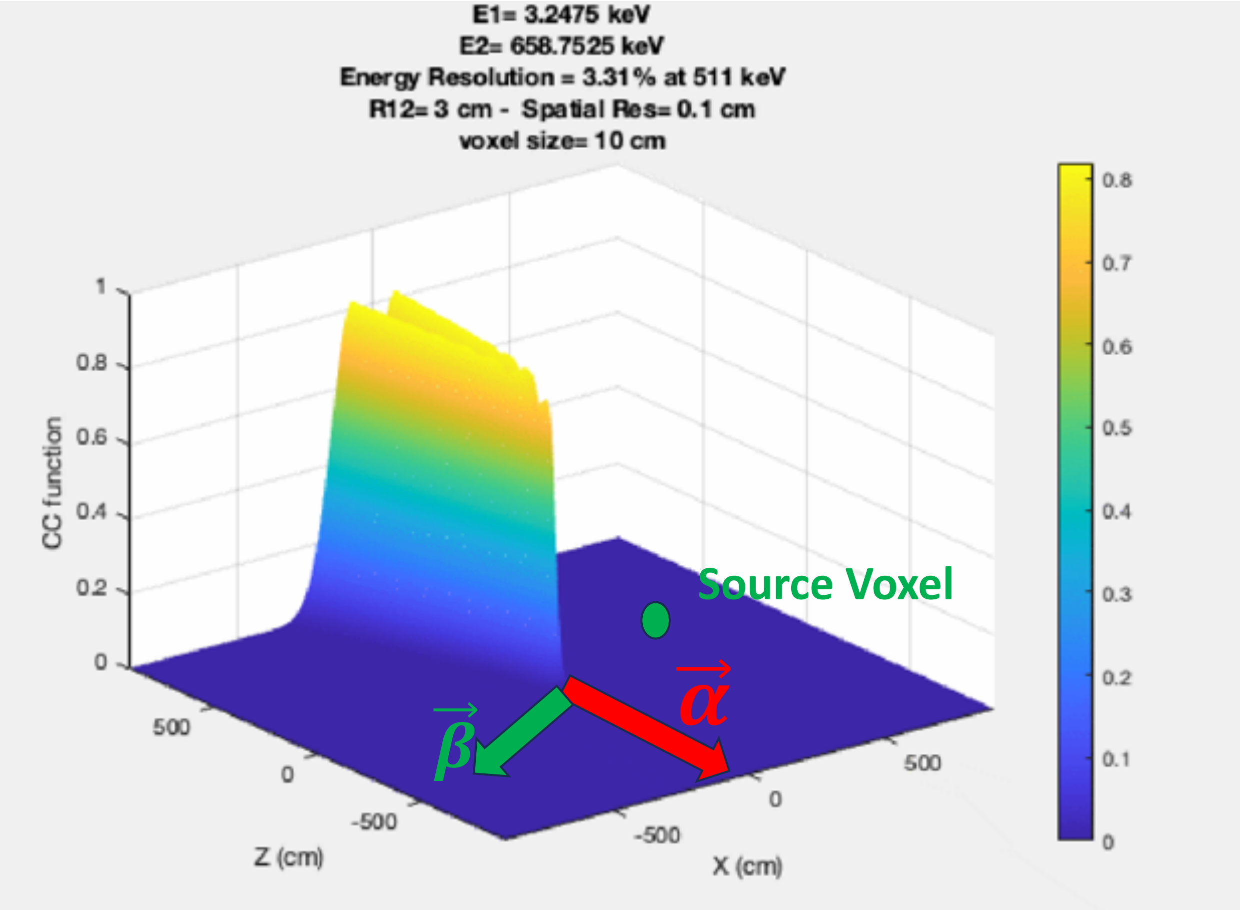

Figure 6. The standard display diagram for both the CC and Rate(D12,D2) functions is shown. The source voxels are distributed in the x-z plane. The vertical axis shows the back-projection of the function for a single event. The initial D1 interaction is assigned to the origin ($x = y = z = 0$). The second interaction is located at ($x = y = 0, z = -R_{12}$); so that, the cone axis is always along the negative z-axis; i.e., $\vec{\alpha} = -\vec{e}_z$. For a source voxel located at the green dot, the direction of the source radiation is denoted by the green vector, $\vec{\beta}$. The angle between $\vec{\alpha}$ and $\vec{\beta}$ is the geometric scattering angle; whereas, the predicted scattering angle is determined by the energies E_1 and E_2. If the two angles coincide, the CC function approaches 1; otherwise, the CC function is nearly zero. In this case, E1<<E2 which implies a small scattering angle. The resulting Compton cone is revealed as a very narrow 'V' along the positive z-axis with its vertex at the origin.

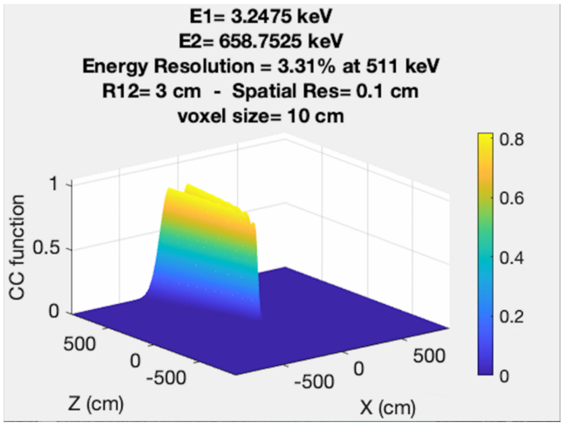
E1= 3.2475 keV
E2= 658.7525 keV
Energy Resolution = 3.31% at 511 keV
R12= 3 cm - Spatial Res= 0.1 cm
voxel size= 10 cm

Figure 7a

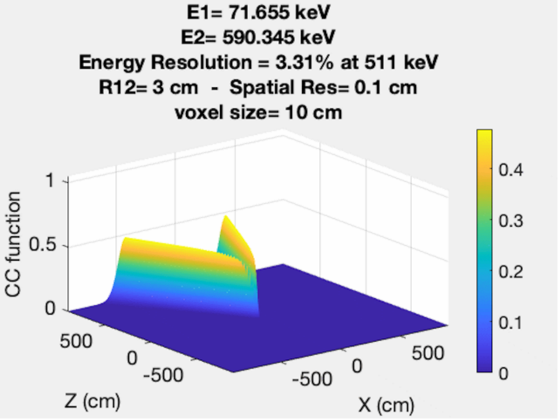
E1= 71.655 keV
E2= 590.345 keV
Energy Resolution = 3.31% at 511 keV
R12= 3 cm - Spatial Res= 0.1 cm
voxel size= 10 cm

Figure 7b

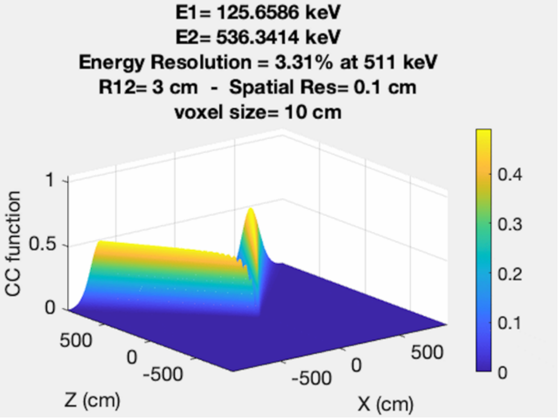
E1= 125.6586 keV
E2= 536.3414 keV
Energy Resolution = 3.31% at 511 keV
R12= 3 cm - Spatial Res= 0.1 cm
voxel size= 10 cm

Figure 7c

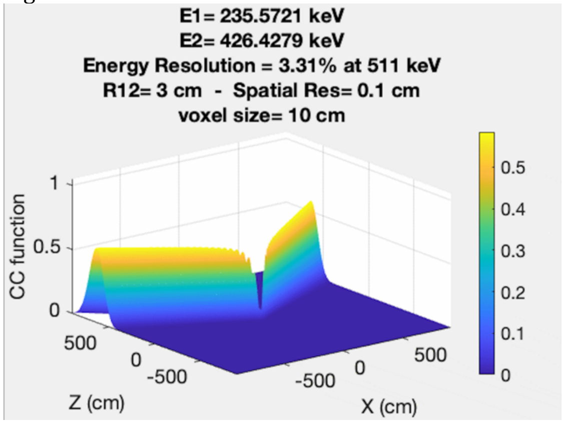
E1= 235.5721 keV
E2= 426.4279 keV
Energy Resolution = 3.31% at 511 keV
R12= 3 cm - Spatial Res= 0.1 cm
voxel size= 10 cm

Figure 7d

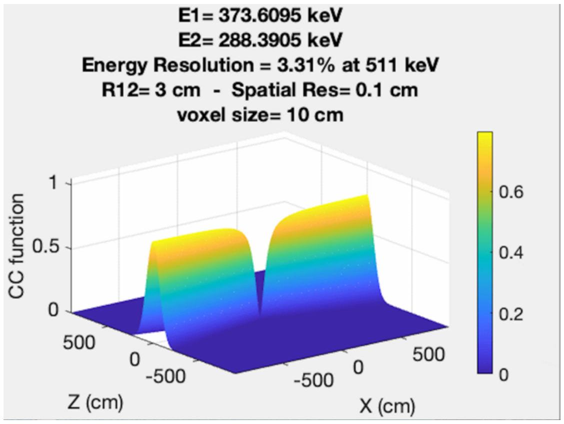
E1= 373.6095 keV
E2= 288.3905 keV
Energy Resolution = 3.31% at 511 keV
R12= 3 cm - Spatial Res= 0.1 cm
voxel size= 10 cm

Figure 7e

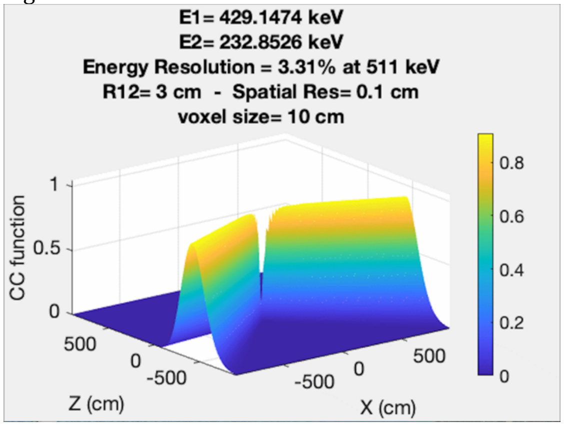
E1= 429.1474 keV
E2= 232.8526 keV
Energy Resolution = 3.31% at 511 keV
R12= 3 cm - Spatial Res= 0.1 cm
voxel size= 10 cm

Figure7f

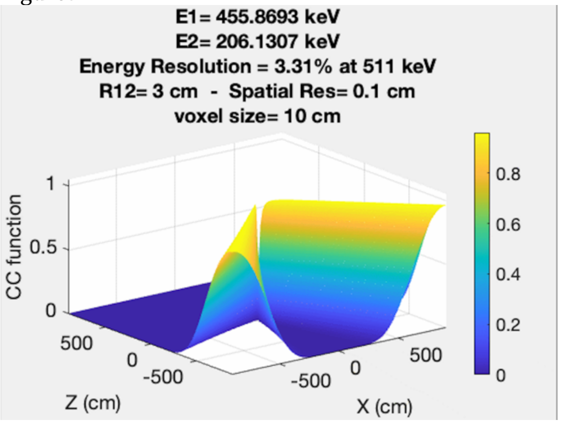
E1= 455.8693 keV
E2= 206.1307 keV
Energy Resolution = 3.31% at 511 keV
R12= 3 cm - Spatial Res= 0.1 cm
voxel size= 10 cm

Figure 7g

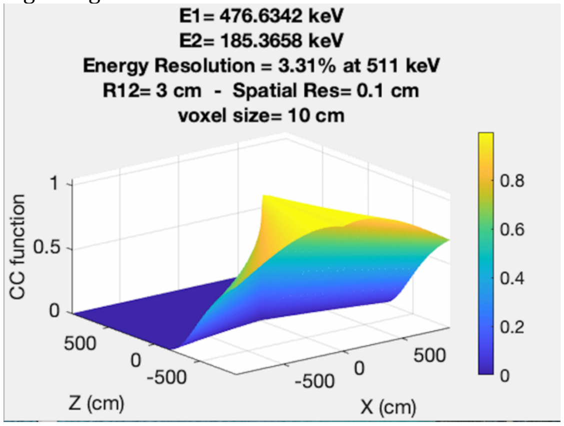
E1= 476.6342 keV
E2= 185.3658 keV
Energy Resolution = 3.31% at 511 keV
R12= 3 cm - Spatial Res= 0.1 cm
voxel size= 10 cm

Figure 7h

Figure 7 Caption

Figure 7. The series of images (7a)-(7h) display the CC function for parameters given in Equations (69), $R_{12} = 3.0\ cm$, and total energy $(E_1 + E_2)$ equal to 662 keV. The deposition energies E_1 and E_2 are assigned to provide Compton cone opening angles between 5° and 175°. [A .gif file of these images is provided in the Supplemental Materials.].

The imaging properties of the CC function are clearly displayed in Figure 7. The CC function is restricted to values 0≤CC≤1 and is expected to vanish unless the source voxel lies near the Compton cone of an event. Because the vertex of the Compton cone is at the origin and the cone axis this aligned with the z-axis of the grid, the Compton cone intersects the x-z plane in a wedge-shaped 'V'. The CC function clearly displays this 'V' wedge in Figures 7a-7f. These images also demonstrate the finite angular width of the Compton cone. As E_1 increases (and E_2 decreases), the angular width of the Compton cone increases. In Figure 7g angular width provides only limited resolution; and, in Figure 7h the CC has expanded to include virtually all voxels in the backscatter hemisphere! Thus, our observations in Appendix B that backscatter events cannot be expected to provide imaging information are confirmed by Figure 7h. As we will see, however, the problems associated with backscattered radiation do not necessarily degrade the overall Compton camera response.

Figure 7 also reveals a significant deficiency in our evaluation of the CC function. Every image in Figure 7 displays an unphysical "notch" in the CC function near the vertex of the cone. This "notch" is most visible in Figure 7e. This artificial depression of the CC function is a direct result of the approximations used in Appendix C. If a voxel is very near the first interaction ($R_s < 2L$), then the incident radiation can come from virtually any direction on the hemisphere facing that voxel. In terms of our parameters, this means that Σ_1 becomes very large and the approximations based on small values of Σ_1 fail. [In particular the approximation used in Equation (C.17) for the asymptotic expansion of the confluent hypergeometric function is no longer valid.]. Basically, the CC calculation assumes that the distribution of incident photons is restricted to a narrow angular region on the celestial sphere and, therefore, expects Σ_1 small. A voxel close to the detector violates this assumption. One method to remedy the problem is to find a better analytic approximation. Another method is to reduce the voxel size (L) in the immediate vicinity of the detector. In the absence of a better approximation, we currently recommend a reduction in voxel size for sources near the detector.

The Compton camera response is determined by $Rate(D1, D2)$ which, in addition to CC, includes numerous other factors. Perhaps the most obvious and significant of these is the R_s^{-2} rate dependence. The R_s^{-2} effect on the x-z plots implies that the calculated rate for voxels near the center will be 10^4 larger than voxels around the edges. In order to visualize the $Rate(D1, D2)$ function, the plots will display $[Rate(D1, D2) * R_s^2]$. The significance of this product goes beyond simple visualization of the plots. In the MLEM algorithm (and any maximum likelihood calculation based on Poisson statistics) the system matrix is divided by the voxel sensitivity (see Appendix F). If the Compton camera is stationary, the sensitivity is proportional to R_s^{-2}; so that, the system matrix divided by the sensitivity is proportional to $[Rate(D1, D2) * R_s^2]$—which is what appears in each update step of the MLEM algorithm.

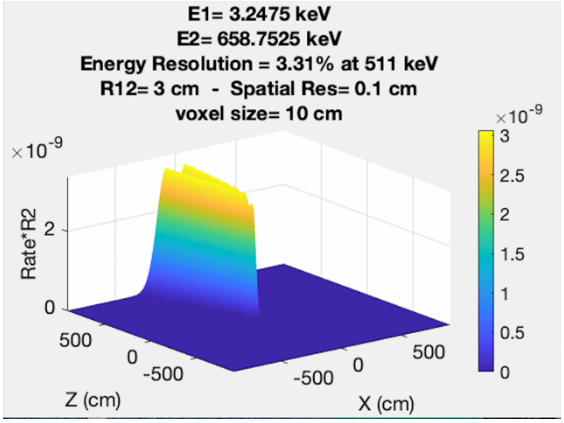
E1= 3.2475 keV
E2= 658.7525 keV
Energy Resolution = 3.31% at 511 keV
R12= 3 cm - Spatial Res= 0.1 cm
voxel size= 10 cm

Figure 8a

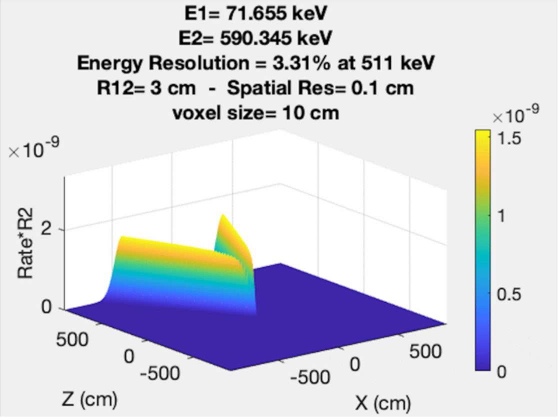
E1= 71.655 keV
E2= 590.345 keV
Energy Resolution = 3.31% at 511 keV
R12= 3 cm - Spatial Res= 0.1 cm
voxel size= 10 cm

Figure 8b

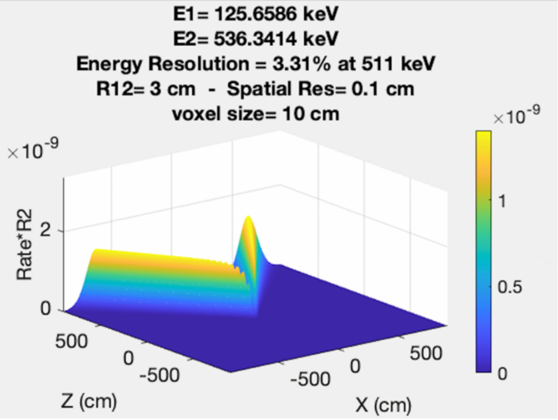
E1= 125.6586 keV
E2= 536.3414 keV
Energy Resolution = 3.31% at 511 keV
R12= 3 cm - Spatial Res= 0.1 cm
voxel size= 10 cm

Figure 8c

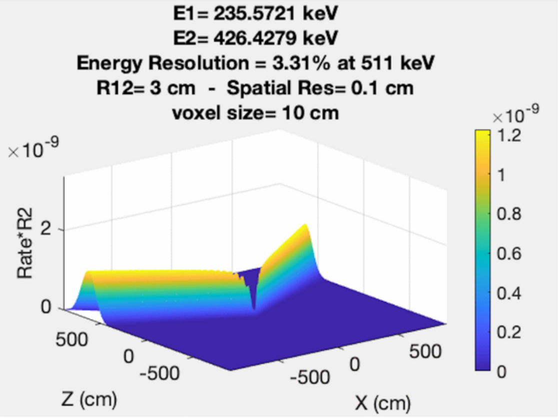
E1= 235.5721 keV
E2= 426.4279 keV
Energy Resolution = 3.31% at 511 keV
R12= 3 cm - Spatial Res= 0.1 cm
voxel size= 10 cm

Figure 8d

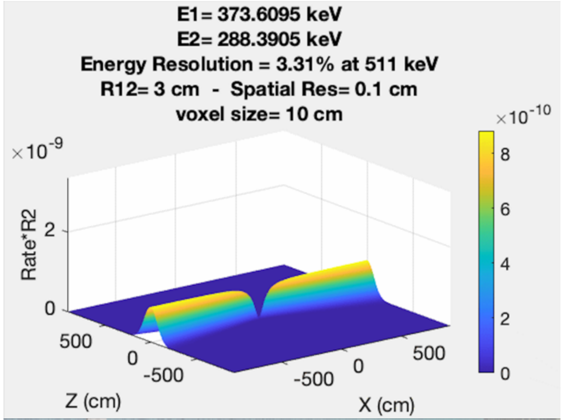
E1= 373.6095 keV
E2= 288.3905 keV
Energy Resolution = 3.31% at 511 keV
R12= 3 cm - Spatial Res= 0.1 cm
voxel size= 10 cm

Figure 8e

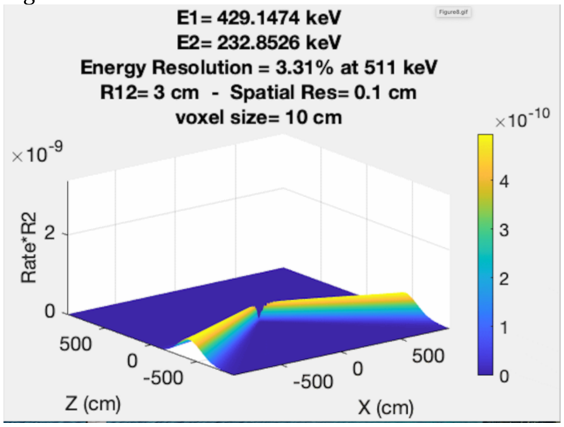
E1= 429.1474 keV
E2= 232.8526 keV
Energy Resolution = 3.31% at 511 keV
R12= 3 cm - Spatial Res= 0.1 cm
voxel size= 10 cm

Figure 8f

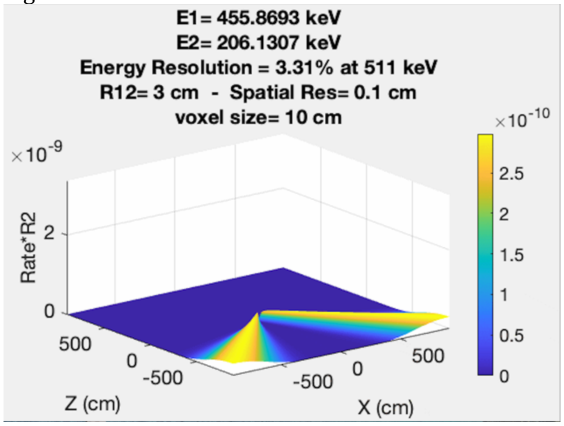
E1= 455.8693 keV
E2= 206.1307 keV
Energy Resolution = 3.31% at 511 keV
R12= 3 cm - Spatial Res= 0.1 cm
voxel size= 10 cm

Figure 8g

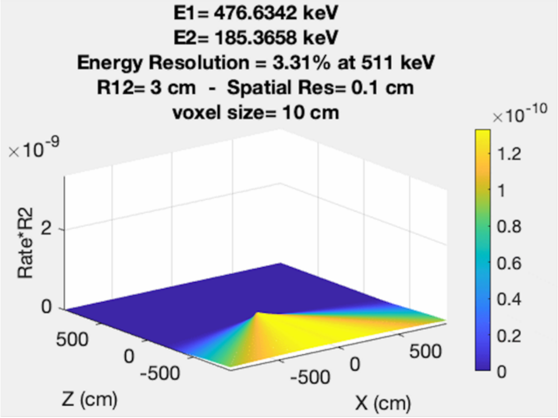
E1= 476.6342 keV
E2= 185.3658 keV
Energy Resolution = 3.31% at 511 keV
R12= 3 cm - Spatial Res= 0.1 cm
voxel size= 10 cm

Figure 8h

Figure 8 Caption

Figure 8. The series of images (8a)-(8h) display the function $[Rate(D1, D2) * R_s^2]$ for parameters given in Equations (69), $R_{12} = 3.0\,cm$, and total energy $(E_1 + E_2)$ equal to 662 keV. The deposition energies E_1 and E_2 are assigned to provide Compton cone opening angles between 5° and 175°. [A .gif file of these images is provided in the Supplemental Materials.].

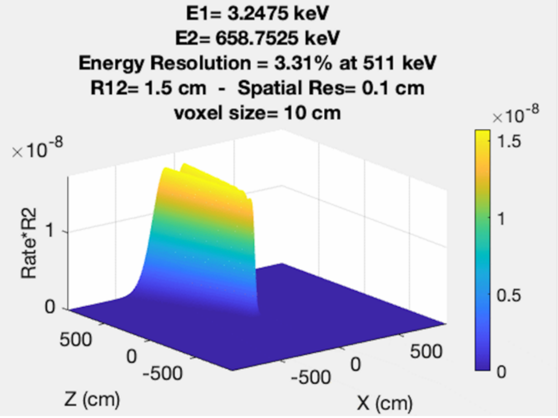

Figure 9a

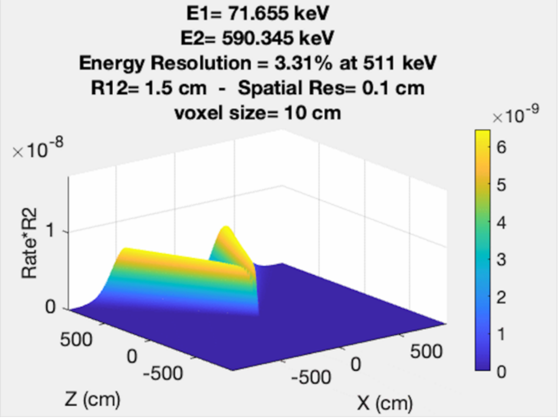

Figure 9b

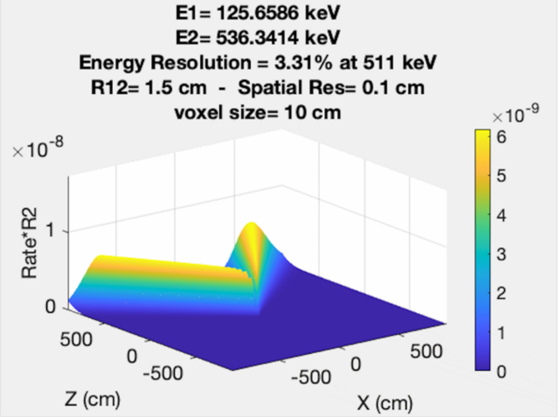

Figure 9c

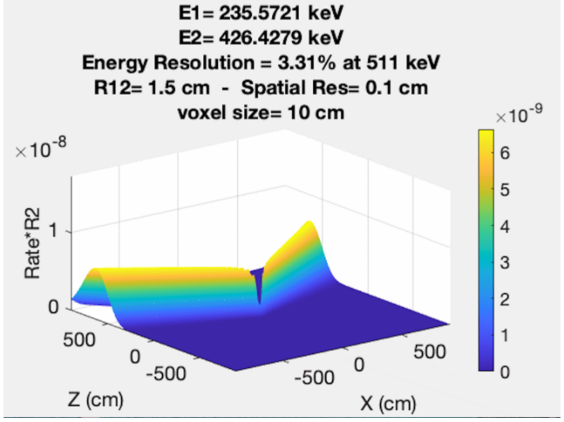

Figure 9d

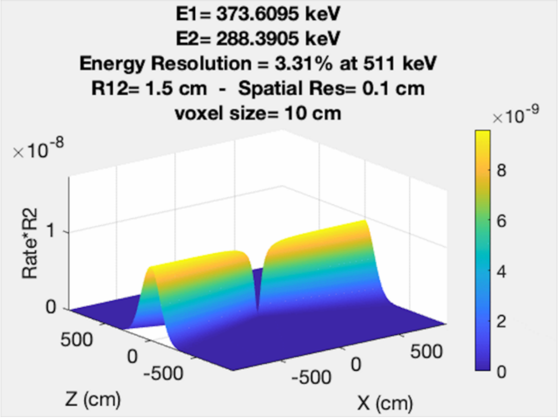

Figure 9e

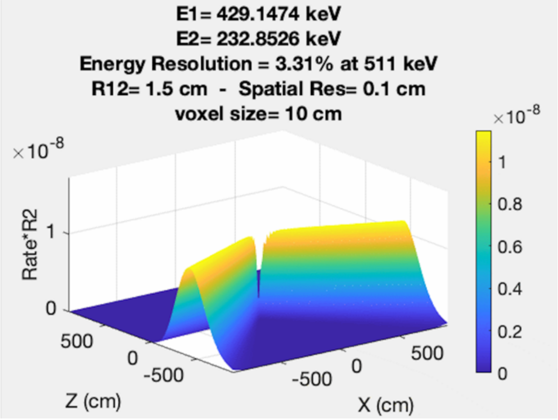

Figure 9f

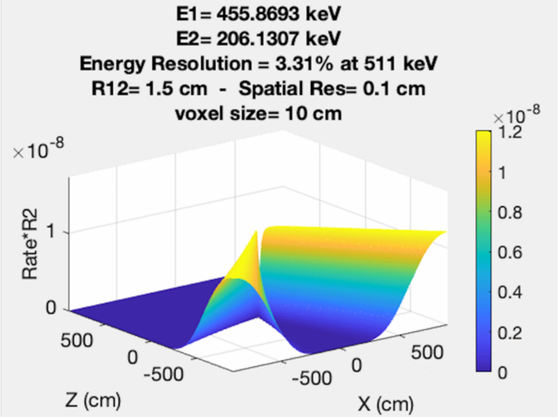

Figure 9g

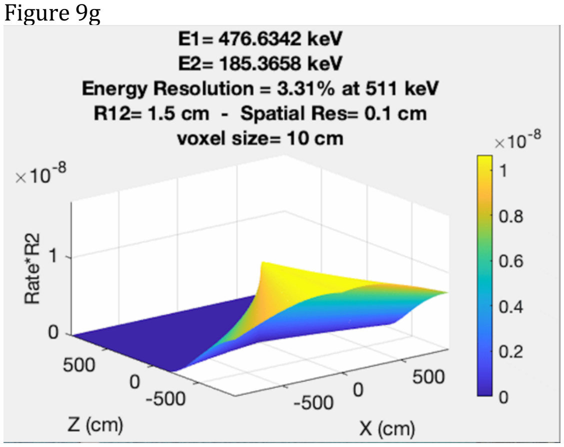

Figure 9h

Figure 9 Caption

Figure 9. The series of images (9a)-(9h) display the function $[Rate(D1, D2) * R_s^2]$ for parameters given in Equations (69), $R_{12} = 1.5\,cm$, and total energy $(E_1 + E_2)$ equal to 662 keV. The deposition energies E_1 and E_2 are assigned to provide Compton cone opening angles between 5° and 175°. [A .gif file of these images is provided in the Supplemental Materials.].

The product $[Rate(D1, D2) * R_s^2]$ is displayed in Figure 8 for the same detector configuration as was displayed in Figure 7 for the CC function. The difference is striking because the backscatter response is suppressed. Despite the catastrophic loss of angular resolution, the $[Rate(D1, D2) * R_s^2]$ for backscattered events drops by an order of magnitude compared with the rate for high-resolution, forward-scattered events. Comparison of Figures 7h and 8h reveals the same angular distribution, but the backscatter rate is so much lower that it poses little problem when back-projected onto the voxels. This fortunate state of affairs arises from the three terms mentioned earlier; namely, Att_{int}, $\left(\underline{\mu}_2 f_{PE2}\right)$, and X_{KN}^{12}. In fact, the major factor suppressing the undesirable backscatter rate is the Att_{int} term. This conclusion is verified by changing the parameter R_{12}.

The interaction distance R_{12} affects the $Rate(D1, D2)$ in three ways. First, the overall rate is proportional to R_{12}^{-2}. This effect is independent of the deposition energies and does not differentiate between forward or backward scattering. Second, the width parameter, Σ_2, is associated with cone-axis wobble, is proportional to R_{12}^{-1}, and is also independent of the deposition energies. Σ_2 affects the angular resolution via the CC function, but not the magnitude of the rate. Finally, R_{12} affects the Att_{int} term as given in Equation (69) by

$$Att_{int} = exp\left[-0.9 R_{12} \underline{\mu}_2\right]. \tag{69}$$

This last term depends on the E$_2$ energy through the $\underline{\mu}_2$ attenuation coefficient. The attenuation coefficient increases dramatically as E$_2$ decreases. Consequently, the Att_{int} term provides preferential suppression of backscattered radiation. Furthermore, larger R_{12} implies more suppression of backscattered response.

In Figure 9 the product $[Rate(D1, D2) * R_s^2]$ is displayed for the same parameters as Figure 8 – except the interaction separation $R_{12} = 1.5cm$ is reduced by half. A simple comparison of Figures 8h and 9h reveals that the backscattered response is no longer suppressed. The immediate conclusion is that larger separations between the interactions can suppress low resolution backscatter events. This phenomenon is examined further in the next section. In conclusion, one concludes that larger R_{12} is desirable for two reasons: (1) better angular resolution, and (2) natural suppression of backscatter rates.

VI. Interaction Sequencing and Coincident Detection Rates

At the beginning of this analysis, we assumed that the sequence of interactions was known. Consequently, the two interactions were labeled D1 and D2. In reality this is a bad assumption. Unless one of the sequences violates the backscatter limit (and is, therefore, prohibited by Compton kinematics), either sequence D1-D2 or D2-D1 is possible. Furthermore, no current instrumentation is expected to provide such sequencing information. [Compton events involving three or more interactions provide sufficient information for sequencing, but occur at such low rates that imaging becomes infeasible.] The ambiguity associated with interaction sequencing is apparently inherent to Compton cameras and must be handle as part of the image reconstruction process. Fortunately, only two alternative sequences are possible, so that evaluation of the rate for both sequences is provided by repeating the calculation for the alternative sequences. The idea is simply stated:

$$Rate(event) = Rate(D1, D2) + Rate(D2, D1) \tag{70}$$

where the $Rate(D2, D1)$ is evaluated with the exchange of interactions, i.e.,

$$\begin{array}{ccc} \vec{r}_1 \pm \lambda_1 & \Leftrightarrow & \vec{r}_2 \pm \lambda_2 \\ E_1 \pm \varepsilon_1 & \Leftrightarrow & E_2 \pm \varepsilon_2 \end{array}. \tag{71}$$

The rates in Equation (70) include the relative probabilities of both sequences. Each voxel provides a rate that is proportional to the probability of detection for the designated sequence. Because the alternate sequences are mutually exclusive, one can add the two rates. This implies that for many events the camera response will provide two Compton cones rather than one. Both cones will share the same axis; however, the vertices of these cones will be different ($\vec{r}_1$ or $\vec{r}_2$).

The application of Equation (70) is demonstrated in Figures 10 and 11 that display the same configurations as Figures 8 and 9, respectively. However, in Figures 10 and 11 the responses from both sequences are combined and displayed together. Because the voxel size is 10 cm and the interactions are separated (R_{12}) by only 1.5 or 3 cm, the displacement of the vertices is not apparent in these figures. The Compton kinematics for the D1D2 sequence gives the backscatter limit for E=662 keV at

$$E_1 \equiv \frac{2E^2}{(2E+m)} = 477.7\ keV\ and\ E_2 \equiv \frac{mE}{(2E+m)} = 184.3\ keV$$

so that energy ranges

$$0\ keV < E_1 < 477.7\ keV \quad and\ 184.3\ keV < E_2 < 662\ keV$$

are kinematically allowed. On the other hand, for the D2D1 sequence, the allow ranges are given by

$$0\ keV < E_2 < 477.7\ keV \quad and\ 184.3\ keV < E_1 < 662\ keV\ .$$

Thus, in the range $0\ keV < E_1 < 184.3\ keV$ only the D1D2 sequence is allowed, in the range $477.3\ keV < E_1 < 662\ keV$ only the D2D1 sequence is allowed, and, finally, in the range $184.3\ keV < E_1 < 477.7\ keV$ both the D1D2 and D2D1 sequences are allowed.

In Figure 10a only the D1D2 sequence is kinematically allowed, so only one cone appears. For Figures 10b-10f, both sequences are kinematically possible, so that two cones appear. As E1 increases both cones move toward the negative z-axis. Figure 10f is located very near the backscatter limit for the D1D2 sequence. In Figures 10g and 10h only the D2D1 sequence is allowed, so only one cone appears. The transition between Figures 10e and 10g is noteworthy because the cones of the D1D2 sequence fade away and the transition to the D2D1 sequence at the backscatter cutoff is smooth. This smooth transition can be attributed to the suppression of the backscattered events by the Att_{int} function for $R_{12} = 3\ cm$. If one sets $R_{12} = 1.5\ cm$, as shown in Figure 11, the transition is *not* smooth. Furthermore, the pathological loss of angular resolution attributable to backscatter radiation is evident. The problem is obvious in Figure 11f that occurs near the D1D2 backscatter limit. Because $R_{12} = 1.5\ cm$, the D1D2 sequence is no longer suppressed by the Att_{int} term and produces a broad distribution with no angular resolution. Superimposed on the broad D1D2 response is a relatively narrow cone from the D2D1 sequence that seems useful for imaging. One might simply want to drop the D1D2 sequence, but the data is incapable of distinguishing which sequence to attribute to event. Indeed, the actual event is most likely attributable to D1D2 and, therefore, not the more desirable D2D1 cone.

The problem described in the last paragraph poses a major dilemma for Compton imaging. Our proposed solution is inelegant but practical. Backscattered events for either the D1D2 or D2D1 sequence produce pathological loss of angular resolution. The loss of resolution arises from backscatter events with $(-1 < \mu < -0.8)$. One wants to discard such events; but, if one sequence is discarded, the other sequence must also be discarded (or one biases the data). Our solution is to discard both sequences if either is near the backscatter limit $(-1 < \mu < -0.8)$. Fortunately this strategy does not discard a large fraction of the events. Figure 12 and 13 show regions of the E_1-E_2 plane that are discarded by this strategy. As observed earlier, this rejection scheme is unnecessary if the Att_{int} term naturally suppresses the backscattered sequence. However, a determination of whether the attenuation term is adequate must be performed individually for each event because the attenuation distance will change.

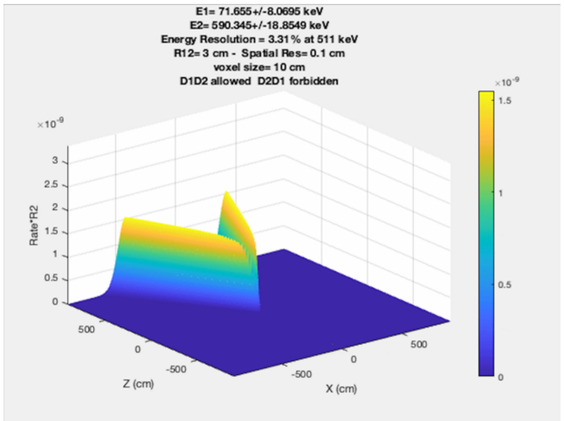

Figure 10a

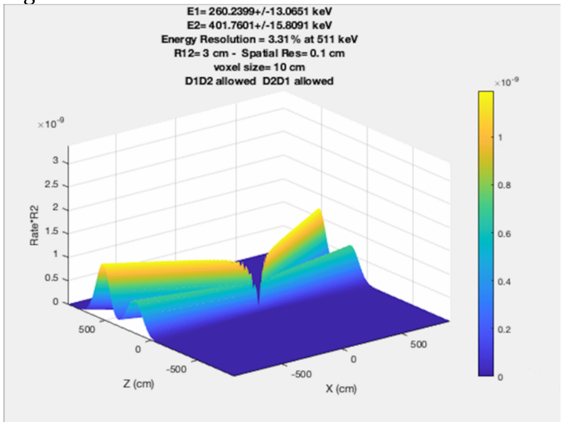

Figure 10b

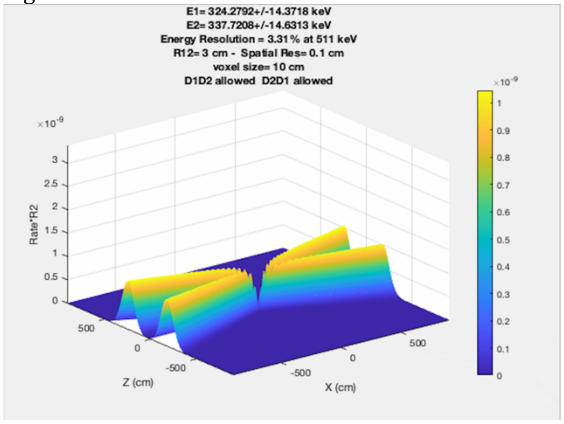

Figure 10c

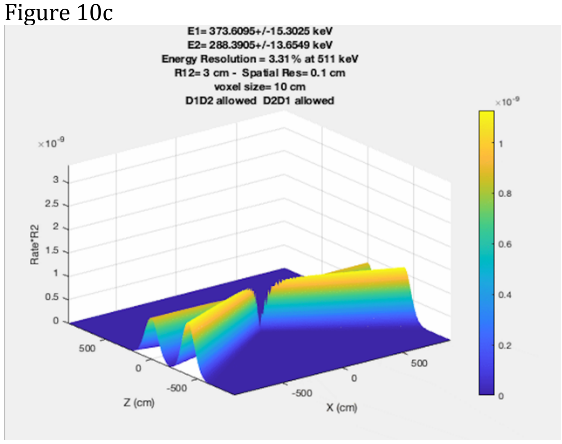

Figure 10d

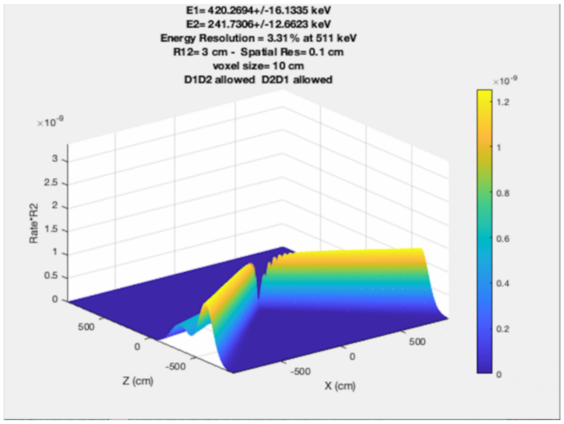

Figure 10e

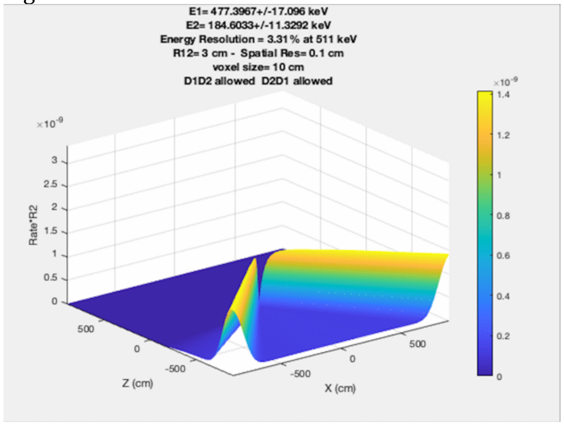

Figure 10f

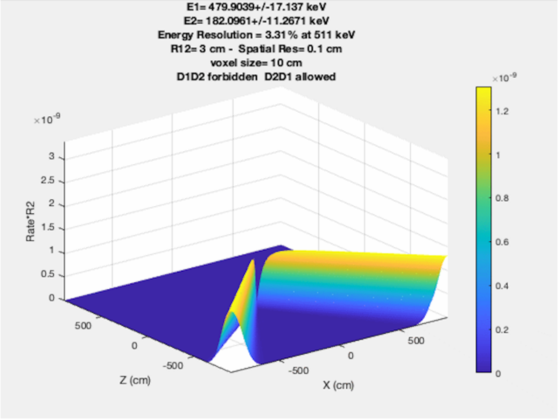

Figure 10g

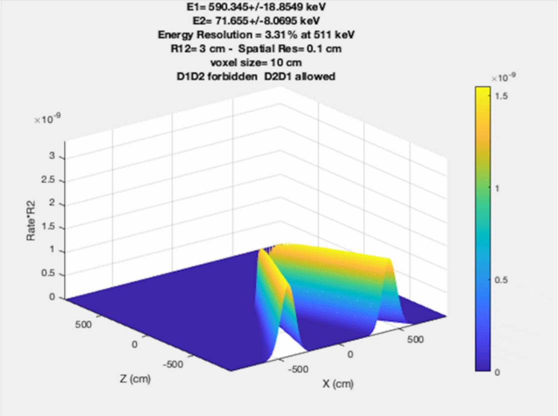

Figure 10h

Figure 10 Caption

Figure 10. The series of images (10a)-(10h) display the function $[Rate(event) * R_s^2]$ for parameters given in Equations (69), $R_{12} = 3.0cm$, and total energy $(E_1 + E_2)$ equal to 662 keV $[Rate(event) = Rate(D1, D2) + Rate(D2, D1)]$. The deposition energies E_1 and E_2 are assigned to provide Compton cone opening angles between 5° and 175°. [A .gif file of these images is provided in the Supplemental Materials.]. Because two sequences are possible and each sequence produces a different Compton cone, each image can potentially have two cones associated with the single event. The bottom line of the title in each image indicates whether the D1D2 and D2D1 sequences are allowed or forbidden by Compton kinematics. In Figure 10a only the sequence D1D2 is allowed. In Figure 10b-10f both sequences are allowed. In Figures 10f and 10g only sequence D2D1 is allowed. Indeed, Figures 10a and 10h are essentially the same event with opposite sequencing.

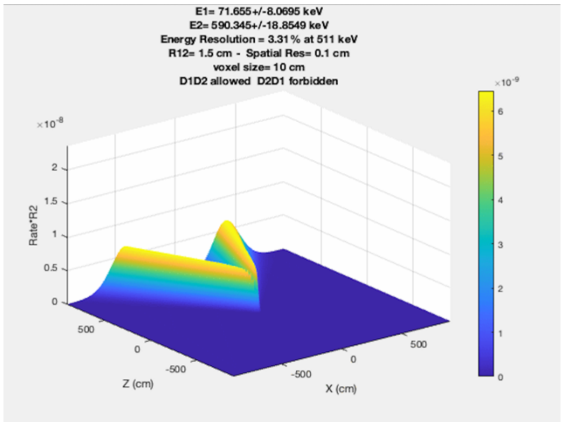

Figure 11a

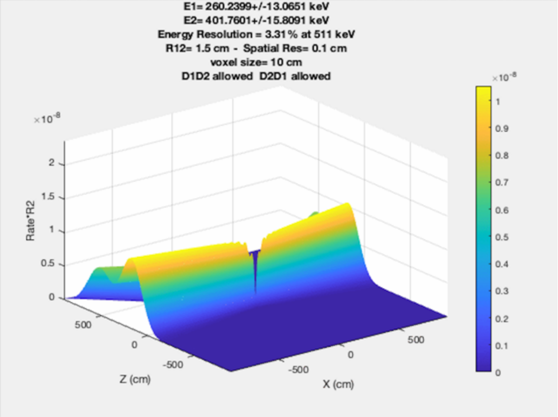

Figure 11b

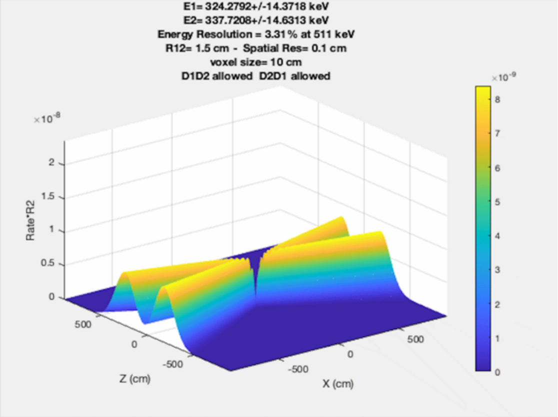

Figure 11c

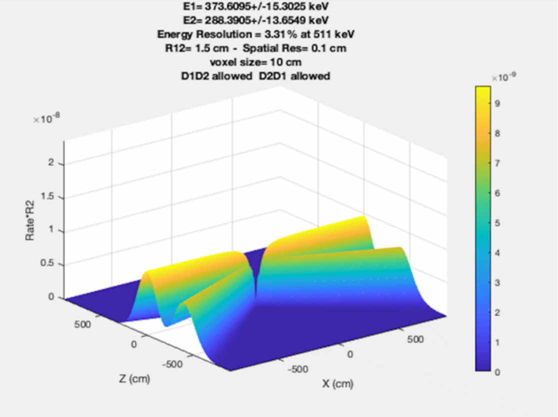

Figure 11d

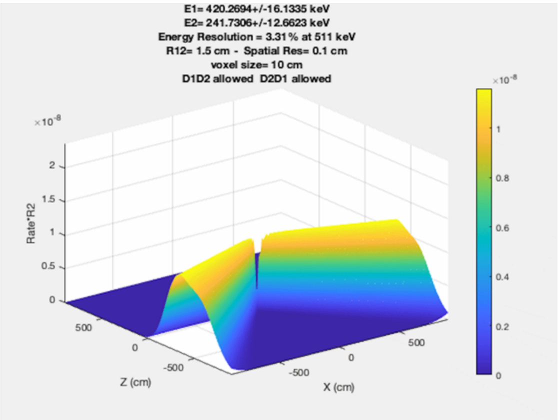

Figure 11e

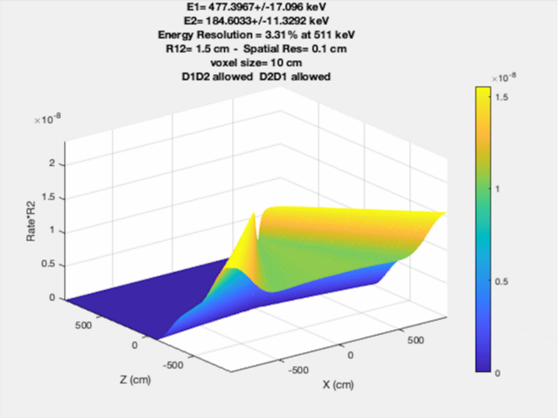

Figure 11f

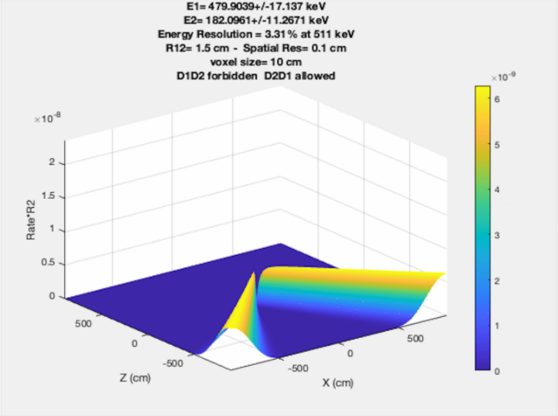

Figure 11g

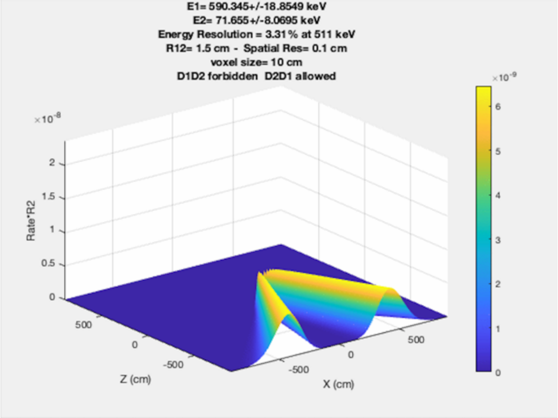

Figure 11h

Figure 11 Caption

Figure 11. The series of images (10a)-(10h) display the function $[Rate(event) * R_s^2]$ for parameters given in Equations (69), $R_{12} = 1.5\ cm$, and total energy $(E_1 + E_2)$ equal to 662 keV $[Rate(event) = Rate(D1, D2) + Rate(D2, D1)]$. The deposition energies E_1 and E_2 are assigned to provide Compton cone opening angles between 5° and 175°. [A .gif file of these images is provided in the Supplemental Materials.]. Because two sequences are possible and each sequence produces a different Compton cone, each image can potentially have two cones associated with the single event. The bottom line of the title in each image indicates whether the D1D2 and D2D1 sequences are allowed or forbidden by Compton kinematics. In Figure 11a only the sequence D1D2 is allowed. In Figure 11b-11f both sequences are allowed. In Figures 11g and 11h only sequence D2D1 is allowed. Indeed, Figures 11a and 11h are essentially the same event with opposite sequencing.

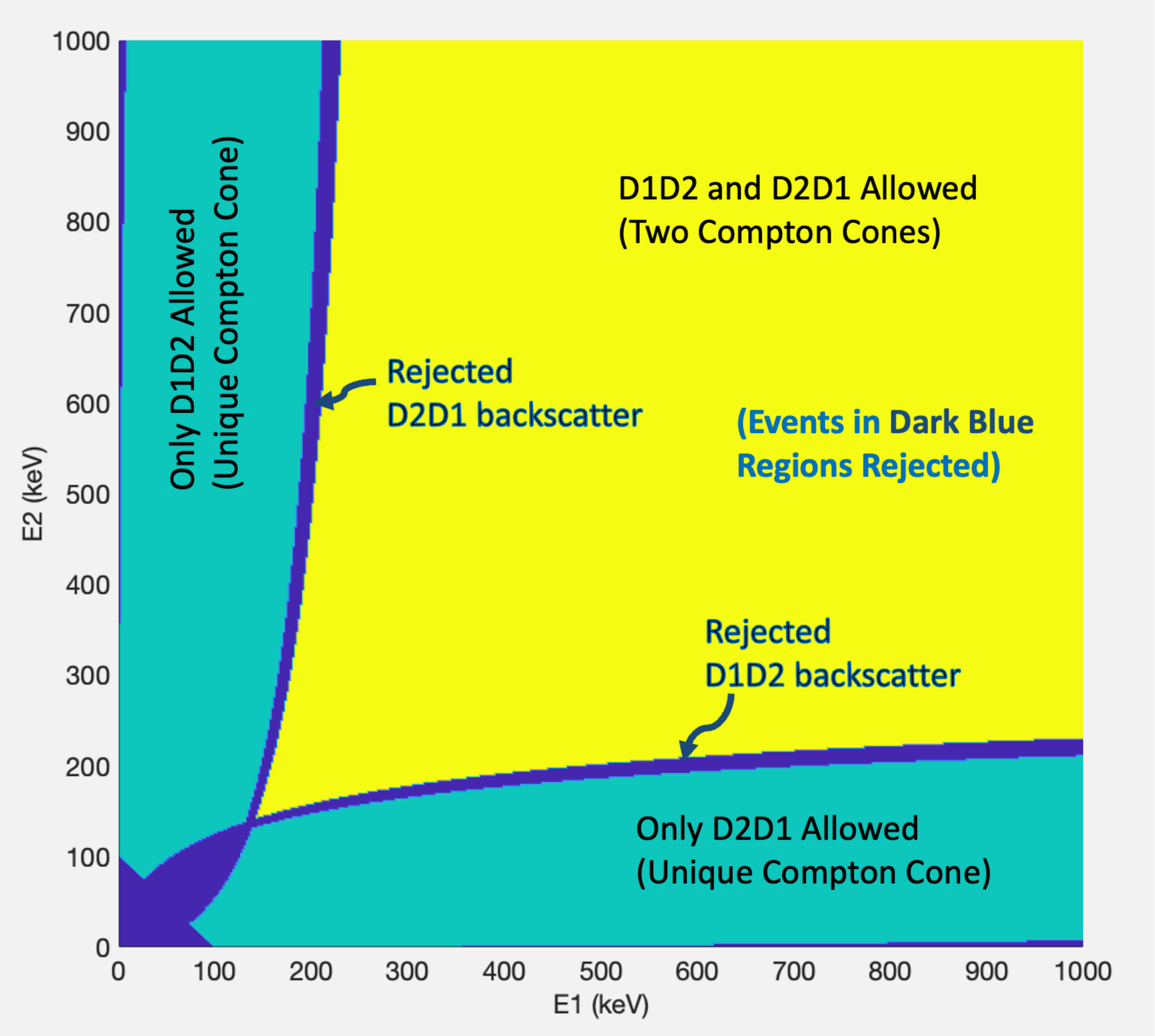

Figure 12. Regions of Allowed Events are plotted on the E_1-E_2 plane. For each combination of E_1 and E2 the color coding indicates the number of viable cones one can use in image reconstruction. In the yellow region, two cones corresponding to the alternative interaction sequences D1D2 and D2D1 are both viable. In the aqua-marine regions, only one sequence is allowed by Compton kinematics. In the dark blue regions, both sequences are allowed by Compton kinematics, but one of the sequences involves a backscatter event $(-1 < \mu < -0.8)$ with extremely poor angular resolution. Because one cannot distinguish whether the event is a good (forward scattered) or a bad (backscattered) event, one should reject the event as unsuitable for imaging.

E1 Acceptance Spectrum for 662 keV

Figure 13. The number of viable Compton cones are displayed as a function of E_1 for incident radiation at $E_{tot} = E_1 + E_2 = 662\ keV$. This plot is essentially a diagonal slice through Figure 12 along the line of constant E_{tot}. The crucial observation is that two gaps exist in the spectrum where the events should be rejected due to poor angular resolution associated with backscattered radiation. Fortunately, these gaps involve relatively narrow energy windows.

VII. Summary and Conclusions

The rate calculation presented in this report is suitable for applications with list-mode MLEM data from Compton cameras. A rigorous derivation of the rate calculation is presented that is then evaluated with realistic physical assumptions and analytic mathematical approximations. The careful exposition of these assumptions and approximations, especially in the appendices, assure that future researchers can adjust the results when/if the assumptions are violated or the approximations fail. The results accurately incorporate three sources of blurring that affect the camera resolution: (1) source voxel size, (2) spatial resolution of the interaction locations, and (3) the resolutions of the deposition energies. These sources of blurring directly affect the angular resolution of the Compton cone which becomes diffuse. The immediate effect is observed as spread of the Compton response from a narrow cone emanating from the vertex of the first interaction into a broad cone that expands to include neighboring voxels as one moves further from the vertex. The accurate description of this blurring is the major contribution of this report.

A major observation arising from this analysis is crucial role of energy resolution in the Compton camera response. The authors were surprised by the dramatic loss of angular resolution from backscattered events – so dramatic that one is forced to exclude such events from the analysis. The loss of angular resolution is caused by the blurring of the Compton cone; which, in turn, is caused by the limited energy resolution of the detectors. Although spatial resolution plays an important role in blurring the axis of the Compton cone, the effects of energy resolution seem more profound.

The problem of interaction sequencing has concerned researchers for decades. The backscatter limit can eliminate the ambiguity of sequencing for many events, especially those associated with small angle scattering. But inevitably, one is faced with a large fraction of events for which the sequencing is ambiguous and the imaging effects significant. Over the years researchers devised numerous strategies to either (1) select one sequence as more probable, or (2) include a weighted average of the alternate sequences. In this report, the second strategy is firmly supported. The rate calculation provides an accurate comparison of the alternative sequences. Without *a priori* information about the appropriate choice, one must simply add the rates of the two possible sequences for each voxel and let the relative rates determine the relative probabilities. Selecting a specific sequence for each event (whether well-founded or not) distorts the entire strategy of a maximum likelihood. Image reconstruction is a mapping from one distribution (data) to another (sources); not an assignment of each event to a specific source or sequence. As displayed in Section VI, the rate calculation provides an unambiguous method of calculating the system matrix without the selection of a specific sequence. The maximum likelihood algorithm based on the combined system matrix for both sequences provides the most probable assignment of the sources (and, implicitly, the sequences) based on the accumulated data – not a single event. Selection of a specific sequence for an event overrides the maximum likelihood algorithm (which considers all the data) with the limited information about that specific event; and, therefore, should be avoided.

Based on this principle, we assert that any viable interaction sequence should be included in the Compton rates and, therefore the rates of both alternate sequences should be added together in calculating the system response. Lamentably, events involving backscatter $(-1 < \mu < -0.8)$ exhibit such poor angular resolution that their inclusion in image reconstruction is dubious. Exclusion of such events implies exclusion of both sequences, even though one of the sequences which seems perfectly viable. One cannot distinguish whether the event is good (forward scattered) of bad (backscattered) events based on the data. Our recommendation is that both sequences be excluded. Fortunately, the energy bands of rejected sequences are relatively narrow (as demonstrated in Figures 12 and 13).

The rate calculation present in this paper has some obvious flaws. Most of these flaws can be traced to the approximations used in the evaluation of the CC function in Appendix C. Indeed, this report has been revised dozens of times in the past few years as better methods were found to handle anomalous results resulting from inadequate approximations. The current CC function will, undoubtedly, be succeeded by further improvements. However, the basic framework for the Compton camera response as expounded in Section II-VI is both rigorous and general enough to accommodate future revisions.

Appendix A. Blurring of the direction of the Compton Cone-Axis due to the Limited Spatial Resolution of the Detector

Embedded within the calculation of the detector rate is a crucial term [Equation (52)] that describes the blurring of the Compton-cone axis due to the uncertainties in the interaction positions. For notational purposes this term is defined as the function CA (cone axis):

$$CA(\vec{\omega}) \equiv \iiint d^3\vec{x}_1 \iiint d^3\vec{x}_2 \; \frac{1}{\left|\vec{x}_1-\vec{x}_2\right|^2} \; \delta^2\left(\vec{\omega}, \frac{\vec{x}_2-\vec{x}_1}{|\vec{x}_1-\vec{x}_2|}\right) \; D_x(\vec{x}_2|\vec{r}_2,\lambda_2) \; D_x(\vec{x}_1|\vec{r}_1,\lambda_1) \tag{A.1}$$

where the argument $\vec{\omega}$ indicates the actual Compton axis; whereas, r_1 and r_2 are the reported locations of the interactions. The function CA is, in some sense, a weighted distribution of actual axis direct $\vec{\omega}$ around the "measured" axis $\vec{\alpha}$ determined from r_1 and r_2. This mathematical appendix provides an analytical evaluation of the CA term that is used for the "realistic" detector models in sections V and VI.

For an "ideal" detector as defined in Equation (41), there is no blurring because the positions are known exactly; thus, the crucial Compton-axis (CA) term is given by

$$CA^{ideal}(\vec{\omega}) = \frac{(2\pi)^3\,\lambda_1^3\lambda_2^3}{R_{12}^2}\;\delta^2(\vec{\alpha},\vec{\omega}) \tag{A.2}$$

so that, the $\mathrm{CA}^{\mathrm{ideal}}$ weighting factor assures that the Compton-cone axis $\vec{\omega}$ is exactly aligned with the vector $\vec{\alpha}$ connecting the two interaction locations. Furthermore, the $\mathrm{CA}^{\mathrm{ideal}}$ satisfies the integral identity:

$$\iint_{S^2} d^2\vec{\omega}\;\; CA^{ideal}(\vec{\omega}) = \frac{(2\pi)^3\,\lambda_1^3\lambda_2^3}{R_{12}^2} \tag{A.3}$$

This identity is significant because, although the $\mathrm{CA}^{\mathrm{ideal}}$ is concentrated to a single direction, the expected rate will be proportional to the integral in Equation (A.3). As we will see, the "realistic" detector model yields a similar result, despite distributing $\vec{\omega}$ over a finite region on the celestial sphere.

For a "realistic" detector model [Equation (42)], the D_x functions are Gaussians, which simplifies the evaluation of Equation (A.1). In particular, one finds that

$$D_x^{real}(\vec{x}_1|\vec{r}_1,\lambda_1)\; D_x^{real}(\vec{x}_2|\vec{r}_2,\lambda_2) = \exp\left[-\frac{|\vec{x}_1-\vec{r}_1|^2}{2\lambda_1^2} - \frac{|\vec{x}_2-\vec{r}_2|^2}{2\lambda_2^2}\right] . \tag{A.4}$$

The integrals in Equation (A.1) are simplified by a simple change in variables; namely, $(\vec{x}_1,\vec{x}_2) \Leftrightarrow (\vec{\xi}_1,\vec{\xi}_2)$ where

$$\vec{\xi}_1 = \frac{\lambda_2^2\vec{x}_1+\lambda_1^2\vec{x}_2}{(\lambda_1^2+\lambda_2^2)}\;, \qquad \vec{\xi}_2 = \vec{x}_2-\vec{x}_1\;; \tag{A.5}$$

$$\vec{x}_1 = \vec{\xi}_1 - \frac{\lambda_1^2}{(\lambda_1^2+\lambda_2^2)}\vec{\xi}_2 \qquad \vec{x}_2 = \vec{\xi}_1 + \frac{\lambda_2^2}{(\lambda_1^2+\lambda_2^2)}\vec{\xi}_2\;.$$

with the supplemental constant vector

$$\vec{W} \equiv \frac{\lambda_2^2\vec{r}_1+\lambda_1^2\vec{r}_2}{(\lambda_1^2+\lambda_2^2)}\;. \tag{A.6}$$

A simple evaluation of the Jacobian reveals that

$$\iiint d^3\vec{x}_1 \iiint d^3\vec{x}_2 = \iiint d^3\vec{\xi}_1 \iiint d^3\vec{\xi}_2 \ ; \tag{A.7}$$

whereas, in the new variables, the product in Equation (A.4) becomes

$$\begin{aligned} &D_x^{real}(\vec{x}_1|\vec{r}_1,\lambda_1)\, D_x^{real}(\vec{x}_2|\vec{r}_2,\lambda_2) \\ &\qquad = \exp\left[-\frac{(\lambda_1^2+\lambda_2^2)\left|\vec{\xi}_1-\vec{W}\right|^2}{2\lambda_1^2\lambda_2^2} - \frac{\left|\vec{\xi}_2-R_{12}\vec{\alpha}\right|^2}{2(\lambda_1^2+\lambda_2^2)}\right] . \end{aligned} \tag{A.8}$$

Rewriting Equation (A.1) in terms of the new variables, one finds that the integrals decouple and

$$\begin{aligned} CA^{real}(\vec{\omega}) = \iiint d^3\vec{\xi}_1 \ \exp\left[-\frac{(\lambda_1^2+\lambda_2^2)\left|\vec{\xi}_1-\vec{W}\right|^2}{2\lambda_1^2\lambda_2^2}\right] \\ \iiint d^3\vec{\xi}_2 \ \frac{1}{\left|\vec{\xi}_2\right|^2} \ \exp\left[-\frac{\left|\vec{\xi}_2-R_{12}\vec{\alpha}\right|^2}{2(\lambda_1^2+\lambda_2^2)}\right] \delta^2\left(\vec{\omega},\frac{\vec{\xi}_2}{\left|\vec{\xi}_2\right|}\right) . \end{aligned} \tag{A.9}$$

In Equation (A.9) the integrand of the $\vec{\xi}_1$ integral is a simple 3D Gaussian and is trivially evaluated; whereas, the integral over $\vec{\xi}_2$, due to the delta function, reduces to a line integral along a ray originating at the origin through a displaced Gaussian that produces an error function. The Inequalities (15a) allow one to approximate the error function term as a Heaviside function, so that

$$\begin{aligned} CA^{real}(\vec{\omega}) &= \frac{(2\pi)^{3/2}\lambda_1^3\lambda_2^3}{(\lambda_1^2+\lambda_2^2)^{3/2}} \int_0^\infty d\xi \ \exp\left[-\frac{|\xi\vec{\omega}-R_{12}\vec{\alpha}|^2}{2(\lambda_1^2+\lambda_2^2)}\right] \\ &\cong \frac{(2\pi)^2\lambda_1^3\lambda_2^3}{(\lambda_1^2+\lambda_2^2)} \ \Theta(\vec{\omega}\cdot\vec{\alpha}) \ \exp\left\{-\frac{R_{12}^2}{2(\lambda_1^2+\lambda_2^2)}\left[1-(\vec{\omega}\cdot\vec{\alpha})^2\right]\right\} . \end{aligned} \tag{A.10}$$

The approximate function given in the second line of Equation (A.10) is used as CA in the remainder of this analysis. [One should note that the Gaussian approximation for the D^{real} function is responsible for this simple evaluation of 6 of the 12 integrals in Equation (47).]

A comparison of Equations (A.2) and (A.10) indicates that both the "ideal" and "real" detector models produce functions $CA(\vec{\omega})$ that are strongly peaked in the direction $\vec{\omega} = \vec{\alpha}$. The major difference between CA^{ideal} and CA^{real} seems to be the R_{12} dependence. The magnitude of CA^{ideal} is explicitly dependent of R_{12}, whereas CA^{real} is only dependent on R_{12} through a narrowing of the angular dependence. This behavior is correct and is exactly what should be expected.

The function CA^{real} in Equation (A.10) can verified by checking that, in the limit $R_{12} >> \lambda_i$ (i.e., large separation between the interactions), CA^{real} reproduces the R_{12}^{-2} behavior of function CA^{ideal} demonstrated in Equation (A.3). The function CA only appears in our calculation within integrals over $\vec{\omega}$. If one integrates CA^{real} over $\vec{\omega}$, one finds that

$$\iint_{S^2} d^2\vec{\omega}\; CA^{real}(\vec{\omega}) = \frac{(2\pi)^2\lambda_1^3\lambda_2^3}{(\lambda_1^2+\lambda_2^2)}\; 2\pi \int_0^1 d\mu\; exp\left[-\frac{R_{12}^2(1-\mu^2)}{2(\lambda_1^2+\lambda_2^2)}\right] \tag{A.11}$$

$$= \frac{(2\pi)^3\lambda_1^3\lambda_2^3}{(\lambda_1^2+\lambda_2^2)}\; exp\left[-\frac{R_{12}^2}{2(\lambda_1^2+\lambda_2^2)}\right]\; {}_1F_1\left(\frac{1}{2},\frac{3}{2};\frac{R_{12}^2}{2(\lambda_1^2+\lambda_2^2)}\right)$$

where $_1F_1$ is the confluent hypergeometric function. The asymptotic expansion of the confluent hypergeometric function gives that

$${}_1F_1\left(\frac{1}{2},\frac{3}{2};z\right) \xrightarrow[z\gg 1]{} \frac{1}{2z}\exp(z) \tag{A.12}$$

so that

$$\iint_{S^2} d^2\vec{\omega}\; CA^{real}(\vec{\omega}) \xrightarrow[R_{12}^2\gg(\lambda_1^2+\lambda_2^2)]{} \frac{(2\pi)^3\lambda_1^3\lambda_2^3}{R_{12}^2} \quad . \tag{A.13}$$

A comparison of Equation (A.13) and Equation (A.3) shows that the integral of CA^{real} over the 2-sphere yields the same result as CA^{ideal} in the limit of R_{12} much larger than the spatial resolution. This observation verifies that for $R_{12} \gg \lambda_i$, CA^{real} is approximated by CA^{ideal}.

Appendix B. Blurring of the Opening Angle of the Compton Cone due to the Limited Energy Resolution of the Detector

The goal of this Appendix is the evaluation OA for common spectra in approximate analytic expressions that can be used for the integration of Equation (57). The opening angle of the Compton cone is determined by relativistic kinematics based on the energies deposited at the two interaction sites, E_1 and E_2; i.e., μ in Equation (12). If the energies were exactly known, then the cone would be characterized by an opening angle θ_{kin} defined by the $\cos\theta_{kin} = \mu(E_1, E_2)$ as defined in Equation (12). Because these energies are measured with finite resolution, the Compton cone is blurred. This blurring is characterized by a blurring function that is defined in Equation (53) in terms of integrals over the energy ranges consistent with the measurements. The function OA, the 'opening angle' function, is defined by

$$OA(\upsilon) \equiv \int_0^{\infty} dk\ A(k)\ D_E\left(\frac{k^2(1-\upsilon)}{m+k(1-\upsilon)}\middle|\, E_1, \varepsilon_1\right)\ D_E\left(\frac{mk}{m+k(1-\upsilon)}\middle|\, E_2, \varepsilon_2\right)\ . \tag{B.1}$$

where $\upsilon \left[= \left(\vec{\Omega}_1 \cdot \vec{\Omega}_2\right)\right]$ is the *actual* cosine of the opening angle of the Compton cone. The function OA(υ) describes the distribution of υ given the observed data (E_i,ε_i). In this appendix the function OA is evaluated for (1) D_E^{real} as defined by Gaussian functions in Equation (42), and for (2) Gaussian source distributions, A(k) that can represent emissions from common spectra. The D_E functions represent the distribution of actual energies, k, consistent with the measured energies, E_i, with resolutions, ε_i. Because the D_E functions are narrow Gaussians, one can create accurate approximations for OA based on the local behavior of A(k) in the vicinity of the peaks. For practical purposes, one wants a generic expression for OA that can be easily evaluated and adapted to many different spectra. The most obvious choice for such a source A(k) is another Gaussian function; namely,

$$A(k) = \frac{A^*}{\sqrt{2\pi}\Sigma_s}\ exp\left[-\frac{(k-E_s)^2}{2\Sigma_s^2}\right] \tag{B.2}$$

where A^* has dimensions $[(counts)(sec^{-1})(m^{-3})]$ and both E_s and Σ_s have units of energy $[(keV)]$. The energy E_s corresponds to the emission energy of the source; whereas, Σ_s represents the width of energy window. In the limit $\Sigma_s \to 0$, A(k) approximates a line spectrum; whereas, in the limit $\Sigma_s \to \infty$, A(k) can approximate a uniform background distribution. Intermediate values of Σ_s approximate spectra associated with finite energy bins. Table B.1 shows how the Gaussian function in Equation (B.2) can be used to approximate useful spectra associated with spectral lines and finite energy bins. [The approximation for energy bins is demonstrated in Appendix G.]

Table B.1

	$A^*\left[\frac{counts}{sec \cdot m^3}\right]$	$E_s[keV]$	$\Sigma_s[keV]$	**Functional Equivalent A(k)** $\left[\frac{counts}{sec \cdot keV \cdot m^3}\right]$
Spectral Line	A^*_{line}	E_{line}	$(\lim \varepsilon \to 0)\ \varepsilon m$	$A^*_{line}\,\delta(k - E_{line})$
Energy Bin	A^*_{bin}	E_{bin}	$\Delta_{bin}/\sqrt{12}$	$\frac{A^*_{bin}}{\Delta_{bin}}\Xi(k - E_{bin}\lvert\Delta_{bin})$

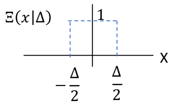

Insight into the integral of Equation (B.1) is obtained from an examination of the 2D distribution

$$p(k_1,k_2) \propto exp\left[-\frac{(k_1-E_1)^2}{2\varepsilon_1^2}\right] exp\left[-\frac{(k_2-E_2)^2}{2\varepsilon_2^2}\right] exp\left[-\frac{(k_1+k_2-E_S)^2}{2\Sigma_S^2}\right] \tag{B.3}$$

which emulates the integrand of that equation. Just as k represents the actual incident energy, k_1 and k_2 represent the actual deposition energies in the detectors. The maximum of this 2D Gaussian product occurs at the point

$$k_{1,max} = \frac{(\varepsilon_2^2+\Sigma_S^2)E_1+\varepsilon_1^2(E_S-E_2)}{(\varepsilon_1^2+\varepsilon_2^2+\Sigma_S^2)} \quad \text{and} \quad k_{2,max} = \frac{(\varepsilon_1^2+\Sigma_S^2)E_2+\varepsilon_2^2(E_S-E_1)}{(\varepsilon_1^2+\varepsilon_2^2+\Sigma_S^2)}. \tag{B.4a}$$

[It turns out that the values $k_{i,max}$ are also the mean values of k_i for the distribution $p(k_1,k_2)$.] If one converts the k_1 and k_2 variables into the k and υ variables of Equation (B.1), the maxima of k and υ occur at

$$k_{1,max} = \frac{k_{max}^2(1-\upsilon_{max})}{[m+k_{max}(1-\upsilon_{max})]} \qquad k_{2,max} = \frac{mk_{max}}{[m+k_{max}(1-\upsilon_{max})]} \tag{B.4b}$$

so that

$$k_{max} = k_{1,max} + k_{2,max} = \frac{(\varepsilon_1^2+\varepsilon_2^2)E_S+\Sigma_S^2(E_1+E_2)}{(\varepsilon_1^2+\varepsilon_2^2+\Sigma_S^2)} \tag{B.4c}$$

and

$$\upsilon_{max} = 1 - \frac{mk_{1,max}}{k_{max}k_{2,max}} = 1 - \frac{m(\varepsilon_1^2+\varepsilon_2^2+\Sigma_S^2)[(\varepsilon_2^2+\Sigma_S^2)E_1+\varepsilon_1^2(E_S-E_2)]}{[(\varepsilon_1^2+\varepsilon_2^2)E_S+\Sigma_S^2(E_1+E_2)][(\varepsilon_1^2+\Sigma_S^2)E_2+\varepsilon_2^2(E_S-E_1)]}. \tag{B.4d}$$

N.B. if $E_s = E_1 + E_2$, then $\upsilon_{max} = \mu(E_1, E_2)$ as defined in Equation (12). One anticipates that υ_{max} is the maximum of the integrand of Equation (B.1). The detector functions in Equation (B.1) are defined as Gaussians

$$D_E\left(\frac{k^2(1-\upsilon)}{m+k(1-\upsilon)}\middle| E_1, \varepsilon_1\right) \equiv exp\left[-\frac{\left(\frac{k^2(1-\upsilon)}{m+k(1-\upsilon)}-E_1\right)^2}{2\varepsilon_1^2}\right] \quad \text{(B.5a)}$$

$$D_E\left(\frac{mk}{m+k(1-\upsilon)}\middle| E_2, \varepsilon_2\right) \equiv exp\left[-\frac{\left(\frac{mk}{m+k(1-\upsilon)}-E_2\right)^2}{2\varepsilon_2^2}\right]. \quad \text{(B.5b)}$$

Insight into these functions from Equations (B.4) imply that the arguments of the Gaussians be written as

$$\frac{k^2(1-\upsilon)}{m+k(1-\upsilon)} - E_1 = \left(\frac{k^2(1-\upsilon)}{m+k(1-\upsilon)} - k_{1,max}\right) + \left(k_{1,max} - E_1\right)$$

$$\frac{mk}{m+k(1-\upsilon)} - E_2 = \left(\frac{mk}{m+k(1-\upsilon)} - k_{2,max}\right) + \left(k_{2,max} - E_2\right)$$

where one evaluates the bracketed terms as

$$\left(k_{1,max} - E_1\right) = \frac{\varepsilon_1^2}{\left(\varepsilon_1^2+\varepsilon_2^2+\Sigma_s^2\right)}\left(E_s - E_1 - E_2\right) \quad \text{(B.6a)}$$

$$\left(k_{2,max} - E_2\right) = \frac{\varepsilon_2^2}{\left(\varepsilon_1^2+\varepsilon_2^2+\Sigma_s^2\right)}\left(E_s - E_1 - E_2\right) \quad \text{(B.6b)}$$

$$\left(\frac{k^2(1-\upsilon)}{m+k(1-\upsilon)} - k_{1,max}\right) = \frac{\left(kk_{max}-k_2k_{2,max}\right)}{kk_{max}}\left(k - k_{max}\right) - \frac{k_2k_{2,max}}{m}\left(\upsilon - \upsilon_{max}\right) \quad \text{(B.7a)}$$

and $$\left(\frac{mk}{m+k(1-\upsilon)} - k_{2,max}\right) = \frac{k_2k_{2,max}}{kk_{max}}\left(k - k_{max}\right) + \frac{k_2k_{2,max}}{m}\left(\upsilon - \upsilon_{max}\right). \quad \text{(B.7b)}$$

In the vicinity of the Gaussian peak [$k \cong k_{max}$ and $k_2 \cong k_{2,max}$; i.e., the region making the major contribution to the integral in Equation (B.1)], Equations (B.7a&7b) can be approximated by

$$\left(\frac{k^2(1-\upsilon)}{m+k(1-\upsilon)} - k_{1,max}\right) \cong \frac{\left(k_{max}^2-k_{2,max}^2\right)}{k_{max}^2}\left(k - k_{max}\right) - \frac{k_{2,max}^2}{m}\left(\upsilon - \upsilon_{max}\right) \quad \text{(B.8a)}$$

$$\left(\frac{mk}{m+k(1-\upsilon)} - k_{2,max}\right) \cong \frac{k_{2,max}^2}{k_{max}^2}\left(k - k_{max}\right) + \frac{k_{2,max}^2}{m}\left(\upsilon - \upsilon_{max}\right). \quad \text{(B.8b)}$$

For convenience, one defines

$$\kappa \equiv k - k_{max} \quad \text{(B.9a)}$$

$$\Delta\upsilon \equiv \upsilon - \upsilon_{max} \quad \text{(B.9b)}$$

$$\Delta E \equiv E_s - E_1 - E_2 \tag{B.9c}$$

so that

$$D_E\left(\frac{k^2(1-\upsilon)}{m+k(1-\upsilon)}\middle| E_1, \varepsilon_1\right) \cong exp\left[-\frac{\left(\frac{\left(k_{max}^2-k_{2,max}^2\right)}{k_{max}^2}\kappa-\frac{k_{2,max}^2}{m}(\Delta\upsilon)+\frac{\varepsilon_1^2}{(\varepsilon_1^2+\varepsilon_2^2+\Sigma_S^2)}(\Delta E)\right)^2}{2\varepsilon_1^2}\right] \tag{B.10a}$$

and $$D_E\left(\frac{mk}{m+k(1-\upsilon)}\middle| E_2, \varepsilon_2\right) \cong exp\left[-\frac{\left(\frac{k_{2,max}^2}{k_{max}^2}\kappa+\frac{k_{2,max}^2}{m}(\Delta\upsilon)+\frac{\varepsilon_2^2}{(\varepsilon_1^2+\varepsilon_2^2+\Sigma_S^2)}(\Delta E)\right)^2}{2\varepsilon_2^2}\right]. \tag{B.10b}$$

Finally, one writes Equation (B.2) as

$$A(k) = \frac{A^*}{\sqrt{2\pi}\Sigma_b}\, exp\left[-\frac{\left(\kappa-\frac{\Sigma_S^2}{(\varepsilon_1^2+\varepsilon_2^2+\Sigma_S^2)}(\Delta E)\right)^2}{2\Sigma_S^2}\right]. \tag{B.10c}$$

In the evaluation of the $OA(\upsilon)$ function the parameters $\Delta\upsilon$ and ΔE are constants; whereas, the parameter κ becomes the variable of integration. Consequently, the function $OA(\upsilon)$ is approximated by

$$OA(\upsilon) \cong \frac{A^*}{\sqrt{2\pi}\Sigma_b}\int_{-\infty}^{\infty} d\kappa\, exp\left[-\frac{\left(\kappa-\frac{\Sigma_b^2}{(\varepsilon_1^2+\varepsilon_2^2+\Sigma_S^2)}(\Delta E)\right)^2}{2\Sigma_S^2}-\frac{\left(\frac{k_{2,max}^2}{k_{max}^2}\kappa+\frac{k_{2,max}^2}{m}(\Delta\upsilon)+\frac{\varepsilon_2^2}{(\varepsilon_1^2+\varepsilon_2^2+\Sigma_S^2)}(\Delta E)\right)^2}{2\varepsilon_2^2}\right]$$

$$exp\left[-\frac{\left(\frac{\left(k_{max}^2-k_{2,max}^2\right)}{k_{max}^2}\kappa-\frac{k_{2,max}^2}{m}(\Delta\upsilon)+\frac{\varepsilon_1^2}{(\varepsilon_1^2+\varepsilon_2^2+\Sigma_S^2)}(\Delta E)\right)^2}{2\varepsilon_1^2}\right]. \tag{B.11}$$

This integration of the Gaussian is performed by (1) combining the three quadratic terms in the exponential, (2) completing the square of the κ terms, and, finally, (3) performing the integral over the displaced Gaussian. After considerable algebra, one finds

$$OA(\upsilon) \cong A^*\frac{\varepsilon_1\varepsilon_2}{\sqrt{\varepsilon_1^2\varepsilon_2^2+\Sigma_S^2[\varepsilon_1^2\Psi^2+\varepsilon_2^2(1-\Psi)^2]}}\,exp\left[-\frac{(\Delta\upsilon)^2}{2\Sigma_3^2}\right] exp\left[-\frac{(\Delta E)^2}{2\Sigma_4^2}\right] \tag{B.12}$$

where

$$\Psi \equiv \frac{k_{2,max}^2}{k_{max}^2} = \left[\frac{\left(\varepsilon_1^2+\Sigma_S^2\right)E_2+\varepsilon_2^2(E_S-E_1)}{\left(\varepsilon_1^2+\varepsilon_2^2\right)E_S+\Sigma_S^2(E_1+E_2)}\right]^2 \tag{B.13}$$

$$\Sigma_3 \equiv \frac{m}{k_{2,max}^2}\frac{\sqrt{\varepsilon_1^2\varepsilon_2^2+\Sigma_S^2[\varepsilon_1^2\Psi^2+\varepsilon_2^2(1-\Psi)^2]}}{\sqrt{\varepsilon_1^2+\varepsilon_2^2+\Sigma_S^2}} = \frac{m\sqrt{\varepsilon_1^2\varepsilon_2^2+\Sigma_S^2[\varepsilon_1^2\Psi^2+\varepsilon_2^2(1-\Psi)^2]}[\varepsilon_1^2+\varepsilon_2^2+\Sigma_S^2]^{3/2}}{[(\varepsilon_1^2+\Sigma_S^2)E_2+\varepsilon_2^2(E_S-E_1)]^2} \tag{B.14}$$

and $$\Sigma_4 \equiv (\varepsilon_1^2+\varepsilon_2^2+\Sigma_s^2)\frac{\sqrt{\varepsilon_1^2\varepsilon_2^2+\Sigma_s^2[\varepsilon_1^2\Psi^2+\varepsilon_2^2(1-\Psi)^2]}}{\sqrt{\varepsilon_1^2\varepsilon_2^2(\varepsilon_1^2+\varepsilon_2^2+2\Sigma_s^2)+\Sigma_s^2[\varepsilon_1^2\Psi+\varepsilon_2^2(1-\Psi)]^2+\Sigma_s^4[\varepsilon_1^2\Psi^2+\varepsilon_2^2(1-\Psi)^2]}}. \tag{B.15}$$

This complicated form of the function OA arises from the arbitrary Gaussian source spectrum asserted in Equation (B.2). However, one frequently requires narrow energy spectra, e.g., emission lines or narrow energy bins ($\leq 2\ keV$). Assuming such a narrow emission line significantly simplifies the OA function. If $\Sigma_s^2 \ll (\varepsilon_1^2+\varepsilon_2^2)$, then one finds

$$OA(\upsilon) \cong A^* exp\left[-\frac{(\upsilon-\upsilon_{max})^2}{2\Sigma_3^2}\right] exp\left[-\frac{(E_s-E_1-E_2)^2}{2(\varepsilon_1^2+\varepsilon_2^2)}\right] \tag{B.16}$$

where

$$\upsilon_{max} = 1-\frac{m[\varepsilon_2^2E_1+\varepsilon_1^2(E_s-E_2)]}{E_s[\varepsilon_1^2E_2+\varepsilon_2^2(E_s-E_1)]} = \mu\left(\frac{\varepsilon_2^2E_1+\varepsilon_1^2(E_s-E_2)}{(\varepsilon_1^2+\varepsilon_2^2)}, \frac{\varepsilon_1^2E_2+\varepsilon_2^2(E_s-E_1)}{(\varepsilon_1^2+\varepsilon_2^2)}\right) \cong \mu(E_1,E_2) \tag{B.17}$$

and $$\Sigma_3 = \frac{m\varepsilon_1\varepsilon_2[\varepsilon_1^2+\varepsilon_2^2]^{3/2}}{[\varepsilon_1^2E_2+\varepsilon_2^2(E_s-E_1)]^2} \approx \frac{\varepsilon_1\varepsilon_2}{\sqrt{\varepsilon_1^2+\varepsilon_2^2}}\frac{m}{E_2^2}. \tag{B.18}$$

Equations (B16) through (B.18) constitute the form of OA used in the remainder of this report. The cosine of the opening angle of the Compton cone is characterized by υ_{max} in Equation (B.17); this parameter is equivalent to $\mu(E_1,E_2)$ of Equation (12) if the source energy E_s satisfies $E_s = E_1 + E_2$. However, if the source energy differs from $E_s = E_1 + E_2$, the opening angle of the Compton cone shifts to accommodate the presumed incident source energy, E_s. Fortunately, if $E_s \neq E_1 + E_2$ by any significant amount, the finally Gaussian in Equation (B.16) suppresses the function OA; thereby, making the value of υ_{max} irrelevant.

General Observations about Effect of Energy Resolution on the Broadening of the Compton Cone

Throughout most of this paper, the analysis is based on the physics of Compton scattering, the definitions of physical parameters (e.g., attenuation coefficients, cross-sections, etc.) and elementary analytical models (i.e., Gaussian responses). In particular, detector resolutions (both spatial and energy) remain independent parameters that can be chosen based on the detection device. In this subsection of Appendix B, we (temporarily) abandon that generality to make important observations about the effects of energy resolution on the broadening of the Compton cone. The energy resolution is generally dependent on the energy deposition. The details can vary significantly depending on the electronics, materials, design, and even detector history; however, an empirical formula for the energy resolution that is applicable to a generic detector can be written as

$$\varepsilon(E) = \sqrt{\varepsilon_0^2+\eta^2mE} \approx max\left(\varepsilon_0, \eta\sqrt{mE}\right) \tag{B.19}$$

where the parameters ε_0 and η characterize the detector resolution over a wide range of energies. The functional form in Equation (B.19) reflects the expected $\sqrt{E}$ behavior of energy resolution for most charge-collection detectors. The dimensionless parameter η

describes the resolution at E=m=511keV; i.e., η=ε(m)/m with typical values about 0.03-0.12 (i.e., 3-12% error at 511keV). The ε_0 parameter is a minimal resolution that becomes important only for very low energies; a typical value is ε_0=5 keV and becomes relevant only for E<20 keV. [N.B. The effects of Doppler broadening on the energy deposition of the Compton scattering interaction can be incorporated into the parameter, ε_1, by adjustment of the ε_0 parameter; $\varepsilon_0^2 \to \varepsilon_0^2 + \varepsilon_{Doppler}^2$, so that $\left(\varepsilon_1 = \sqrt{\varepsilon_0^2 + \varepsilon_{Doppler}^2 + \eta^2 m E_1}\right)$.]

The parameter Σ_3 defined in Equation (B.18) indicates the uncertainty in the cosine of the scattering angle $[\mu = cos\theta]$ caused by the energy resolution. For measurements E_1 and E_2, one can define $E=E_1+E_2$ and use μ as defined in Equation (12) to convert $(E_1, E_2) \longrightarrow (E, \mu)$, so that

$$\Sigma_3 = \frac{\varepsilon_1 \varepsilon_2}{m\sqrt{\varepsilon_1^2+\varepsilon_2^2}} \frac{[m+E(1-\mu)]^2}{E^2} \tag{B.20}$$

If one evaluates ε_1 and ε_2 with the empirical formula (B.19), the uncertainty parameter Σ_3 becomes

$$\Sigma_3 \cong \eta \frac{[m+E(1-\mu)]}{E} \sqrt{1-\mu} \ . \tag{B.21}$$

This uncertainty in the cosine can then be converted into an uncertainty in the opening angle of the Compton cone:

$$\Delta\theta = \Delta\mu \Big/ \left|\frac{d\mu}{d\theta}\right| = \frac{\Sigma_3}{\sqrt{1-\mu^2}} \cong \eta \frac{[m+E(1-\mu)]}{E\sqrt{1+\mu}} \ . \tag{B.22}$$

The parameter Σ_3 plays a crucial role in the remainder of this paper; however, the opening angle of the Compton cone (Δθ) provides better intuitive understanding of the effects of Σ_3. In particular, backscattered radiation ($\mu \approx -1$) suffers from extremely poor angular resolution; whereas, the forward scattered radiation ($\mu \approx 1$) exhibits comparatively good angular resolution. This important observation arises from the small errors in ε_1 $\left(\varepsilon_1 \propto \sqrt{E_1} \propto \sqrt{1-\mu}\right)$ that arise in forward scattering ($E_1 \longrightarrow 0$). On the other hand, for backscattering the $\varepsilon_2\left(\propto \sqrt{E_2}\right)$ term does not vanish and, therefore does not cancel the $1/\sqrt{1-\mu^2}$ term that arises from the coordinate transformation in Equation (B.22). Another important observation is that once the total energy, E, drops smaller the m (E<m), the angular resolution degrades significantly – even for small angle scattering. This fact is the basis of the well-known observation that Compton cameras work best for high energy radiation sources. Both these effects are illustrated in Figures B.1 and B.2. The figures demonstrated the expected angular resolution from the broadening of the Compton cone for detectors exhibiting 3% energy resolution at 511 keV. The loss in angular resolution for backscattered radiation is dramatic. For events scattering at greater than 160 degrees, the angular uncertainty is greater than 30 degrees! One possible conclusion is that the events associated with scatter angles greater than 140 degrees should be discarded. Fortunately, the Klein-Nishina scattering cross-section naturally suppresses backscatter events for high energy radiation, so that such a cut-off actually excludes few events.

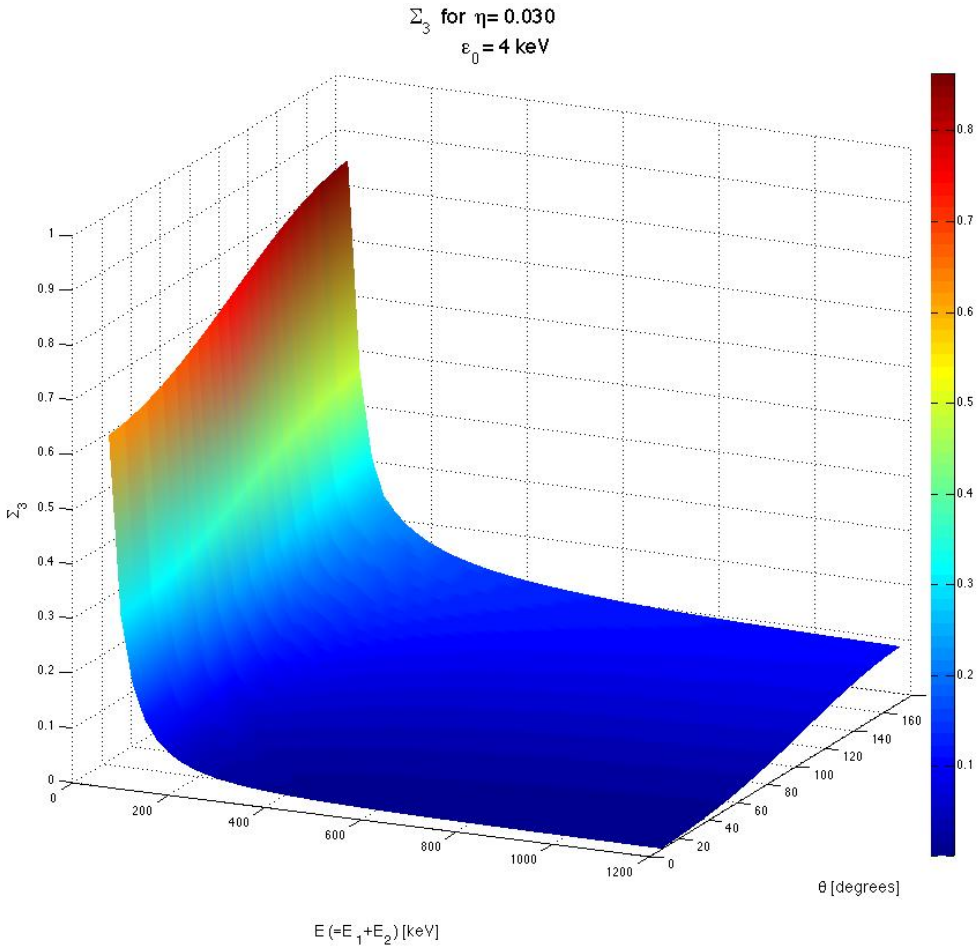

Figure B.1. The function Σ_3 is shown for the energy resolution parameters η=0.03 and ε_0=4 keV. The values of E_1 and E_2 are calculated from the total energy (E) and the scattering angle θ [$\mu = cos(\theta)$]. The energy resolutions, ε_1 and ε_2, are calculated from E_1 and E_2 based on Equation (B.19). The function Σ_3 is then calculated from Equation (B.18). This plot demonstrates two important properties of Σ_3. First, for fixed E, Σ_3 is a slowly, monotonically increasing function of θ with minimum at θ=0 (forward scattering) and maximum at θ=180^o (backscattering). Second, as a function of E, Σ_3 is a monotonically decreasing function that is very large for small E(<200 keV), but decreases and plateaus for E>m.

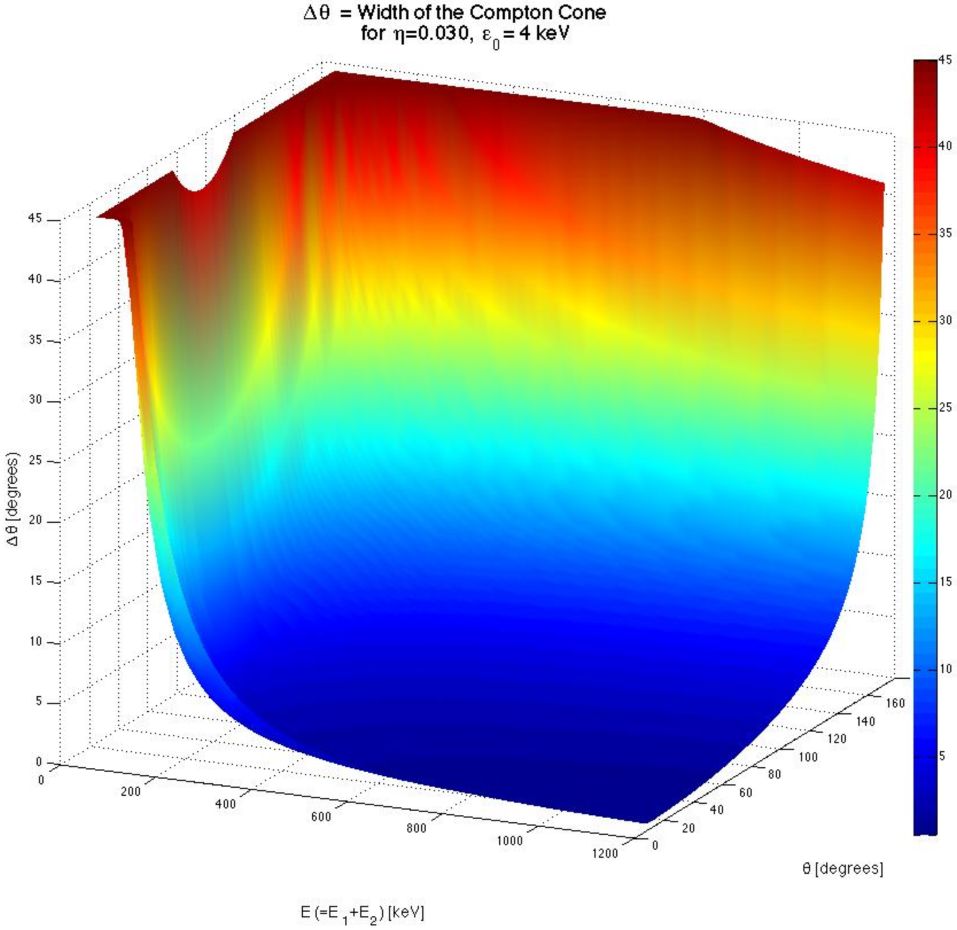

Figure B.2a. The width of the Compton cone Δθ is shown as determined from Σ_3 (see Figure B.1) by application of Equation (B.19). The figure demonstrates that the angular resolution degenerates dramatically at low energies (E<200 keV) and at large scattering angles (θ>150°). Thus, one should not expect the backscattered events to contribute significantly to the imaging process.

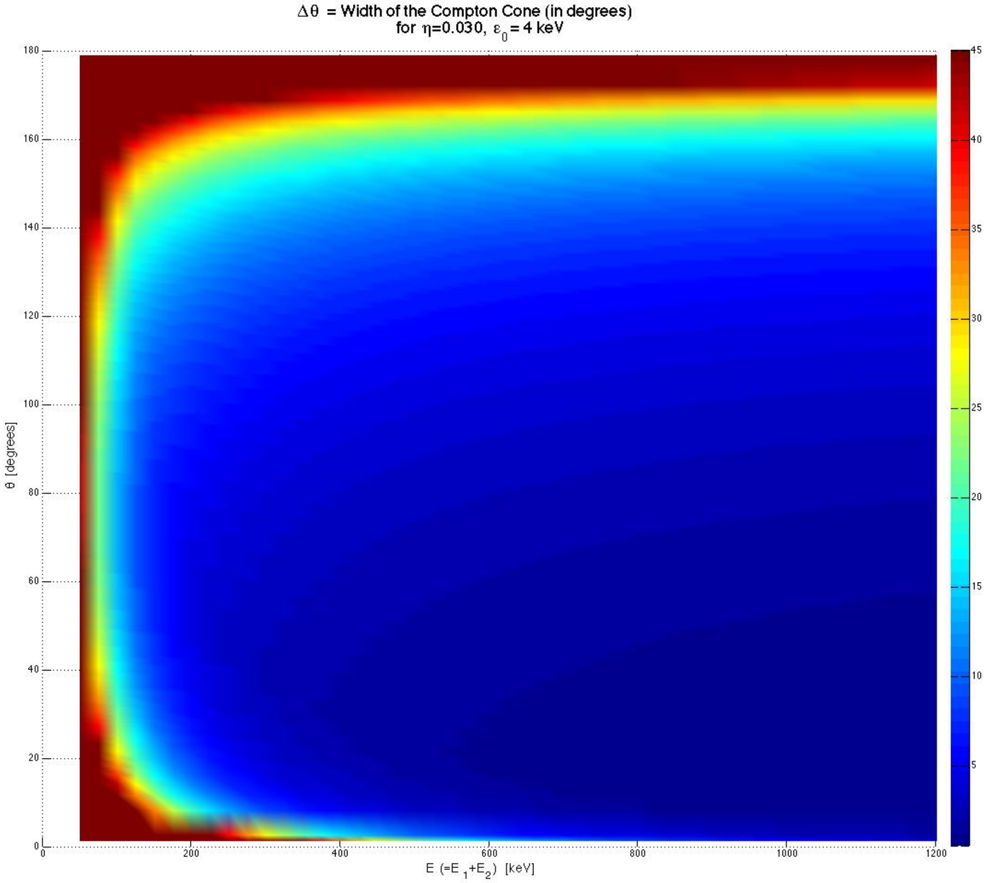

Figure B.2b. The width of the Compton cone Δθ (in degrees) is shown as determined from Σ_3. The color bar on the right indicates the angular uncertainty (Δθ, in degrees) associated with measurements having total energy E(=E1+E2) and scattering at angle θ. The figure displays the same information as Figure B2a from a perspective that more clearly delineates the regions of poor angular resolution.

The Function OA Fails to Suppress Unphysical Interaction Sequences

The kinematics of Compton scattering is at the core of the entire response calculation and the function OA characterizes this kinematics. The energies E_1 and E_2 determine the angle of scattering according to Equation (12). The most probably cosine of the scattering angle is represented as υ_{max} in Equation (B.17); and, the uncertainty in this cosine is characterized by Σ_3 in Equation (B.18). However, according to the Inequalities (13) some combinations of E_1 and E_2 are unphysical because they predict $\upsilon_{max} \cong \mu(E_1, E_2) < -1$. One expects the rates for these unphysical combinations to be suppressed in the OA function where the kinematic prediction [υ_{max} in Equation (B.17)] is compared with the actual physical cosine, υ. Indeed, the function OA *is* suppressed for such combinations, but the suppression *is not* a sharp cutoff at $\mu(E_1, E_2) = -1$. If $\upsilon_{max} = -1 - \delta$ (and is, therefore, unphysical), the maximum of OA(υ) occurs for υ=-1; so that, according to Equation (B.25)

$$OA(-1) = A^* exp\left[-\frac{\delta^2}{2\,\Sigma_3^2}\right] \tag{B.24}$$

is the maximum value of OA for an unphysical combination of E_1 and E_2. Thus, the condition OA(unphysical)<.02*OA(physical) implies $\delta<3\Sigma_3$. The function OA will successfully suppress unphysical combinations if $\mu(E_1, E_2) = -1 - 3\Sigma_3$. However, for $\mu(E_1, E_2)$ in the interval

$$-1 \leq \mu(E_1, E_2) \leq -1 - 3\Sigma_3 \tag{B.25}$$

(*a priori* unphysical) there is only partial suppression of the function OA. This interval of partial suppression is associated with the uncertainty in the μ caused by the uncertainty in measured energies.

The region of partial suppression described by the Inequalities (B.25) can be estimated based on the assumption $\mu(E_1, E_2) \approx -1$. In the vicinity of $\mu(E_1, E_2) \approx -1$, one finds that ($E=E_1+E_2$)

$$E_1 \approx \frac{2E^2}{(m+2E)} \quad ; \quad E_2 \approx \frac{mE}{(m+2E)} \tag{B.26}$$

so that, according to Equation (B.19) the errors associated with these energies are

$$\varepsilon_1 \approx \eta E\sqrt{\frac{2m}{(m+2E)}} \quad ; \quad \varepsilon_2 \approx \eta m\sqrt{\frac{E}{(m+2E)}} \ . \tag{B.27}$$

The resulting parameter $\Sigma_3(\mu \approx -1)$ is given by

$$\Sigma_3(\mu \approx -1) = \sqrt{2}\,\eta\,\frac{(m+2E)}{E} \ . \tag{B.28}$$

From Equation (B,28) one observes that a lower limit for $\Sigma_3(\mu \approx -1)$ is given by

$$\sqrt{8}\eta < \Sigma_3(\mu \approx -1)\,. \tag{B.29}$$

For typical values $\eta=.03$ and $E=m$, one finds $\Sigma_3=0.12$. This approximate result indicates a serious problem. If $\Sigma_3=0.12$ the OA function does not fully suppress unphysical sequences until $\mu < -1.36$. Unphysical sequences in the interval $[-1.36 < \mu < -1]$ will be only partially suppressed. This discouraging result is a simple corollary of the angular resolution problem illustrated in Figures B1 and B2. Basically, the angular resolution for backscattered radiation is so poor that the detectors are incapable of distinguishing whether an interaction sequence has crossed the backscatter threshold [i.e., Inequality (13)] or not. This conclusion, combined with the overall angular resolution problem near the backscatter limit, suggests that the general form of OA given in Equation (B.16) should be modified by imposing an angular cutoff of the form

$$OA^*(\upsilon) = OA(\upsilon)\Theta\big(\upsilon_{max} - \mu_{cutoff}\big) \tag{B.30}$$

where a typical value of $\mu_{cutoff} = -0.85$ might be considered (i.e., rejection of all events with scattering angle $\theta > 150°$). Because such a cutoff depends on only the detected energies and associated resolutions (not υ), it does not affect the rate calculation and can be imposed at any point in the analysis. Nonetheless, the obvious cutoff $\mu_{cutoff} = -1$ should be implemented to suppress the most egregious combinations, i.e.,

$$OA^*(\upsilon) = OA(\upsilon)\Theta(1 + \upsilon_{max})$$

or

$$OA^*(\upsilon) = OA(\upsilon)\Theta\left(2 - \frac{m}{E_s}\frac{\left[\varepsilon_1^2 E_2 + \varepsilon_2^2(E_s - E_1)\right]}{\left[\varepsilon_2^2 E_1 + \varepsilon_1^2(E_s - E_2)\right]}\right). \tag{B.31}$$

Appendix C. Evaluation the Compton Cone (CC) function – the Crucial Double Spherical Integral

This appendix evaluates the integrals over the possible directions of both the incident and scattered radiation that appear in Equation (57). For purposes of this calculation, the integrals are written in a very general form:

$$CC\left(\vec{\alpha}\cdot\vec{\beta},\mu;\Sigma_i\right) \equiv \frac{1}{(2\pi\Sigma_1^2)(2\pi\Sigma_2^2)} \iint_{S^2} d^2\vec{\Omega}_1 \iint_{S^2} d^2\vec{\Omega}_2 \;\; \Theta\left(\vec{\Omega}_1\cdot\vec{\beta}\right)\Theta\left(\vec{\Omega}_2\cdot\vec{\alpha}\right)$$
$$exp\left\{-\frac{1}{2\Sigma_1^2}\left[1-\left(\vec{\Omega}_1\cdot\vec{\beta}\right)^2\right]-\frac{1}{2\Sigma_2^2}\left[1-\left(\vec{\Omega}_2\cdot\vec{\alpha}\right)^2\right]\right\} \qquad (C.1)$$
$$exp\left\{-\frac{1}{2\Sigma_3^2}\left[\left(\vec{\Omega}_1\cdot\vec{\Omega}_2\right)-\mu\right]^2\right\}.$$

The exponentials in the integrand are similar to Gaussians locally; but, due to the global integration over spheres, do not exhibit the same asymptotic properties that simplify integrations over Gaussians on R^n. Nonetheless, because the constants, Σ_i, are small (Σ_i<<1), the integrals are dominated by the local behavior; so that, the integrands can be treated locally as Gaussians.

The evaluation of the CC function requires the 4D integration of over the half spheres in Equation (C.1). One accomplishes this integration by mapping the two half-spheres $\left(\vec{\Omega}_1,\vec{\Omega}_2\right)$ onto two R^2 planes $(\vec{r},\vec{s})$ by the transformations:

$$\vec{\Omega}_1 = \left[\sqrt{1-r^2}\vec{\beta} + r_1\frac{\left(\vec{\alpha}-\nu\vec{\beta}\right)}{\sqrt{1-\nu^2}} + r_2\frac{\vec{\alpha}\times\vec{\beta}}{\left|\vec{\alpha}\times\vec{\beta}\right|}\right]$$

$$\vec{\Omega}_2 = \left[\sqrt{1-s^2}\vec{\alpha} + s_1\frac{\left(\vec{\Omega}_1-\kappa\vec{\alpha}\right)}{\sqrt{1-\kappa^2}} + s_2\frac{\vec{\alpha}\times\vec{\Omega}_1}{\left|\vec{\alpha}\times\vec{\Omega}_1\right|}\right] \qquad (C.2)$$

where

$$\nu \equiv \vec{\alpha}\cdot\vec{\beta}\,,$$

$$\kappa(\vec{r}) \equiv \vec{\Omega}_1\cdot\vec{\alpha} = \sqrt{1-r^2}\nu + r_1\sqrt{1-\nu^2}\,,$$

$$r^2 \equiv r_1^2 + r_2^2 < 1\,, \qquad (C.3)$$

$$s^2 \equiv s_1^2 + s_2^2 < 1\,.$$

We note that

$$-1 < \kappa(\vec{r}) < 1 \qquad \text{and} \qquad \kappa(\vec{r}=0) = \nu. \qquad (C.4)$$

These transformations are basically a projection of the half spheres into unit circles in the planes R^2. [The case $\nu^2=1$ must be formally excluded because collinear vectors α and β

produce a pathology in the mapping; however, the problem can be computationally resolved by adding an arbitrary infinitesimal rotation to either of the vectors.] From the transformations in Equation (C.2) one finds that the range of integration over a half-sphere is mapped into the unit circle in the R^2 plane: so that,

$$\iint_{\substack{S^2 \\ \vec{\Omega}_1\cdot\vec{\beta}>0}} d^2\,\vec{\Omega}_1 \;\iint_{\substack{S^2 \\ \vec{\Omega}_2\cdot\vec{\alpha}>0}} d^2\,\vec{\Omega}_2 \;=\; \iint_{\substack{R^2 \\ |\vec{r}|<1}} d^2\vec{r}\;(1-r^2)^{-1/2} \iint_{\substack{R^2 \\ |\vec{s}|<1}} d^2\vec{s}\;\;(1-s^2)^{-1/2} \tag{C.5}$$

where the weightings in Equation (C.5) arise from the Jacobian associated with the coordinate transformations. Other terms in the integrand of Equation (C.1) depend on inner products. In particular, one finds that

$$\left(\vec{\Omega}_1\cdot\vec{\beta}\right)=\sqrt{1-r^2} \qquad\qquad \left(\vec{\Omega}_2\cdot\vec{\alpha}\right)=\sqrt{1-s^2} \tag{C.6}$$

$$\left(\vec{\Omega}_1\cdot\vec{\Omega}_2\right)=\kappa\sqrt{1-s^2}+\sqrt{1-\kappa^2}s_1 \tag{C7}$$

so that

$$1-\left(\vec{\Omega}_1\cdot\vec{\beta}\right)^2=r^2 \qquad\qquad 1-\left(\vec{\Omega}_2\cdot\vec{\alpha}\right)^2=s^2. \tag{C.8}$$

Thus, Equation (C.1) becomes

$$CC\left(\vec{\alpha}\cdot\vec{\beta},\mu;\Sigma_i\right)=\frac{1}{(2\pi\Sigma_1^2)(2\pi\Sigma_2^2)}\iint_{|\vec{r}|<1} d^2\,\vec{r}\,(1-r^2)^{-1/2}\iint_{|\vec{s}|<1} d^2\,\vec{s}\,(1-s^2)^{-1/2}$$
$$exp\left\{-\frac{r^2}{2\Sigma_1^2}-\frac{s^2}{2\Sigma_2^2}\right\}\,exp\left\{-\frac{1}{2\Sigma_3^2}\left[\left(\vec{\Omega}_1\cdot\vec{\Omega}_2\right)-\mu\right]^2\right\}\,. \tag{C.9}$$

For convenience, we denote the three crucial Gaussian functions as

$$M_1(\vec{r})\equiv exp\left[-\frac{|\vec{r}|^2}{2\Sigma_1^2}\right],$$
$$M_2(\vec{s})\equiv exp\left[-\frac{|\vec{s}|^2}{2\Sigma_2^2}\right]\text{ , and} \tag{C.10}$$
$$M_3(\vec{r},\vec{s})\equiv exp\left\{-\frac{1}{2\Sigma_3^2}\left[\left(\vec{\Omega}_1\cdot\vec{\Omega}_2\right)-\mu\right]^2\right\}$$

The M_1 function suppresses contributions to the integral from larger values of $|\vec{r}|$; and the M_2 function suppresses contributions to the integral from larger values of $|\vec{s}|$. Our earlier analysis of realistic events indicated that $\left(1/2\Sigma_{1,2}^2\right)>6$; so that the Gaussian peaks in the vicinity of $\vec{r}\approx 0$ and $\vec{s}\approx 0$ are relatively narrow. In particular, the contributions to the integrals for values of $|\vec{r}|^2>1/2$ or $|\vec{s}|^2>1/2$ are generally insignificant. The difficulties with these integrals arise from the complicated nature of the M_3 function. This suggests a simple approximation

$$M_3(\vec{r},\vec{s})\approx M_3\left(\vec{0},\vec{0}\right)=exp\left[-\frac{1}{2\Sigma_3^2}(\nu-\mu)^2\right]. \tag{C.11}$$

If one adopts this approximation, the integrals over $\vec{r}$ and $\vec{s}$ decouple and become standard special functions; so that

$$CC(\nu,\mu;\Sigma_i) \approx \frac{1}{\Sigma_1^2\Sigma_2^2} exp\left[-\frac{1}{2\Sigma_3^2}(\nu-\mu)^2\right] exp\left[-\frac{1}{2\Sigma_1^2}-\frac{1}{2\Sigma_2^2}\right]$$
$${}_1F_1\left(\frac{1}{2},\frac{3}{2};\frac{1}{2\Sigma_1^2}\right)\, {}_1F_1\left(\frac{1}{2},\frac{3}{2};\frac{1}{2\Sigma_2^2}\right) \qquad \text{(C.12)}$$

Using the asymptotic behavior of the $_1F_1$ for large argument; namely,

$${}_1F_1(\alpha,\gamma;x) \xrightarrow[x\gg 1]{} \frac{\Gamma(\gamma)}{\Gamma(\alpha)}\, x^{\alpha-\gamma} exp(x) \qquad \text{(C.13)}$$

one concludes that

$$CC(\nu,\mu;\Sigma_i) \xrightarrow[\substack{\Sigma_1\ll 1\\ \Sigma_2\ll 1}]{} exp\left[-\frac{1}{2\Sigma_3^2}(\nu-\mu)^2\right] \qquad \text{(C.14)}$$

approximates the CC function. We note that the important imaging properties associated with the Compton cone are expressed in the Gaussian term of Equation (C.14). For many years this approximation was used in our analysis. The problem with this simple expression is that virtually all the blurring effects of Σ_1 and Σ_2 (which may be comparable to Σ_3) are ignored.

A better approximation of CC can be found by assuming that

$$M_3(\vec{r},\vec{s}) \approx M_3(\vec{0},\vec{s}) = exp\left[-\frac{1}{2\Sigma_3^2}\left(\nu\sqrt{1-s^2}+\sqrt{1-\nu^2}s_1-\mu\right)^2\right]. \qquad \text{(C.15)}$$

This approximation ignores the blurring effects due to Σ_1, but includes the blurring due to Σ_2. Essentially, this assumption is exact in the $\Sigma_1 \rightarrow 0$ limit. In this approximation, the integral over $\vec{r}$ decouples and can be evaluated independently, so that

$$CC(\nu,\mu;\Sigma_i) = \frac{1}{\Sigma_1^2} exp\left[-\frac{1}{2\Sigma_1^2}\right] {}_1F_1\left(\frac{1}{2},\frac{3}{2};\frac{1}{2\Sigma_1^2}\right)$$
$$\frac{1}{(2\pi\Sigma_2^2)}\iint_{|\vec{s}|<1} d^2\,\vec{s}\,(1-s^2)^{-1/2}\, M_2(\vec{s})\, M_3(\vec{0},\vec{s}) \;. \qquad \text{(C.16)}$$

Once again, the asymptotic limit of the $_1F_1$ function for $\Sigma_1 \rightarrow 0$ allows one to write

$$CC(\nu,\mu;\Sigma_i) \xrightarrow[\Sigma_1\ll 1]{} \frac{1}{(2\pi\Sigma_2^2)}\iint_{|\vec{s}|<1} d^2\,\vec{s}\,(1-s^2)^{-1/2}\, M_2(\vec{s})\, M_3(\vec{0},\vec{s})\,. \qquad \text{(C.17)}$$

Despite these simplifications, this integral is still daunting due the complicated nature of M_3 term. However, these complications can now be easily visualized by displaying the M_2 and M_3 functions on the $\vec{s}$ plane. Figure C.1 displays the functions M_2 and M_3 on the (s_1,s_2) plane for Σ_2=.05, Σ_3=.07, ν=0.8 and various values of μ. A major conclusion can be inferred from the Figure C.1; namely, that the values of M_3 off the s_2 axis have little effect on the product M_2*M_3 because only the point of closest approach of the Compton cone with the origin (s_2=0) contributes to the product. Thus, one can approximate $M_3(\vec{0},\vec{s}) \cong M_3(\vec{0},s_1\vec{e}_1)$. The effects of this approximation are displayed in Figure C.2 which compares the product M_2*M_3 with/without the approximation. The errors are less than 1 percent.

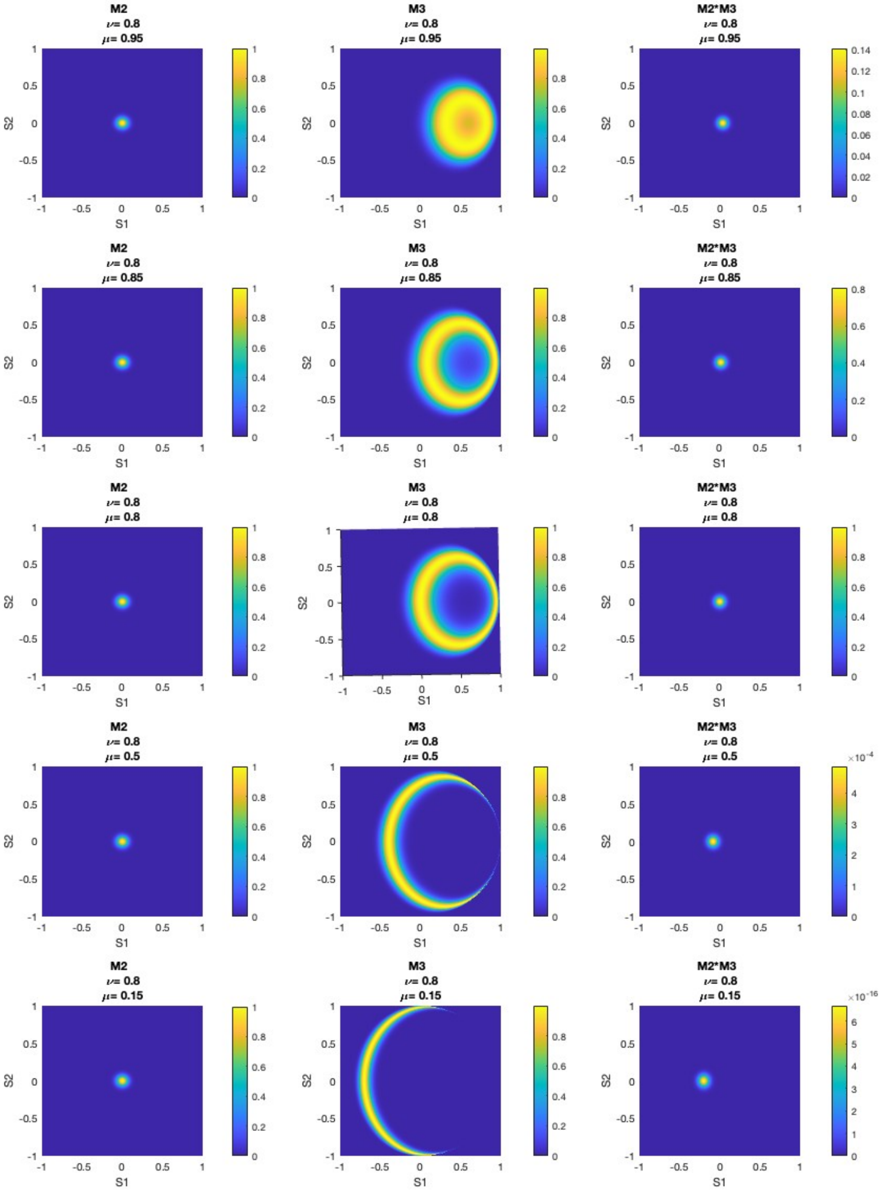

Figure C.1. The functions M_2 and M_3 are displayed for Σ_2=0.05, Σ_3=0.07, and ν=0.8. Each row displays the M_2, M_3, and M_2*M_3 functions for different values a specific value of μ (=0.95, 0.85, 0.8, 0.5 and 0.15 in successive rows). In the first column, the M_2 function represents the dispersion of the cone axis due to uncertainty in the interaction positions, does not depend on μ, and is the same in each row. In the second column, the M_3 function displays the arc of the Compton cone intersecting the $\vec{s}$ plane and varies significantly depending on the opening angle of the cone (μ). The third column shows the product of M_2*M_3 which appears as another Gaussian-like function centered on a position on the s_2=0 axis and displaced from the origin toward the point of closest approach on the arc of the Compton cone.

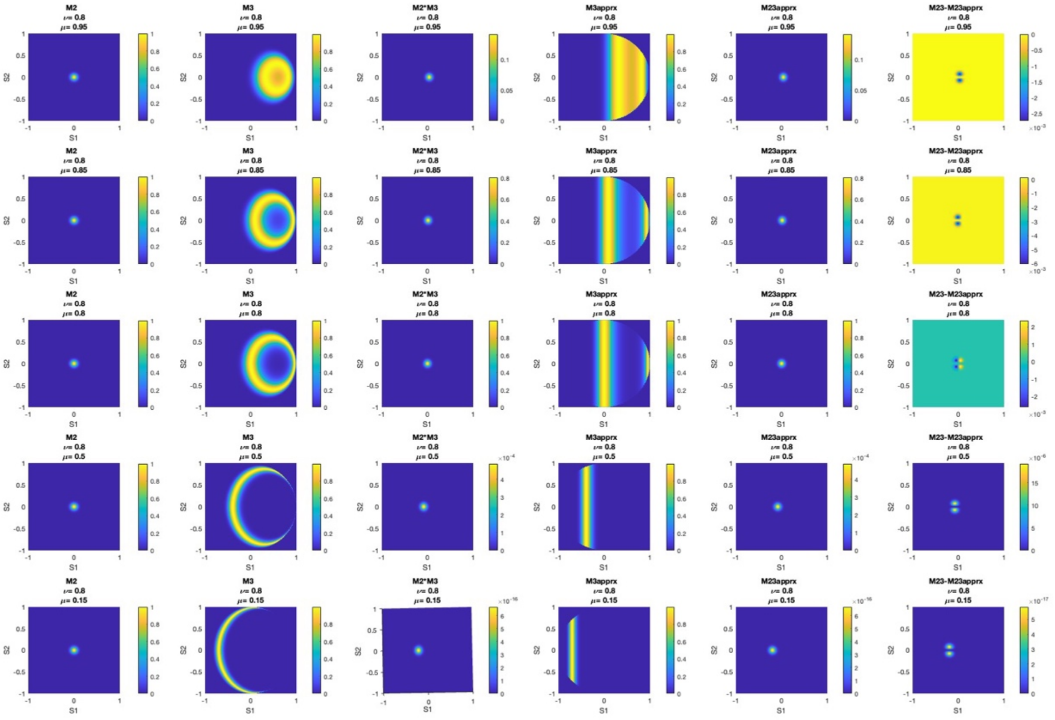

Figure C.2. The functions M_2, M_3 and their approximations are displayed for Σ_2=0.05, Σ_3=0.07, and ν=0.8. Each row corresponds to a specific μ (=0.95, 0.85, 0.8, 0.5, and 0.15). Each column corresponds to a specific function. The first column displays M_2 which represents the dispersion of the cone axis due to uncertainty in the interaction positions. The second column displays M_3 which exhibits the intersection of the Compton cone with the $\vec{s}$ plane. The third column displays the product M_2*M_3 that appears in the integrand. The fourth column shows the proposed approximation for M_3; namely, $M_3(\vec{r} = 0, \vec{s} = s_1\vec{e}_1)$ that assumes s_2=0. This approximation has the same profile as M_3 along the s_2=0 axis, but displays no s_2 dependence and, therefore, the arc structure of the Compton cone is lost. Nonetheless, the product of M_2 and the M_3 approximation, shown in the fifth column, is virtually identical to the exact product in the third column. The difference M_2*M_3 and its approximation is displayed in the sixth column. The differences are less than a few percent of the actual product.

Based on these considerations, we adjust the approximation again and settle on the approximation (used for the remainder of this paper):

$$CC(\nu,\mu;\Sigma_i) \cong \frac{1}{(2\pi\Sigma_1^2)(2\pi\Sigma_2^2)} \iint_{[\vec{r}]<1} d^2\,\vec{r}\,(1-r^2)^{-1/2} M_1(\vec{r}) \tag{C.18}$$

$$\iint_{[\vec{s}]<1} d^2\,\vec{s}\,(1-s^2)^{-1/2} M_2(\vec{s})\, M_3(r_1\vec{e}_1, s_1\vec{e}_1)\,.$$

With this approximation the integrals over r_2 and s_2 can be performed explicitly; so that

$$CC(\nu,\mu;\Sigma_i) \cong \frac{1}{(2\Sigma_1^2)(2\Sigma_2^2)} \int_{-1}^{1} dr_1\, exp\left[-\frac{(1-r_1^2)}{2\Sigma_1^2}\right] {}_1F_1\left(\frac{1}{2},1;\frac{(1-r_1^2)}{2\Sigma_1^2}\right) M_1(r_1\vec{e}_1) \tag{C.19}$$

$$\int_{-1}^{1} ds_1\, exp\left[-\frac{(1-s_1^2)}{2\Sigma_2^2}\right] {}_1F_1\left(\frac{1}{2},1;\frac{(1-s_1^2)}{2\Sigma_2^2}\right) M_2(s_1\vec{e}_1)\, M_3(r_1\vec{e}_1, s_1\vec{e}_1)\,.$$

Once again, arguments of the confluent hypergeometric functions are expected to be large so that the asymptotic behavior of ${}_1F_1$ [Equation (C.13)] can be invoked with the result,

$$CC(\nu,\mu;\Sigma_i) \cong \frac{1}{2\pi\Sigma_1\Sigma_2} \int_{-1}^{1} dr_1\,(1-r_1^2)^{-1/2}\, M_1(r_1\vec{e}_1) \tag{C.20}$$

$$\int_{-1}^{1} ds_1\;(1-s_1^2)^{-1/2}\, M_2(s_1\vec{e}_1)\, M_3(r_1\vec{e}_1, s_1\vec{e}_1)\,.$$

Equation (C.20) provides an excellent approximation of the CC function and will be used in all subsequent analysis. The M_3 term is most problematic in the evaluation of the integrals and, therefore, warrants careful examination. One observes that

$$M_3(r_1\vec{e}_1, s_1\vec{e}_1) = exp\left[-\frac{1}{2\Sigma_3^2}\left(\kappa\sqrt{1-s_1^2}+\sqrt{1-\kappa^2}\,s_1-\mu\right)^2\right] \tag{C.21}$$

can be simplified by the notation

$$\Xi(x,y) \equiv x\sqrt{1-y^2}+y\sqrt{1-x^2} = \Xi(y,x) \tag{C.22}$$

so that by Equations (C.3) and (C.21) can be written as

$$\kappa = \Xi(r_1,\nu) \tag{C.23}$$

and $M_3(r_1\vec{e}_1, s_1\vec{e}_1) = exp\left[-\frac{1}{2\Sigma_3^2}\,(\Xi(s_1,\kappa)-\mu)^2\right]$, respectively.

As a result, M_3 is maximum (s_1=s_{max}) when

$$\Xi(s_{max},\kappa) = \kappa\sqrt{1-s_{max}^2}+\sqrt{1-\kappa^2}\,s_{max} = \mu. \tag{C.24}$$

Simple algebra reveals the general result that

$$\Xi(x,y) = z \quad \Rightarrow \quad x = \Xi(z,\pm y). \tag{C.25}$$

This identity will be invoked repeatedly. The ± sign in Equation (C.25) provides two solutions of the quadratic equation – corresponding in Equation (C.24) to the directions on the Compton cone that are nearest and furthest from the direction to the voxel. The contribution to the integrand will be greatest for the direction of closest approach. As a result, we find that

$$s_{max} = \sigma\sqrt{1-\left[max\big(0,\Upsilon(\mu,\kappa)\big)\right]^2} \cong\; \Xi(\mu,-\kappa) \tag{C.26a}$$

$$\sqrt{1-s_{max}^2} = \ max\big(0, \Upsilon(\mu,\kappa)\big) \tag{C.26b}$$

where

$$\Upsilon(x,y) \equiv xy + \sqrt{1-x^2}\sqrt{1-y^2} \tag{C.27}$$

and $\sigma = sign\big(\Xi(\mu,-\nu)\big);$ (C.28)

Expanding the $\Xi(s_1,\kappa)$ function in a Taylor's series around the peak in M$_3$, one finds

$$\Xi(s_1,\kappa) \cong \Xi(s_{max},\kappa) + \left[\frac{\partial\Xi(s_1,\kappa)}{\partial s_1}\right]_{s_1=s_{max}} (s_1 - s_{max}) + higher\ order\ terms$$

$$\cong \mu + \gamma_2(s_1 - s_{max}) \tag{C.29}$$

where

$$\gamma_2 \equiv \left[\frac{\partial\Xi(s_1,\kappa)}{\partial s_1}\right]_{s_1=s_{max}} = \frac{\sqrt{1-\mu^2}}{\sqrt{1-s_{max}^2}} = \frac{\sqrt{1-\mu^2}}{max\big(0,\Upsilon(\mu,\kappa)\big)} \tag{C.30}$$

so that one can approximate M$_3$ as a Gaussian of the form

$$M_3(r_1\vec{e}_1, s_1\vec{e}_1) \cong exp\left[-\frac{\gamma_2^2}{2\Sigma_3^2}\ (s_1 - s_{max})^2\right]. \tag{C.31}$$

The product of M2 and M3 is, therefore,

$$M_2(s_1\vec{e}_1)M_3(r_1\vec{e}_1, s_1\vec{e}_1) \cong exp\left[-\frac{s_1^2}{2\Sigma_2^2} - \frac{\gamma_2^2}{2\Sigma_3^2}\ (s_1 - s_{max})^2\right] \tag{C.32}$$

$$= exp\left[-\frac{[\Sigma_3^2+\gamma_2^2\Sigma_2^2]}{2\Sigma_2^2\Sigma_3^2} s_1^2 + \frac{\gamma_2^2 s_{max}}{\Sigma_3^2} s_1 - \frac{\gamma_2^2 s_{max}^2}{2\Sigma_3^2}\right]$$

Returning to Equation (C.20), we find that the s$_1$ integral becomes

$$\int_{-1}^{1} ds_1\ \ (1-s_1^2)^{-1/2}\ M_2(s_1\vec{e}_1)\ M_3(r_1\vec{e}_1, s_1\vec{e}_1) \tag{C.33}$$

$$= exp\left[-\frac{\gamma_2^2 s_{max}^2}{2\Sigma_3^2}\right] \int_{-1}^{1} ds_1\ \ (1-s_1^2)^{-1/2}\ exp\left[-\frac{1}{2\Sigma_{23}^2} s_1^2 + \frac{\gamma_2^2 s_{max}}{\Sigma_3^2} s_1\right]$$

where

$$\Sigma_{23}^2 \equiv \frac{\Sigma_2^2\Sigma_3^2}{[\Sigma_3^2+\gamma_2^2\Sigma_2^2]} < \Sigma_2^2 \ll 1 \tag{C.34}$$

This integral is now performed under the assumption that $\Sigma_{23} \ll 1$. We define

$$
\begin{aligned}
I(A,B) &= \int_{-1}^{1} ds\,(1-s^2)^{-1/2} exp(-As^2+Bs) \\
&= \sum_{m=0}^{\infty} \frac{B^m}{m!} \int_{-1}^{1} ds\,(1-s^2)^{-1/2} s^m exp(-As^2) \\
&= \sum_{m=0}^{\infty} \frac{B^{2m}}{(2m)!}\, 2\int_{0}^{1} ds\,(1-s^2)^{-1/2} s^{2m} exp(-As^2) \\
&= \sum_{m=0}^{\infty} \frac{B^{2m}}{(2m)!} \int_{0}^{1} dx\,(1-x)^{-\frac{1}{2}} x^{m-\frac{1}{2}} exp(-Ax) \qquad \text{(C.35)} \\
&= \sum_{m=0}^{\infty} \frac{B^{2m}}{(2m)!} exp(-A) \int_{0}^{1} dx\,(1-x)^{m-\frac{1}{2}} x^{-\frac{1}{2}} exp(Ax) \\
&= \sum_{m=0}^{\infty} \frac{B^{2m}}{(2m)!} exp(-A) \frac{\Gamma\left(\frac{1}{2}\right)\Gamma\left(m+\frac{1}{2}\right)}{\Gamma(m+1)}\, {}_{1}^{\square}F_1\left(\frac{1}{2}, m+1; A\right).
\end{aligned}
$$

If A>>1 (i.e.,□Σ_{23}<<1), one can apply the asymptotic behavior of ${}_1F_1$ [Equation (C.13)] and find that

$$
\begin{aligned}
I(A,B) &\cong \sum_{m=0}^{\infty} \frac{B^{2m}}{(2m)!} exp(-A)\, \Gamma\left(m+\frac{1}{2}\right)\, exp(A)\, A^{-m-\frac{1}{2}} \\
&= A^{-\frac{1}{2}} \sum_{m=0}^{\infty} \frac{\Gamma\left(m+\frac{1}{2}\right)}{(2m)!} \left(\frac{B^2}{A}\right)^m = \sqrt{\frac{\pi}{A}} \sum_{m=0}^{\infty} \frac{1}{m!} \left(\frac{B^2}{4A}\right)^m \qquad \text{(C.36)} \\
&= \sqrt{\frac{\pi}{A}}\, exp\left(\frac{B^2}{4A}\right)
\end{aligned}
$$

We now can evaluate the s_1 integral of Equation (C.33) using Equation (C.36) with the result that

$$
\begin{aligned}
&\int_{-1}^{1} ds_1\;(1-s_1^2)^{-1/2}\, M_2(s_1\vec{e}_1)\, M_3(r_1\vec{e}_1, s_1\vec{e}_1) \\
&= \frac{\sqrt{2\pi}\Sigma_2\Sigma_3}{\sqrt{\Sigma_3^2+\gamma_2^2\Sigma_2^2}}\, exp\left[-\frac{\gamma_2^2 s_{max}^2}{2[\Sigma_3^2+\gamma_2^2\Sigma_2^2]}\right]. \qquad \text{(C.37)}
\end{aligned}
$$

[N.B.: This expression is dependent on the r_1 parameter because both $\gamma_{\square}$ and s_{max} are functions of r_1.] The function CC as expressed in Equation (C.20) becomes

$$
\begin{aligned}
CC(\nu,\mu;\Sigma_i) \cong \frac{1}{\sqrt{2\pi}\Sigma_1} \int_{-1}^{1} dr_1\,(1-r_1^2)^{-1/2}\, exp\left[-\frac{r_1^2}{2\Sigma_1^2}\right] \qquad \text{(C.38)} \\
\frac{\Sigma_3}{\sqrt{\Sigma_3^2+\gamma_2^2\Sigma_2^2}}\, exp\left[-\frac{\gamma_2^2 s_{max}^2}{2[\Sigma_3^2+\gamma_2^2\Sigma_2^2]}\right].
\end{aligned}
$$

The part of the integrand in the first line of Equation (C.38) is strongly peaked near r_1=0; whereas, the second line of the integrand is peaked around s_{max}=0. According to Equation (C.26) we have

$$
s_{max}(r_1) \cong \Xi(\mu, -\kappa(r_1)). \qquad \text{(C.39)}
$$

If we define r_{max} as the value of r_1 at the peak of the second exponential of the integrand; i.e.,

$$
s_{max}(r_{max}) \equiv 0 \;\Rightarrow\; \Xi(\mu, -\kappa(r_{max})) = 0, \qquad \text{(C.40)}
$$

which, in turn, implies

$$\kappa(r_{max}) \equiv \Xi(\nu, r_{max}) = \mu. \tag{C.41}$$

Once again, one finds a pair of solutions for r$_{max}$ for which the solution of closest approach is given by

$$r_{max} = \sigma\sqrt{1 - \left[max\left(0, \Upsilon(\mu,\nu)\right)\right]^2} \cong \; \Xi(\mu, -\nu) = \; \mu\sqrt{1-\nu^2} - \nu\sqrt{1-\mu^2} \tag{C.42a}$$

and $$\sqrt{1 - r_{max}^2} = max\left(0, \Upsilon(\mu,\nu)\right). \tag{C.42b}$$

As before, we assume that the second exponential in the integrand of Equation (C.38) contributes only in the vicinity of the peak, r$_{max}$=0; so that one can approximate $s_{max}(r_1)$ by a Taylor's series expansion around r$_{max}$. In particular, we approximate

$$s_{max}(r_1) \cong s_{max}(r_{max}) + \left[\frac{ds_{max}}{dr_1}\right]_{r_1=r_{max}} (r_1 - r_{max}) = \gamma_1(r_1 - r_{max}) \tag{C.44}$$

where

$$\gamma_1 \equiv \left[\frac{ds_{max}}{dr_1}\right]_{r_1=r_{max}} = \frac{1}{\sqrt{1-\mu^2}}\left[\sqrt{1-\nu^2} - \frac{\nu r_{max}}{\sqrt{1-r_{max}^2}}\right] \tag{C.45}$$

Because the Gaussians imply r$_1$ and s$_{max}$ must *both* be small, we expect the integrand in Equation (C.38) will be non-vanishing only if $r_{max} \cong 0$. Using the Taylor's series expansion, one finds that

$$\frac{\Sigma_3}{\sqrt{\Sigma_3^2+\gamma_2^2\Sigma_2^2}} exp\left[-\frac{\gamma_2^2 s_{max}^2}{2[\Sigma_3^2+\gamma_2^2\Sigma_2^2]}\right] \tag{C.46}$$

$$\cong \frac{\Sigma_3}{\sqrt{\Sigma_3^2+\gamma_2^2\Sigma_2^2}} exp\left[-\frac{\gamma_2^2\gamma_1^2(r_1-r_{max})^2}{2[\Sigma_3^2+\gamma_2^2\Sigma_2^2]}\right].$$

Putting this expression into Equation (C.38), one finds

$$CC(\nu,\mu;\Sigma_i) \cong \frac{\Sigma_3}{\sqrt{2\pi}\Sigma_1\sqrt{\Sigma_3^2+\gamma_2^2\Sigma_2^2}} \int_{-1}^{1} dr_1\,(1-r_1^2)^{-1/2}\, exp\left[-\frac{r_1^2}{2\Sigma_1^2}\right] \tag{C.47}$$

$$xp\left[-\frac{\gamma_2^2\gamma_1^2(r_1-r_{max})^2}{2[\Sigma_3^2+\gamma_2^2\Sigma_2^2]}\right].$$

Rearranging the terms in the Gaussians and defining

$$\Sigma_{123}^2 = \frac{\Sigma_1^2[\Sigma_3^2+\gamma_2^2\Sigma_2^2]}{[\Sigma_3^2+\gamma_2^2\Sigma_2^2+\gamma_2^2\gamma_1^2\Sigma_1^2]} \le \Sigma_1^2 \ll 1 \tag{C.48}$$

one finds that

$$CC(\nu,\mu;\Sigma_i) \cong \frac{\Sigma_3}{\sqrt{2\pi}\Sigma_1\sqrt{\Sigma_3^2+\gamma_2^2\Sigma_2^2}} exp\left[-\frac{\gamma_2^2\gamma_1^2 r_{max}^2}{2[\Sigma_3^2+\gamma_2^2\Sigma_2^2]}\right] \tag{C.49}$$

$$\int_{-1}^{1} dr_1\,(1-r_1^2)^{-1/2}\, exp\left[-\frac{r_1^2}{2\Sigma_{123}^2}\right] exp\left[\frac{\gamma_2^2\gamma_1^2 r_{max}}{[\Sigma_3^2+\gamma_2^2\Sigma_2^2]} r_1\right].$$

Once again, we invoke the result of Equation (C.36) and get

$$CC(\nu, \mu; \Sigma_i) \cong \frac{\Sigma_3}{\sqrt{\Sigma_3^2+\gamma_2^2\Sigma_2^2+\gamma_1^2\gamma_2^2\Sigma_1^2}} exp\left[-\frac{\gamma_2^2\gamma_1^2 r_{max}^2}{2\left[\Sigma_3^2+\gamma_2^2\Sigma_2^2+\gamma_1^2\gamma_2^2\Sigma_1^2\right]}\right]. \tag{C.50}$$

Equation (C.50) is the result of numerous approximations. Based on this calculation, the following CC function can be summarized by the following analytic calculations:

$$\sigma \equiv sign\left(\mu\sqrt{1-\nu^2} - \nu\sqrt{1-\mu^2}\right) \tag{C.51a}$$

$$\Upsilon \equiv max\left(\epsilon, \mu\nu + \sqrt{1-\mu^2}\sqrt{1-\nu^2}\right) \quad [\epsilon \approx .0001] \tag{C.51b}$$

$$\Delta \equiv \sigma\sqrt{1-\Upsilon^2} \tag{C.51c}$$

$$\chi \equiv \frac{\nu\Delta}{\Upsilon} \tag{C.51d}$$

and

$$CC(\nu, \mu; \Sigma_i) = \frac{\Sigma_3}{\sqrt{\Sigma_3^2+(1-\nu^2)\Sigma_1^2+(1-\mu^2)\Sigma_2^2}} exp\left[-\frac{\left(\sqrt{1-\nu^2}-\chi\right)^2\Delta^2}{2\left[\Sigma_3^2+(1-\nu^2)\Sigma_1^2+(1-\mu^2)\Sigma_2^2\right]}\right]. \tag{C.51e}$$

Equations (C.51a-e) are the final result of this appendix.

Most of the properties of this CC function are consistent with our intuitive expectations. These properties are displayed in Figure C.3 which shows CC as a function of μ and ν for Σ_1=.03, Σ_2=04, and Σ_3=.02. One expects the CC function to be a sharply-peaked ridge along the $\mu = \nu$ line; and this behavior is successfully demonstrated in Figure C.3. Another feature is that the ridge dips from peak values (CC=1) near $\mu = \pm 1$ to a minimum at $\mu = 0$. This behavior arises from the coefficient preceding the exponential and has a natural explanation. This factor accounts for the fraction of the voxel that is viewed within the finite width of the Compton cone. If the voxel is far from the detector ($\Sigma_1 \ll \Sigma_3$), then virtually all voxel will be within the blurred Compton cone; however, if the voxel is near the detector ($\Sigma_3 \ll \Sigma_1$), the cone will slice through the voxel, so that only a fraction of the emissions will be capable of producing the event. Likewise, if the cone axis wobbles significantly ($\Sigma_3 \ll \Sigma_2$), then only a fraction of the wobble positions is capable of producing the event. Consequently, the CC function is suppressed if either the voxel is near the detector or the cone axis is uncertain. The effect is mediated if the cone is tight near the axis because a larger fraction of the cone will intersect the voxel; so that the suppression is reduced as μ approaches ±1. More surprising is the pathologic behavior of the exponential term of the CC function in the vicinity of $\mu = \pm 1$.

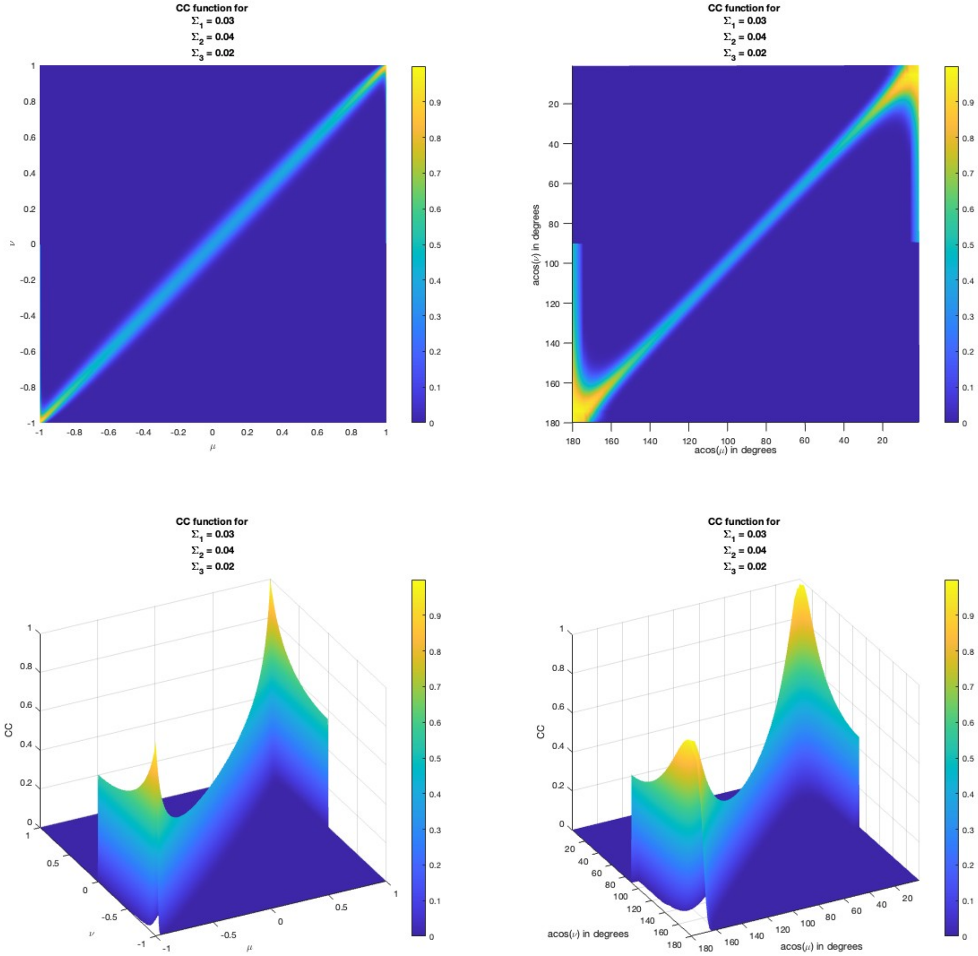

Figure C.3. The $CC(\nu,\mu;\Sigma_i)$ function is displayed as for Σ_1=0.03, Σ_2=0.04, and Σ_3=0.02. The top row shows color lookup tables of the CC function and the second row shows 3D display of the same CC function. The first column shows CC function in terms of the cosines μ and ν from the cone axis; whereas, the second column shows CC in terms of angles (degrees) from the cone axis.

In the vicinity of $\mu = \pm 1$ the CC function as approximated in Equation (C.43) displays anomalous high responses for values of ν on the interval $\nu \in [0,\mu]$. One concludes that the Compton camera provides *no angular resolution* for such events. This result is counter-intuitive because the cases $\mu = \pm 1$ correspond to the Compton cone contracting to a narrow pencil beam – which should provide extremely good angular resolution. This paradox is independent of the angular resolution problems described in Appendix B. The approximations used in the derivation of Equation (C.43) are the source of this paradox. At numerous points in the derivation, we assumed that the Gaussian widths were small and used this assumption to truncate Taylor's series or use asymptotic approximations. In the vicinity of $\mu = \pm 1$ these assumptions may be inappropriate. More significantly the fundamental approximation asserted in Equation (C.18) is based on the "arc-like" appearance of the Compton cone in Figures C.1 and C.2. In the cases of $\mu = \pm 1$, this approximation fails. Different approximations are required for these special cases. [The lead author has spent many months tracking down and accounting for such inappropriate approximations with limited success.] As a practical matter, however, these anomalies do not significantly affect the results. One cannot detect D1 events that deposit no energy in the detector, so the case $\mu = 1$ never arises. The considerations in Appendix B imply that backscattered events ($\mu = -1$) provide so little angular resolution (i.e., Σ_3 is so large) that the such events should not be used in imaging. This conclusion is supported by Figures C.4 and C.5 that display the CC function for realistic detector parameters. Consequently, the Equation (C.43) provides an adequate approximation for all practical purposes.

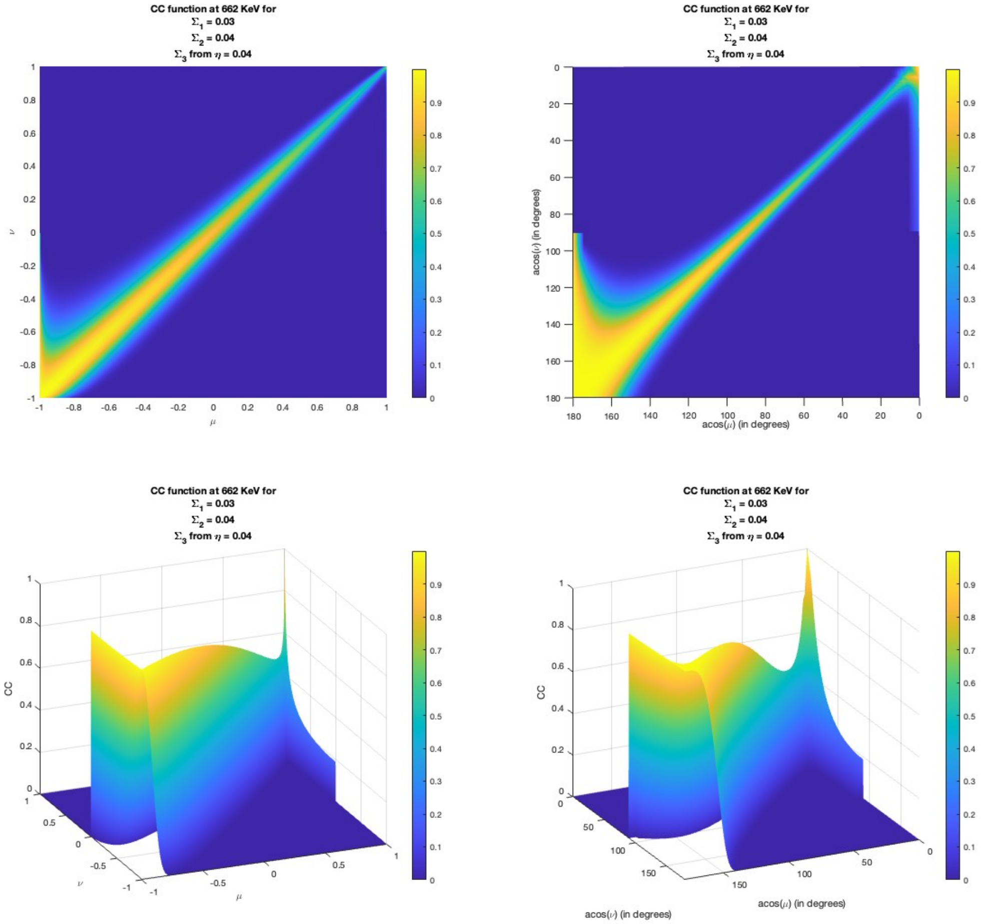

Figure C.4. The $CC(\nu,\mu;\Sigma_i)$ function is displayed as for incident radiation at 662 keV, Σ_1=0.03, and Σ_2=0.04. The parameter Σ_3 is determined by the energy resolution model η=0.04 and ε_0=5keV of Equation (B.13) (i.e., 4% energy resolution at 511 keV). The values of Σ_1 and Σ_2 are the same as Figure C.3. The Σ_3 models a detector with 4% energy resolution at 511 keV. The top row shows color graphics of the CC function and the second row shows 3D projections of the same CC function. The first column shows CC function in terms of the cosines μ and ν from the cone axis; whereas, the second column shows CC in terms of angles (degrees) from the cone axis.

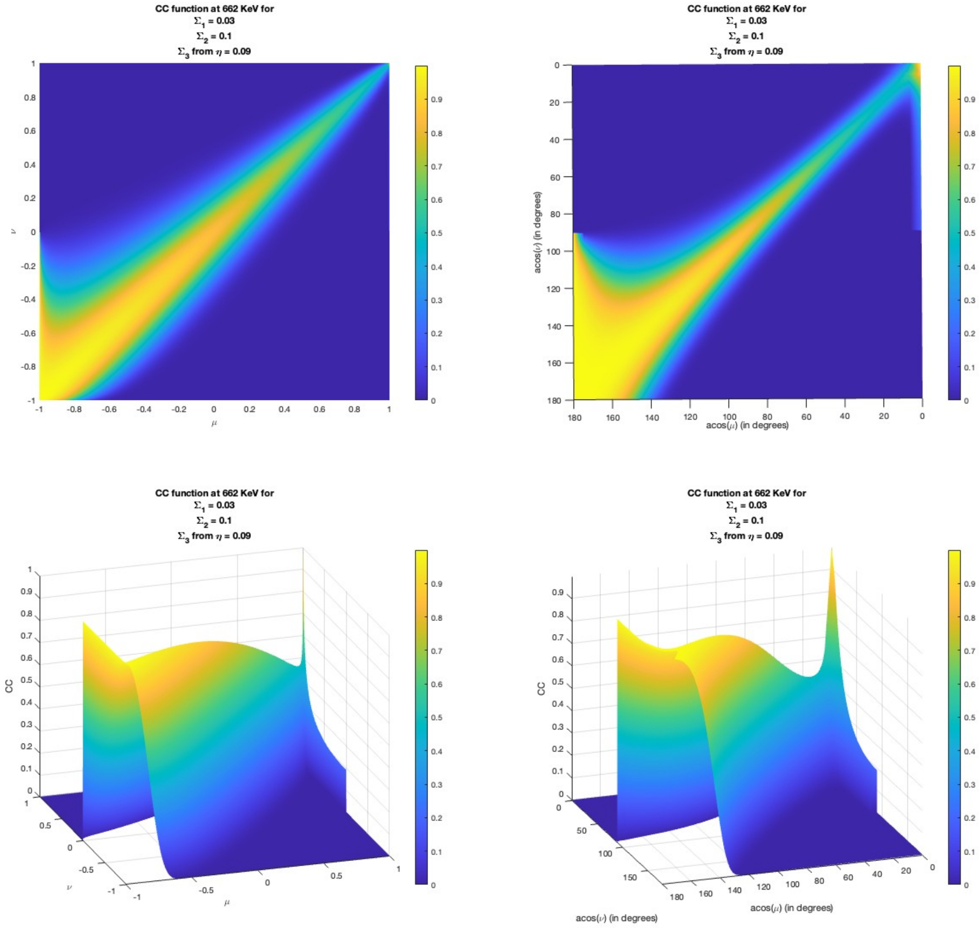

CC function at 662 KeV for
$\Sigma_1 = 0.03$
$\Sigma_2 = 0.1$
Σ_3 from $\eta = 0.09$

CC function at 662 KeV for
$\Sigma_1 = 0.03$
$\Sigma_2 = 0.1$
Σ_3 from $\eta = 0.09$

CC function at 662 KeV for
$\Sigma_1 = 0.03$
$\Sigma_2 = 0.1$
Σ_3 from $\eta = 0.09$

CC function at 662 KeV for
$\Sigma_1 = 0.03$
$\Sigma_2 = 0.1$
Σ_3 from $\eta = 0.09$

Figure C.5. The $CC(\nu, \mu; \Sigma_i)$ function is displayed as for incident radiation at 662 keV, Σ_1=0.03, and Σ_2=0.1. The parameter Σ_3 is determined by the energy resolution model η=0.09 and ε_0=5keV of Equation (B.13). The values of Σ_i are appropriate for the UC Berkeley CCI-II system. The top row shows color lookup tables of the CC function and the second row shows 3D display of the same CC function. The first column shows CC function in terms of the cosines μ and ν from the cone axis; whereas, the second column shows CC in terms of angles (degrees) from the cone axis.

Appendix D. The Relation Between Distant Source Voxels and Incident Fluxes

Throughout this analysis an "idealized" Gaussian voxel is assumed to be the source of radiation as described in Equations (3) and (4). However, a detector inherently observes the local radiation field -- not distant sources. For this reason, one often wants to describe the radiation in terms of the local incident flux originating from directions on the 2-sphere, rather than in terms of distant source voxels. This Appendix provides a method of translating the rate produced by a Gaussian source voxel to/from the rate produced by an incident flux.

In Section III the photon phase-space density, Φ, was defined by

$$\Phi(\vec{x},\vec{p}) \equiv \frac{[\,\#photons\,]}{[m^3][keV^3]} = \text{photon phase} - \text{space density} \quad . \tag{16}$$

The radiation flux is defined by

$$\Psi\left(\vec{x},E,\vec{\Omega}\right) \equiv \frac{\left[\,\#photons\ \left(at\ \vec{x}\ and\ E\ in\ the\ direction\ \vec{\Omega}\right)\,\right]}{[sec][m^2][keV][steradian]} = \text{photon flux} \,. \tag{D.1}$$

The two functions are essentially equivalent and related by

$$\Psi\left(\vec{x},E,\vec{\Omega}\right) = cE^2\Phi\left(\vec{x},E\vec{\Omega}\right) . \tag{D.2}$$

The photon phase-space density is easier to use in calculations and less prone to misinterpretations; whereas, the photon flux emphasizes the directional aspect of the photon distribution and is often more experimentally relevant. The photon flux distribution is generally represented on a 2D sphere showing the intensity of the flux from different directions at energy E. In this Appendix the source of radiation will no longer be a distant voxel; instead, detector position will be assumed fixed at $\vec{x}_0$ and the source will be an incident flux at that location, i.e. $\Psi\left(\vec{x}_0,E,\vec{\Omega}\right)$. This incident radiation flux is a function of the energy, E, and the direction, $\vec{\Omega}$, of the radiation on the 2D sphere. This direction is represented by discrete values on a 2D grid of pixels covering the sphere – each pixel corresponding to a direction of photon propagation. For example, HEALPix provides such a grid (as shown in Figure D.1). Each pixel "i" (i=1,…,N) on the sphere can be characterized by the central direction, $\vec{\Omega}_i$, and pixel size, $\Delta\Omega_i$, in steradians. This pixelization can be characterized analytically by a set of pixelation functions, $\Lambda_i\left(\vec{\Omega}\right)$ where

$$\Lambda_i\left(\vec{\Omega}\right) \equiv \begin{cases} 1 & if\ \vec{\Omega}\ inside\ pixel\ "i" \\ 0 & if\ \vec{\Omega}\ outside\ pixel\ "i" \end{cases} \tag{D.3}$$

[N.B.: the functions Λ_i are dimensionless] and

$$\iint_{S^2} d^2\vec{\Omega}\ \Lambda_i\left(\vec{\Omega}\right) = \Delta\Omega_i \tag{D.4}$$

so that (D.5)

$$\sum_{i=1}^{N} \Delta\Omega_i = 4\pi. \tag{D.6}$$

The incident flux can, therefore, be written as

$$\Psi(\vec{x}_0, E, \vec{\Omega}) = \sum_{i=1}^{N} \Lambda_i(\vec{\Omega})\, \Psi_i(\vec{x}_0, E) \tag{D.7}$$

For most pixelizations, the sizes of the pixels are chosen with equal area; so that, $\Delta\Omega_i \cong 4\pi/N$. Any tessellation of a sphere necessarily requires that the shapes of the pixels be variable (as illustrated in Figure (D.1)]. These variable shapes pose problems for any attempt to characterize the pixels. If one approximates each pixel as rotationally symmetric around the direction $\vec{\Omega}_i$, one can write that

$$\Lambda_i^{approx}(\vec{\Omega}) = \Theta\left(\vec{\Omega} \cdot \vec{\Omega}_i - 1 + \frac{\Delta\Omega_i}{2\pi}\right). \tag{D.8}$$

These "approximate" pixels produce N circular areas that exhibit overlaps and gaps; however, for our purposes, the approximation is both useful and sufficiently accurate.

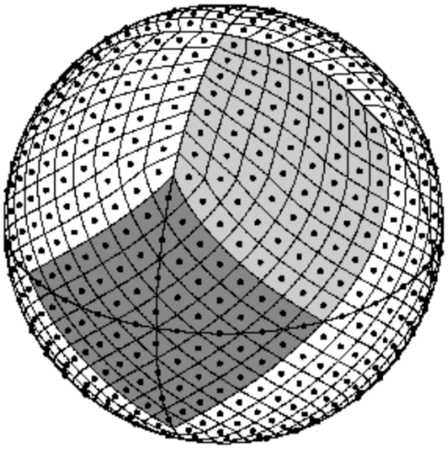

Figure D.1. A typical HEALPix grid is shown. [Taken from: Górski, Krzysztof M.; Hivon, Éric; Banday, Anthony J.; Hansen, Frode K.; Wandelt, Benjamin D.; Reinecke, M.; Bartelmann, M. (2005). "HEALPix: A Framework for High-Resolution Discretization and Fast Analysis of Data Distributed on the Sphere". *Astrophysical Journal*. **622** (2): 759–771. arXiv:astro-ph/0409513]

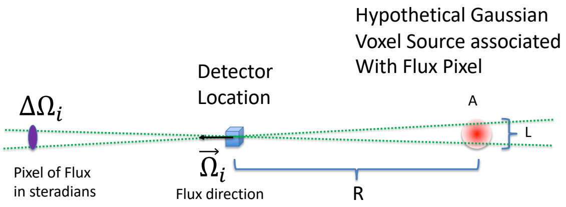

Figure D.2. The basic idea of this appendix is shown in this diagram. The flux of radiation at the detector in the direction $\vec{\Omega}_i$ is represented by a pixel on the celestial sphere of angular size $\Delta\Omega_i$. This flux can be approximated as that of a hypothetical Gaussian voxel source located at an *arbitrarily* large distance, R, from the detector. The Gaussian source strength, A(E), and size, L, at distance R are directly related to the flux, Ψ_i, and size of the pixel on the celestial sphere, $\Delta\Omega_i$.

The basic idea of this appendix is that one can approximate the flux from a single pixel location by a single Gaussian voxel source located far from the detector and in opposite the direction of incident radiation. In this approximation, the grid pattern is reproduced by a collection of Gaussian voxel sources arranged on a sphere surrounding the detector. The distance to the sphere (R) is assumed very large (compared to the detector size) and the voxel size (L) must be selected to match the pixel size (in steradians) of the grid. The geometric idea is presented in Figure D.2.

If a Gaussian source with voxel size L is located at center point $\vec{C} = \vec{x}_0 - R\vec{\Omega}_i$, then the photon phase-space density according to Equation (25) [ignoring attenuation] is given by

$$\Phi^{(0)}(\vec{x}_0, E\vec{\Omega}) = \frac{6\,A(E)L}{4\pi^2 c\,E^2}\exp\left\{-\frac{6R^2}{L^2}\left[1-\left(\vec{\Omega}\cdot\vec{\Omega}_i\right)^2\right]\right\}\Theta\left(\vec{\Omega}\cdot\vec{\Omega}_i\right). \tag{D.9}$$

which, according to Equation (D.2) gives

$$\Psi^{(0)}(\vec{x}_0, E, \vec{\Omega}) = \frac{6\,A(E)L}{4\pi^2}\exp\left\{-\frac{6R^2}{L^2}\left[1-\left(\vec{\Omega}\cdot\vec{\Omega}_i\right)^2\right]\right\}\Theta\left(\vec{\Omega}\cdot\vec{\Omega}_i\right). \tag{D.10}$$

One now compares this incident flux with the desired approximate flux from the pixel “i”; namely,

$$\Psi\left(\vec{x}_0, E, \vec{\Omega}\right) = \Psi_i(\vec{x}_0, E)\ \Theta\left(\vec{\Omega}\cdot\vec{\Omega}_i - 1 + \frac{\Delta\Omega_i}{2\pi}\right). \tag{D.11}$$

These expressions cannot be equated because the angular dependence on $\left(\vec{\Omega}\cdot\vec{\Omega}_i\right)$ differs. However, both expressions are determined by two variables. In Equation (D.10) the function $\Psi^{(0)}$ is determined by the parameters [A(E)L] and [L/R], whereas, in Equation (D.11) the function Ψ is determined by Ψ_i and $\Delta\Omega_i$. {N.B. the parameters [A(E)L] and Ψ_i have the same dimensions [counts/(sec keV cm^2)], whereas both [L/R] and $\Delta\Omega_i$ are dimensionless, as steradians are dimensionless.}. Although the two expressions cannot be equated, the angular distributions can be adjusted by the parameters to give similar results. The key properties of such distributions arise from their integrals with other functions. Because the angular distributions of both Equations (D.10) and (D.11) are radially symmetric around $\vec{\Omega}_i$, a comparison of the "radial" moments is suggested. If one defines the "A" moments by

$$K_A(E) = \iint_{S^2} d^2\vec{\Omega}\, \Psi\left(\vec{x}_0, E, \vec{\Omega}\right)\ \left[1 - \left(\vec{\Omega}\cdot\vec{\Omega}_i\right)^2\right]^A \tag{D.12}$$

and $$K_A^0(E) = \iint_{S^2} d^2\vec{\Omega}\, \Psi^0\left(\vec{x}_0, E, \vec{\Omega}\right)\ \left[1 - \left(\vec{\Omega}\cdot\vec{\Omega}_i\right)^2\right]^A, \tag{D.13}$$

then, by matching the moments of the two distributions, one might hope to find

$$K_A(E) \cong K_A^0(E) \tag{D.14}$$

for all A. Because only two parameters can be matched, one can assert the Equalities (D.14) for only two moments: A=0 and 1. These two moments assure that the total flux and its angular width are approximately equivalent. Using Equation (D.11) for $\Psi\left(\vec{x}_0, E, \vec{\Omega}\right)$ in Equation (D.12), one finds that

$$\begin{aligned} K_A(E) &= 2\pi\Psi_i(\vec{x}_0, E)\int_{1-\frac{\Delta\Omega_i}{2\pi}}^{1} d\mu\,[1-\mu^2]^A \\ &= \frac{\Psi_i(\vec{x}_0,E)(\Delta\Omega_i)}{(A+1)}\left(\frac{\Delta\Omega_i}{\pi}\right)^A {}_2F_1\left(-A, A+1; A+2; \frac{\Delta\Omega_i}{4\pi}\right). \end{aligned} \tag{D.15}$$

Consequently, one finds

$$K_0(E) = \Psi_i(\vec{x}_0, E)(\Delta\Omega_i) \tag{D.16}$$

and $$K_1(E) = \Psi_i(\vec{x}_0, E)(\Delta\Omega_i)\left(\frac{\Delta\Omega_i}{2\pi}\right)\left[1 - \frac{\Delta\Omega_i}{6\pi}\right]. \tag{D.17}$$

Likewise, if one uses Equation (D.10) in Equation (D. 13), one finds

$$\begin{aligned} K_A^0(E) &= \frac{3\,A(E)L}{\pi}\int_0^1 d\mu\,[1-\mu^2]^A \exp\left\{-\frac{6R^2}{L^2}[\,1-\mu^2\,]\right\} \\ &= \frac{3\,A(E)L}{\pi}\exp\left\{-\frac{6R^2}{L^2}\right\}\int_0^1 d\mu\,[1-\mu^2]^A \exp\left\{\frac{6R^2}{L^2}\mu^2\right\} \qquad \text{(D.18)} \\ &= \frac{3\,A(E)L}{2\pi}\exp\left\{-\frac{6R^2}{L^2}\right\}\frac{\Gamma\left(\frac{1}{2}\right)\Gamma(A+1)}{\Gamma\left(A+\frac{3}{2}\right)}\,{}_1F_1\left(\frac{1}{2}, A+\frac{3}{2}; \frac{6R^2}{L^2}\right). \end{aligned}$$

The argument of the confluent hypergeometric function is always large (R>>L), so that one can use the asymptotic behavior of ${}_1F_1$; namely,

$${}_1F_1\left(\frac{1}{2}, A+\frac{3}{2}; z\right) \xrightarrow[1\ll z]{} \frac{\Gamma\left(A+\frac{3}{2}\right)}{\Gamma\left(\frac{1}{2}\right)} exp(z) z^{-A-1} \qquad \text{(D.19)}$$

and find that

$$K_A^0(E) \cong \frac{3\,A(E)L}{2\pi}\Gamma(A+1)\left(\frac{6R^2}{L^2}\right)^{-A-1}. \qquad \text{(D.20)}$$

As a result, one concludes that

$$K_0^0(E) \cong \frac{A(E)L^3}{4\pi R^2} \qquad \text{(D.21)}$$

and $$K_1^0(E) \cong \frac{A(E)L^3}{4\pi R^2}\left(\frac{L^2}{6R^2}\right). \qquad \text{(D.22)}$$

Equating the moments for the two distributions, one finds that

$$\Psi_i(\vec{x}_0, E)(\Delta\Omega_i) = \frac{A(E)L^3}{4\pi R^2} \qquad \text{(D.23)}$$

and $$\Psi_i(\vec{x}_0, E)(\Delta\Omega_i)\left(\frac{\Delta\Omega_i}{2\pi}\right) = \frac{A(E)L^3}{4\pi R^2}\left(\frac{L^2}{6R^2}\right). \qquad \text{(D.24)}$$

From which, one concludes that

$$(\Delta\Omega_i) = \frac{\pi L^2}{3R^2} \qquad \text{(D.25)}$$

and $$\Psi_i(\vec{x}_0, E) = \frac{3A(E)L}{4\pi^2}. \qquad \text{(D.26)}$$

These relations provide the conversion between the local flux $\Psi_i(\vec{x}_0, E)$ from a pixel on the celestial sphere of angular size $\Delta\Omega_i$ and one of the idealized Gaussian voxels treated the paper. The radial distance between the Gaussian voxel and the detector, R, can be chosen arbitrary (provided that R is much greater than the size of the detector system). The size of the Gaussian, L, is then related to the pixel size, $\Delta\Omega_i$, by Equation (D.25). The local flux, $\Psi_i(\vec{x}_0, E)$, is related to the Gauss activity, $A(E)$, by Equation (D.26).

Appendix E. Comparison with an Alternative Treatment by Xu and He

The analysis of Compton camera data has a long history and, consequently, many alternative treatments have been introduced by different researchers. An extensive review and comparison of these alternative approaches is beyond the scope of this report; however, some general observations are useful. Early treatments of the subject involved *ad hoc* observations that the observed rate (or probability of detection) should be proportional to various terms [source activity, (source distance)$^{-2}$, attenuated flux, scattering cross-sections, etc.]; and, subsequently, multiplying these terms together. If all such terms were included, then the result would be proportional to the desired rate (i.e., accurate to within a constant multiplicative factor). The major distinction between our treatment and previous published analyses lies in the analytic calculation of the phase space contributions. These phase space calculations can be analyzed using Monte Carlo simulations. But that strategy is inappropriate when one needs the detector response evaluated rapidly for large numbers of events. Thus, most researchers implement an approximate analytic expression. Among the most concise and insightful treatments is presented by Xu and He [D. Xu & J. He. *Nuclear Instruments and Methods in Physics Research* **A574** (2007) 98-109]. In particular, Section 2 of that paper provides a detailed derivation of their analytic response function – which we consider one of the best in the literature. In this appendix, rather than survey the entire literature, we compare our analysis with that paper. Both the papers analyze two-interaction coincident events. However, Xu and He consider both Compton-Photoelectric events and Compton-Compton events; whereas, this paper considers only Compton-Photoelectric events. Nonetheless, direct comparison of the results is possible. With minor exceptions, the two treatments yield similar results.

Xu and He calculate "the system response function t_{ij}" which "is defined as the probability of a photon emitted from pixel **j** to be observed as a measured event **i**." The definitions of a measured event **i** are the same in both the analysis of Xu and He and this report -- with our Gaussian approximations substituting for their detector voxels and energy bins. The definition of the emission "pixel **j**" requires more careful interpretation. Xu and He assume that the energy and direction of the incident photon are known; whereas, in our analysis the emissions arise from a finite voxel with an energy distribution. Our treatment of emissions from a line spectrum in the limit $L \to 0$, corresponds to that of Xu and He. In our notation, therefore, one finds

$$t_{ij} \equiv \frac{rate\ of\ measure\ events}{rate\ of\ emissions} = \frac{rate_{12}}{A^{*}L^{3}} [\equiv P_{i\alpha}(of\ Appendix\ F)] \qquad \text{(E.1)}$$

where $A^{*}L^{3}$ is the rate of emissions from a source voxel. The limit $L \to 0$ implies that the activity A^{*} (which is a spatial density) must behave as $A^{*} \to L^{-3}$ in order to produce finite rates. Furthermore, from the definition of Σ_1 [Equation (14)], one concludes the treatment of Xu and He corresponds to the limit $\Sigma_1 \to 0$. Xu and He assume that the detectors have perfect efficiency ($Eff_i = 1$), so that our Eff_i terms can be ignored. From the combination of Equation (E.1) with Equation (64), our analysis yields

$$
\begin{aligned}
t_{ij} = \llbracket Att_{int} Att_{ext} \rrbracket \left\{ \tfrac{2\pi^2 \lambda_1^2 \lambda_2^2}{R_S^2 R_{12}^2} \right\} \left[\underline{\mu}_1 \lambda_1 \underline{\mu}_2 \lambda_2 f_{CS1} f_{PE2} X_{KN}^{12} \right] \\
exp\left[-\tfrac{(E_S - E_1 - E_2)^2}{2(\varepsilon_1^2 + \varepsilon_2^2)} \right] \; \Theta\left(2 - \tfrac{mE_1}{(E_1 + E_2)E_2} \right) \; CC(\nu, \mu; \Sigma_i).
\end{aligned}
\tag{E.2}
$$

The equivalent expression given by Xu and He [as Equation (29) in their paper] is

$$
\begin{aligned}
t_{ij} = \frac{2R_0^5 \Delta E_1 \Delta E_2 N^2}{15 R^2 d \sin\theta_{\mathrm{e}}} \, \mathrm{e}^{-\mu_{E_0} \, \mathrm{d}_1} \frac{\mathrm{d}\sigma_{\mathrm{c}}(E_0)}{\mathrm{d}\Omega}\bigg|_{E_1} \frac{2\pi m_{\mathrm{e}} c^2}{(E_0 - E_1)^2} \\
\times \, \mathrm{e}^{-\mu_{E_0 - E_1} d} \frac{\sigma_{\mathrm{p}}(E_2)}{\sqrt{2\pi(\sigma_{E_1}^2 + \sigma_{E_2}^2)}} \mathrm{e}^{-((E_0 - E_1 - E_2)^2 / 2(\sigma_{E_1}^2 + \sigma_{E_2}^2))}.
\end{aligned}
\tag{E.3}
$$

Although their notation is different, many of the terms are immediately recognizable as equivalent to our analysis. In particular, the following expressions appear to be equivalent (our notation on the left, Xu-He notation on the right):

$$
\begin{array}{ll}
Att_{ext} \leftrightarrow e^{-\mu_{E_0} d_1} & Att_{int} \leftrightarrow e^{-\mu_{E_0 - E_1} d} \\
R_s \leftrightarrow R & R_{12} \leftrightarrow d \\
\lambda_1 \leftrightarrow R_0 & \lambda_2 \leftrightarrow R_0 \\
\varepsilon_1 \leftrightarrow \sigma_{E_1} & \varepsilon_2 \leftrightarrow \sigma_{E_2} \\
\varepsilon_1 \leftrightarrow \Delta E_1 & \varepsilon_2 \leftrightarrow \Delta E_2 \\
\underline{\mu}_2 f_{PE2} \leftrightarrow N\sigma_p(E_2) & \underline{\mu}_1 f_{CS1} X_{KN}^{12} \leftrightarrow N \frac{d\sigma_c}{d\Omega}(E_0) \\
\sqrt{1 - \mu^2} \leftrightarrow \sin\theta_e. &
\end{array}
\tag{E.4}
$$

There are, however, some rather glaring differences in our expressions for t_{ij}. The most significant difference is that our analysis considers two scatter angles: (1) the angle between the incident radiation and the axis between interaction positions ($\nu = cos\phi$), and (2) the predicted angle of scatter based on Compton kinematics ($\mu = cos\theta$). In our analysis the blurring of the Compton cone appears in the CC function that compares the cosines (ν and μ) and, thereby, suppresses the response if the angles differ. No such term appears in Xu-He paper. Apparently, their assumption is that the implicit delta function in the Compton cross-section equates the two angles. This assumption eliminates the blurring of the Compton cone that is a crucial component of our analysis. Such an assumption constitutes the most significant difference between the two treatments.

The treatment of the Compton cross-section seems central to many of the discrepancies between the two results. The lengthy (pedantic) discussion of the Compton cross-section was included following Equation (33) for this reason. In our treatment, the kinematics and cross-section are included explicitly; thereby avoiding confusion. For example, one term that appears exclusively in our analysis is the $\Theta\left(2-\frac{mE_1}{(E_1+E_2)E_2}\right)$ function. This function explicitly excludes unphysical scattering angles (i.e., the backscatter limit). In the Xu-He analysis this condition is apparently considered implicit within the Compton cross-section term. The other discrepancies can be explained if one restricts the analysis to the case $\Sigma_1 = 0$ and $\mu = \nu$. In that case, the function CC is given by

$$CC(\mu,\mu;\Sigma_i) = \frac{\Sigma_3}{\sqrt{\Sigma_3^2+(1-\mu^2)\Sigma_2^2}} \tag{E.5}$$

where, according to Equation (54),

$$\Sigma_2 \equiv \frac{\sqrt{\lambda_1^2+\lambda_2^2}}{R_{12}} \tag{E.6}$$

and, according to Equation (B26c),

$$\Sigma_3 = \frac{\varepsilon_1\varepsilon_2 m\left(\varepsilon_1^2+\varepsilon_2^2\right)^{3/2}}{\left[\varepsilon_1^2 E_2+\varepsilon_2^2(E_{el}-E_1)\right]^2} \approx \frac{\varepsilon_1\varepsilon_2 m}{\sqrt{\varepsilon_1^2+\varepsilon_2^2}\,E_2^2} \tag{E.7}$$

so that

$$CC(\mu,\mu;\Sigma_i) = \frac{\varepsilon_1\varepsilon_2 m\, R_{12}}{\sqrt{(\varepsilon_1\varepsilon_2 m\, R_{12})^2+(1-\mu^2)\left(\lambda_1^2+\lambda_2^2\right)\left(\varepsilon_1^2+\varepsilon_2^2\right)E_2^4}}\ . \tag{E.8}$$

Substituting this expression for the CC function in Equation (E.2), one finds

$$\begin{aligned} t_{ij} &= [\![Att_{int}Att_{ext}]\!]\left\{\frac{2\pi^2\lambda_1^2\lambda_2^2}{R_s^2R_{12}^2}\right\}\left[\underline{\mu}_1\lambda_1\underline{\mu}_2\lambda_2 f_{CS1}f_{PE2}X_{KN}^{12}\right] \\ &\quad exp\left[-\frac{(E_{el}-E_1-E_2)^2}{2\left(\varepsilon_1^2+\varepsilon_2^2\right)}\right]\ \Theta\left(2-\frac{mE_1}{(E_1+E_2)E_2}\right)\frac{\varepsilon_1\varepsilon_2 m\, R_{12}}{\sqrt{(\varepsilon_1\varepsilon_2 m\, R_{12})^2+(1-\mu^2)\left(\lambda_1^2+\lambda_2^2\right)\left(\varepsilon_1^2+\varepsilon_2^2\right)E_2^4}}. \end{aligned} \tag{E.9}$$

One notes that dropping the first term under the square root in Equation (E.9), i.e.

$$\sqrt{(\varepsilon_1\varepsilon_2 m\, R_{12})^2+(1-\mu^2)(\lambda_1^2+\lambda_2^2)(\varepsilon_1^2+\varepsilon_2^2)E_2^4} \to \sqrt{(1-\mu^2)(\lambda_1^2+\lambda_2^2)(\varepsilon_1^2+\varepsilon_2^2)E_2^4},$$

reproduces [using the conversions in (E.4)] the result of Xu-He in Equation (E.3). The additional term in the square root of Equation (E.9) prevents a pathology in the Equation (E.3) when $\sin\theta_e = 0$, [i.e., $\mu = \pm 1$] which is a major concern for small angle scattering. In particular, one finds that the ratio of the two expressions for t_{ij} is given by

$$\frac{t_{ij}^{Gunter,et\ al}}{t_{ij}^{Xu-He}} \cong \left\{\frac{15\pi^{3/2}}{2}\right\}\frac{\sqrt{(1-\mu^2)\left(\lambda_1^2+\lambda_2^2\right)\left(\varepsilon_1^2+\varepsilon_2^2\right)E_2^4}}{\sqrt{(\varepsilon_1\varepsilon_2 m\, R_{12})^2+(1-\mu^2)\left(\lambda_1^2+\lambda_2^2\right)\left(\varepsilon_1^2+\varepsilon_2^2\right)E_2^4}}. \tag{E.10}$$

The constant term [in {curly brackets}] is an inevitable result of notational differences; however, the pathological behavior near $\mu = \pm 1$ is significant. Equation (E.10) implies that the two treatments yield equivalent results if

$$\frac{m\varepsilon_1\varepsilon_2}{E_2^2\sqrt{\varepsilon_1^2+\varepsilon_2^2}}\frac{R_{12}}{\sqrt{\lambda_1^2+\lambda_2^2}} \ll \sqrt{1-\mu^2} \equiv \sin\theta_e. \tag{E.11}$$

For typical Compton camera data, one might expect $\left[m\varepsilon_1\varepsilon_2/E_2^2\sqrt{\varepsilon_1^2+\varepsilon_2^2} \approx .03\right]$ and $\left[R_{12}/\sqrt{\lambda_1^2+\lambda_2^2} \approx 10\right]$; so that, the two treatments are essentially equivalent for $\sin\theta_e > 0.3$ or, in angular coordinates, $18° < \theta_e < 162°$.

Our conclusion is that near the Compton cone ($\mu = \nu$), the analysis of Xu and He yields results consistent with this report. The major advantage of the current work is that the rate can be evaluated for voxels not specifically "on the Compton cone." Consequently, the blurring of the Compton cone can be accurately evaluated. Furthermore, the "small-angle" pathology associated with $\sin\theta_e = 0$ in the Xu-He analysis is ameliorated in our analysis.

Appendix F. Utilizing Detection Rates in List-Mode MLEM

The MLEM algorithm is often used in the analysis of Compton camera data. The accumulation of counts is fundamentally a Poisson process and the MLEM algorithm is specifically designed for Poisson-distributed data. The standard MLEM assumes that a collection of 'S' Poisson sources each produce $CE_\alpha (\alpha = 1, \dots, S)$ "counts emitted" over a time period T, and that a collection of 'D' detectors observes $N_i (i = 1, \dots, D)$ "counts detected" over that same period. Furthermore, one assumes that the probability of an emission from source 'α' will be observed in detector 'i' is known; namely,

$$P_{i\alpha} \equiv Probability\ an\ emission\ from\ source\ \alpha\ is\ observed\ in\ detector\ i\ , \quad \text{(F.1)}$$

so that the expectation values of the Poisson distributions are related by

$$\langle N_i \rangle = \sum_{\alpha=1}^{S} P_{i\alpha} \langle CE_\alpha \rangle. \quad \text{(F.2)}$$

The probability matrix, $P_{i\alpha}$, is often call the system matrix. The analysis of detector rates in this report provides an approximate analytic formula for the evaluation of the matrix $P_{i\alpha}$. In particular, for a coincident event [i=(D1,D2)] and a source voxel labeled 'α', our analysis indicates that

$$P_{i\alpha} = \frac{(Rate_{D1D2})_i}{(emission\ rate)_\alpha} = \frac{(Rate_{D1D2})_i}{(A^* L^3)_\alpha}. \quad \text{(F.3)}$$

The MLEM algorithm is an iterative scheme for determining values of CE_α that produce the maximum likelihood associated with a particular Poisson data sample N_i. From an initial estimate of $CE_\alpha^{(k)}$, one calculates successive updates using the algorithm:

$$CE_\alpha^{(k+1)} = \frac{CE_\alpha^{(k)}}{\$_\alpha} \sum_{i=1}^{D} \frac{N_i}{\sum_{\beta=1}^{S} P_{i\beta} CE_\beta^{(k)}} P_{i\alpha} \quad \text{(F.4)}$$

where $$\$_\alpha \equiv \sum_{i=1}^{D} P_{i\alpha}. \quad \text{(F.5)}$$

The parameter $\$_\alpha$ is defined as the sensitivity of the source α. Equations (F.1) through (F.5) constitute the standard MLEM. One should note that *all* the parameters in the algorithm are dimensionless numbers, i.e. counts or probabilities. But for most imaging applications, the *source rates* are required – not the number of counts emitted, CE_α.

At the beginning of our analysis, we concluded that the source activity density, A, with units of $[(emissions)/(\sec \cdot m^3 \cdot keV)]$, was the most appropriate parameter to represent voxel sources. In Appendix B, the analysis was restricted to sources with Gaussian energy spectra that could be adapted to various applications. Accordingly, in Appendix B the activity was written as

$$A(k) = \frac{A^*}{\sqrt{2\pi}\Sigma_s}\, exp\left[-\frac{(k-E_s)^2}{2\Sigma_s^2}\right] \quad \text{(B.2)}$$

where A^* has dimensions $[(counts)(sec^{-1})(m^{-3})]$ and both E_b and Σ_b have units of energy $[(keV)]$. One can view the Gaussian parameter Σ_b as the width of the source energy bin. The distinction between A and A* is significant because the dimensions of the two parameters differ, i.e.

$$A \sim \frac{[emissions]}{[sec][m^3][keV]} \qquad A^* \sim \frac{[emissions]}{[sec][m^3]};$$

so that, the number of "counts emitted" from the "α" voxel, CE_α, can be written as

$$CE_\alpha = TL_\alpha^3 A_\alpha^*. \tag{F.6}$$

N.B.: The specific value of A* does *not* affect the definition of the probability, $P_{i\alpha}$, in Equation (F.3) because the A* in the denominator cancels an identical A* term appearing in the Rate (D1,D2) of the numerator. The substitution of Equation (F.6) into Equation (F.2) yields

$$\langle N_i \rangle = \sum_{\alpha=1}^{S} P_{i\alpha} T L_\alpha^3 A_\alpha^* \tag{F.7}$$

Finally, Equation (F.7) can be further generalized by assuming that each independent measurement, N_i, could be acquired over a time of variable duration or acquisition time T_i. With this additional generalization, one can write

$$\langle N_i \rangle = \sum_{\alpha=1}^{S} T_i P_{i\alpha} L_\alpha^3 A_\alpha^* = \sum_{\alpha=1}^{S} K_{i\alpha} A_\alpha^* \tag{F.8}$$

where the "kernel matrix" (not to be confused with the "system matrix") is defined by

$$K_{i\alpha} \equiv T_i P_{i\alpha} L_\alpha^3 = diag(T_i) P_{i\alpha} diag(L_\alpha^3) \tag{F.9}$$

and has dimensions $[(sec)(m^3)]$ due to the T and L^3 terms. A corresponding MLEM algorithm follows from the same derivation as the original MLEM algorithm applied to Equation (F.8); namely,

$$A_\alpha^{*(k+1)} = \frac{A_\alpha^{*(k)}}{\$_\alpha^K} \sum_{i=1}^{D} \frac{N_i}{\sum_{\beta=1}^{S} K_{i\beta} A_\beta^{*(k)}} K_{i\alpha} \tag{F.10}$$

where the *kernel* sensitivity, $\$_\alpha^K$, must now be defined by

$$\$_\alpha^K \equiv \sum_{i=1}^{D} K_{i\alpha} \tag{F.11}$$

which has the same dimensions as $K_{i\alpha}$, i.e., $[(sec)(m^3)]$. This generalized form of the MLEM is used for the analysis of List-Mode MLEM.

List-Mode MLEM was first introduced for the analysis of coincident events in PET reconstruction. In PET imaging, a major problem arises from the number of possible combinations of coincident interactions. For an imaging device consisting of 10^4 segmented detector voxels, one expects 10^8 combinations of coincident interactions. If only 10^6 events are detected, then less than 1% of the possible combinations are observed, i.e., $N_i \neq 0$; the vast majority of detector combinations must vanish, i.e., $N_i = 0$. In this situation, the binning of the event data into 10^8 possible coincident combinations is inefficient and, frequently, infeasible. Instead, a list of the events is stored; each event is then interpreted as a “bin” with $N_i = 1$. Most significantly, the summation in Equation (F.10) does not require the evaluation of $K_{i\alpha}$ for unobserved event combinations (i.e., if $N_i = 0$, none of the other terms in the sum need be evaluated); thereby, saving both computation time and computer memory. This observation is the basis of list-mode MLEM. The same situation arises with Compton camera events; namely, many combinations of coincident interaction are unobserved and can be ignored. However, Compton cameras generally involve an additional complication – the camera is generally moving during the data acquisition. Surprisingly, this motion has little effect on the imaging kernel, $K_{i\alpha}$, which is evaluated *for each event* using the formalism of this report; but, unfortunately, the calculation of the sensitivity is significantly altered. The problem arises from the definition of the sensitivity in Equation (F.11). This summation must include *all possible* events, independent of whether those events were actually observed or not. This implies the calculation of the kernel matrix for all possible camera positions *and* all combinations of interaction positions, energies and their resolutions! For the fixed geometry of a PET imaging device, this sensitivity can be evaluated once (either experimentally or theoretically) and used in all subsequent analyses. But for a moving camera, the sensitivity will depend on the trajectory and orientation of the camera; and will, therefore, change with each data acquisition. If the camera passes close to source voxel or sits near the voxel over a long period, the sensitivity of that voxel will rise. If a voxel is far from the camera trajectory or is passed only fleetingly, the sensitivity will be small. Consequently, the calculation of the sensitivity for a moving camera is complicated by *both* (1) the details of the camera trajectory/orientation and (2) the inclusion of unobserved combinations of interactions in the summations.

The crucial idea required for list-mode analysis requires the subdivision of the observations into extremely short time intervals. In particular the time intervals $[T_i = dt]$ must be so short that (1) no two events are observed during the same interval, and (2) during each interval the motion of the camera is negligible. The camera motion will be described by the position, $\vec{D}(t)$, associated with the location of a central fiducial point in the camera as a function of time.

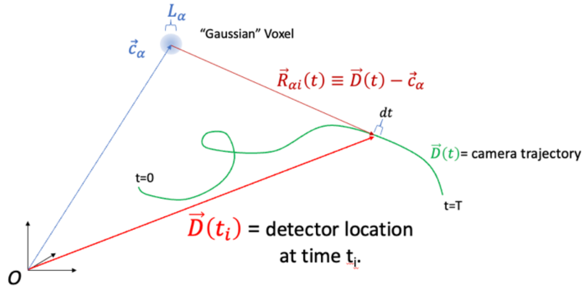

Figure F.1. A camera trajectory is shown with a source voxel.

From Figure F.1, one defines the distance between the source voxel and the detector as

$$R_\alpha(t) \equiv \left|\vec{R}_{\alpha i}(t)\right| = \left|\vec{D}(t) - \vec{C}_\alpha\right| \approx R_s > L_\alpha. \qquad \text{(F.12)}$$

One must also consider the orientation of the detector with respect to the source voxel α. For notational convenience, the orientation will be described by a rotation matrix, $\hat{O}_\alpha(t)$, that indicates the relative orientation of the source to the fixed axes of the detector. The evaluation of the sum $\Sigma_{i=1}^{D}$ in Equation (F.11) involves the sum over all possible combinations of interactions and also all the infinitesimal time intervals, dt_i. Formally, one can write the sum as

$$\Sigma_{i=1}^{D} = \Sigma_{time\ intervals}^{\square}\Sigma_{interaction\ combinations}^{\square} \cdot \qquad \text{(F.13)}$$

The sum over time intervals is naturally written as

$$\textstyle\sum_{time\ intervals} dt_i \to \int_0^T dt, \qquad \text{(F.14)}$$

whereas, the sum over interaction combinations can be formally written as

$$\Sigma^{\square}_{\substack{interaction\\ combinations}} \to \iiint^{\square}_{\substack{Device\\ Volume}} d^3\vec{x}_1 \iiint^{\square}_{\substack{Device\\ Volume}} d^3\vec{x}_2 \int dE_1 \int dE_2\, \frac{1}{(2\pi)^4\lambda_1^3\lambda_2^3\varepsilon_1\varepsilon_2}\,. \qquad \text{(F.15)}$$

If one wants to evaluate the dimensionless sensitivity, $\$_\alpha$, [as defined by Equation (F.5)] for a fixed detector location and orientation, one writes

$$\$_\alpha\left(R_\alpha, \hat{O}_\alpha\right) \equiv \textstyle\sum_{i=1}^{D} P_{i\alpha}\left(R_\alpha, \hat{O}_\alpha\right) \qquad \text{(F.16)}$$

$$= \iiint^{\square}_{\substack{Device\\ Volume}} d^3\vec{x}_1 \iiint^{\square}_{\substack{Device\\ Volume}} d^3\vec{x}_2 \int dE_1 \int dE_2\, \frac{P_{i\alpha}(R_\alpha,\hat{O}_\alpha)}{(2\pi)^4\lambda_1^3\lambda_2^3\varepsilon_1\varepsilon_2}.$$

If the separation of the detector and the source voxel is sufficiently large, one may assume that

$$\$_\alpha\left(R_\alpha, \hat{O}_\alpha\right) = \frac{R_0^2}{R_\alpha^2}\$_\alpha\left(R_0, \hat{O}_\alpha\right) \qquad \text{(F.17)}$$

and define

$$\$_\alpha(R_0, max) \equiv max_{all\ orientations}\left[\$_\alpha\left(R_0, \hat{O}_\alpha\right)\right]. \qquad \text{(F.18)}$$

One can, therefore, write the kernel sensitivity, $\$_\alpha^K$, as

$$\$_\alpha^K = \$_\alpha(R_0, max) L_\alpha^3 \int_0^T dt\, \frac{R_0^2}{R_\alpha^2(t)} \frac{\$_\alpha\left(R_0, \hat{O}_\alpha(t)\right)}{\$_\alpha(R_0, max)}\,. \qquad \text{(F.19)}$$

Typically, the dimensionless sensitivity, $\$_\alpha\left(R_0, \hat{O}_\alpha\right)$, is measured experimentally and the kernel sensitivity, $\$_\alpha^K$, is evaluated for each detector trajectory by performing the integral over time. Each source voxel is "effectively" observed for a period of

$$T_\alpha^{eff} \equiv \int_0^T dt \frac{R_0^2}{R_\alpha^2(t)} \frac{\$_\alpha\left(R_0, \hat{O}_\alpha(t)\right)}{\$_\alpha(R_0, max)} \tag{F.20}$$

so that

$$\$_\alpha^K = \$_\alpha(R_0, max) L_\alpha^3 T_\alpha^{eff}. \tag{F.21}$$

Returning to the List-Mode MLEM algorithm [Equation (F.10)], one writes

$$A_\alpha^{*(k+1)} = \frac{A_\alpha^{*(k)}}{\$_\alpha^K} \sum_{i=1}^{D} \frac{K_{i\alpha}}{\sum_{\beta=1}^{S} K_{i\beta} A_\beta^{*(k)}}. \tag{F.22}$$

Significant observations follow directly from Equation (F.22). First, the dimensions on either side of Equation (F.22) agree. The sum $\left[\sum_{\beta=1}^{S} K_{i\beta} A_\beta^{*(k)} (\ll 1)\right]$ is the (dimensionless) number of expected counts for detector configuration "i". Because $\$_\alpha^K$ and $K_{i\alpha}$ have the same dimensions [(sec)(m^3)], the term $[K_{i\alpha}/\$_\alpha^K]$ is also dimensionless. Consequently, $A_\alpha^{*(k+1)}$ has the same dimensions as $A_\alpha^{*(k)}$. Second, the infinitesimal time intervals, dt_i, *do not affect the calculation*. Although the integration of these time intervals appears implicitly in the evaluation of T_α^{eff}, the explicit value of dt_i appears identically in $K_{i\alpha}$ of both the numerator and denominator of Equation (F.22) and, therefore, will cancel out. Third, the effect of voxel size is crucial and cannot be ignored. Unlike the time intervals that are identical in the numerator and denominator, the voxel sizes for various sources "β" in the sum $\sum_{\beta=1}^{S} K_{i\beta} A_\beta^{*(k)}$ are not necessarily equal and will give erroneous results if ignored.

Finally, the List-Mode MLEM suffers from the same problem as MLEM if the kernel sensitivity vanishes. If the kernel sensitivity, $\$_\alpha^K$, is extremely small, the algorithm will amplify noise and, consequently, predict anomalously high activities in the 'α' voxel. The standard regularization strategy used in MLEM can be applied to List-Mode MLEM if one substitutes

$$\frac{1}{\$_\alpha^K} \to \frac{\$_\alpha^K}{\left(\$_\alpha^K\right)^2 + \tau^2 \left(\$_{\alpha,max}^K\right)^2} \tag{F.23}$$

in Equation (F.22), where

$$\$_{\alpha,max}^K \equiv max_\alpha(\$_\alpha^K) \tag{F.24}$$

and the parameter τ is a dimensionless Tikhonov regularization parameter that satisfies $0 \leq \tau \ll 1$.

Appendix G. Gaussian Voxels in N-Dimensions

A voxel in N-dimensions can be written as a function of the form

$$\Lambda(\vec{x}|\vec{c},L) = \begin{cases} 1 & if\ |x_i - c_i| < \frac{L}{2}\ for\ all\ i = 1, \dots, N \\ 0 & otherwise \end{cases} \tag{G.1}$$

which is an N-dimensional box. One wants to approximate this distribution with an N-dimensional isotropic Gaussian of the form

$$\Xi(\vec{x}|\vec{c},A,\Sigma) = A\ exp\left[-\frac{|\vec{x}-\vec{c}|^2}{2\Sigma^2}\right]. \tag{G.2}$$

Obviously, the two distributions are not identical; however, one wants *integrals over these two distributions* that give approximately the same results. Therefore, the moments of the distributions must be examined and equated if possible. Because the Gaussian has only two free parameters ($A\ and\ \Sigma$), only two moments can be matched; presumably, the lowest order moments are the most important. Thus, one defines

$$I_0 \equiv \iiint d^N x\ \ \Lambda(\vec{x}|\vec{c},L) \tag{G.3a}$$
$$I_2 \equiv \iiint d^N x\ \ |\vec{x}-\vec{c}|^2\, \Lambda(\vec{x}|\vec{c},L) \tag{G.3b}$$

and

$$J_0 \equiv \iiint d^N x\ \ \Xi(\vec{x}|\vec{c},A,\Sigma) \tag{G.4a}$$
$$J_2 \equiv \iiint d^N x\ \ |\vec{x}-\vec{c}|^2\, \Xi(\vec{x}|\vec{c},A,\Sigma) \tag{G.4b}$$

The I_0 and I_2 integrals are easily evaluated; in particular,

$$I_0 = L^N \tag{G.5a}$$

and $$I_2 = \frac{N}{12} L^{N+2}. \tag{G.5b}$$

On the other hand, the J_0 and J_2 integrals require slightly more analysis.

$$J_0 \equiv A \iiint d^N x\ \ exp\left[-\frac{|\vec{x}|^2}{2\Sigma^2}\right] = A\left[\int_{-\infty}^{\infty} dx\ exp\left[-\frac{|\vec{x}|^2}{2\Sigma^2}\right]\right]^N \tag{G.6a}$$

$$\begin{aligned} J_2 &\equiv A \iiint d^N x\ \ |\vec{x}|^2\ exp\left[-\frac{|\vec{x}|^2}{2\Sigma^2}\right] \\ &= NA\left[\int_{-\infty}^{\infty} dx\ x^2 exp\left[-\frac{|\vec{x}|^2}{2\Sigma^2}\right]\right]\left[\int_{-\infty}^{\infty} dx\ exp\left[-\frac{|\vec{x}|^2}{2\Sigma^2}\right]\right]^{N-1} \end{aligned} \tag{G.6b}$$

The two integrals are evaluated in terms of the Γ function; namely,

$$\begin{aligned} \int_{-\infty}^{\infty} dx\ exp\left[-\frac{|\vec{x}|^2}{2\Sigma^2}\right] &= 2\int_0^{\infty} dx\ exp\left[-\frac{|\vec{x}|^2}{2\Sigma^2}\right] = \sqrt{2}\Sigma \int_0^{\infty} du\ \ u^{-1/2} exp(-u) \\ &= \sqrt{2}\Sigma\Gamma\left(\frac{1}{2}\right) = \sqrt{2\pi}\Sigma \end{aligned} \tag{G.7a}$$

and

$$\int_{-\infty}^{\infty} dx\, x^2 exp\left[-\frac{|\vec{x}|^2}{2\Sigma^2}\right] = 2\int_0^{\infty} dx\, x^2 exp\left[-\frac{|\vec{x}|^2}{2\Sigma^2}\right] = 2\sqrt{2}\Sigma^3 \int_0^{\infty} du\ u^{1/2} exp(-u)$$
$$= 2\sqrt{2}\Sigma^3\Gamma\left(\frac{3}{2}\right) = \sqrt{2\pi}\Sigma^3. \qquad \text{(G.7b)}$$

As a result, one finds

$$J_0 = (2\pi)^{N/2} A\Sigma^N \qquad \text{(G.8a)}$$
$$J_2 = (2\pi)^{N/2} NA\Sigma^{N+2}. \qquad \text{(G.8b)}$$

Equating the moments, one finds

$$I_0 = J_0 \Rightarrow L^N = (2\pi)^{N/2} A\Sigma^N \qquad \text{(G.9a)}$$

and $$I_2 = J_2 \Rightarrow \frac{N}{12} L^{N+2} = (2\pi)^{N/2} NA\Sigma^{N+2}. \qquad \text{(G.9b)}$$

From Equations (G.9a) and (G.9b) one immediately concludes that

$$\Sigma = \sqrt{\frac{1}{12}} L \qquad \text{(G.10a)}$$

and $$A = \left(\frac{6}{\pi}\right)^{N/2}. \qquad \text{(G.10b)}$$

From these results the Gaussian voxel in N dimensions is written as

$$\Xi(\vec{x}|\vec{c}, L) = \left(\frac{6}{\pi}\right)^{N/2}\ exp\left[-\frac{6|\vec{x}-\vec{c}|^2}{\mathrm{L}^2}\right]. \qquad \text{(G.11)}$$

Figure G.1 compares a 1-dimensional (N=1) energy bin $\Lambda(\vec{x}|\vec{c}, L)$ with the associated Gaussian bin $\Xi(\vec{x}|\vec{c}, L)$. The area under both curves is the same; furthermore, the second order moments (standard deviations) are also equal.

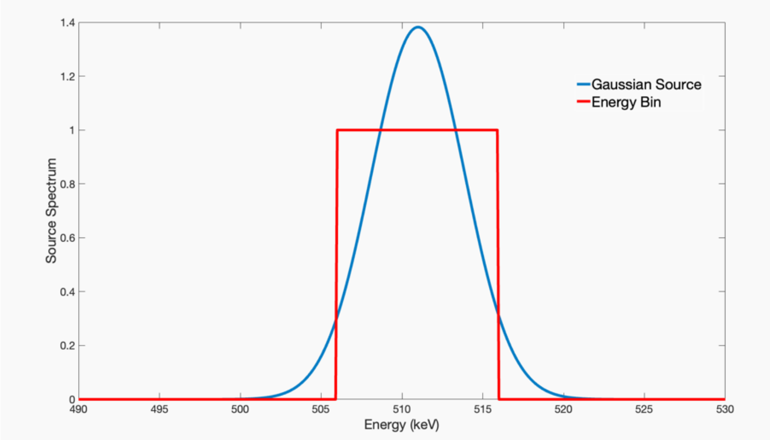

Figure G.1. The 1D Gaussian approximation $\Xi(\vec{x}|E, L)$ of a standard energy bin $\Lambda(\vec{x}|E, L)$ is shown for E=511 keV and L=10 keV.